



Justus-Liebig-Universität Gießen

Neue Konzepte für Sampling-Kalorimeter

Novel concepts for sampling calorimetry

Master's thesis
by
Sebastian Zimmermann

April 2016

1. Gutachter: Prof. Dr. K.-Th. Brinkmann
2. Gutachter: Dr. S. Lange

Contents

1	Calorimetry	5
1.1	Particle Interaction with Matter	6
1.1.1	Ionization and Excitation of Charged Particles	6
1.1.2	Bremsstrahlung	9
1.1.3	Cherenkov Radiation	9
1.1.4	Photon Interactions	10
1.1.5	Nuclear Interactions	12
1.2	Shower Development	13
1.2.1	Electromagnetic Shower	14
1.2.2	Hadronic Shower	17
1.3	Desirable Properties for Calorimeter	19
1.4	Calorimeter Setups	20
1.4.1	Homogeneous Calorimeter	21
1.4.2	Sampling Calorimeter	22
1.4.3	Challenges of Hadron Callorimetry	23
1.4.4	Active Detector Material	24
1.4.5	Readout	26
1.5	Radiation Damage in Scintillators	28
1.5.1	Radiation Dependency of the Damage	29
1.5.2	Damage Recovery	30
2	LuAG and YAG fibers	33
2.1	Motivation	33
2.2	Attenuation Measurement Setup	36
2.2.1	Measurement of Irradiated LuAG Fibers	37
2.2.2	Measurement of rectangular YAG and LuAG fibers	38
2.3	First Beam Time at MAMI in Mainz	39
2.3.1	MAMI Irradiation Facility	40
2.3.2	Experimental Setup	42
2.3.3	Data Analysis	43
2.3.4	Experimental Results	44
2.4	Second Beam Time at MAMI	45
2.4.1	Extended Data Analysis	46
2.4.2	Experimental Results	50
3	Study of the optical properties of DSB	55
3.1	Motivation	55
3.2	DSB:Ce Fibers	55
3.2.1	Attenuation Measurements	56

3.2.2	Fiber Scintillation Measurement	58
3.2.3	Fiber Matrix	59
3.3	DSB Block	60
3.3.1	Transmission Measurements	61
3.3.2	Light Yield Measurements	61
3.3.3	Measurement of the Radiation Damage	65
3.4	DSB Block II	66
3.4.1	Transmission Measurements	67
3.4.2	Light Yield Measurements	67
4	Discussion	71
4.1	LuAG fibers	71
4.1.1	Attenuation of irradiated pulled LuAG fibers	71
4.1.2	Attenuation of cut LuAG and YAG fibers	71
4.1.3	LuAG fiber calorimeter	72
4.2	DSB	74
4.2.1	Emission	74
4.2.2	Fiber Measurements	74
4.2.3	DSB Matrix	75
4.2.4	DSB Block Transmission Measurement	76
4.2.5	Light Yield Measurements	76
4.2.6	Radiation Damage	77

Zusammenfassung

Um den Bedingungen der immerfort steigenden Energien, die von Teilchenbeschleunigern erreicht werden, standzuhalten, müssen neue Kalorimeterkonzepte, so wie strahlungsharte Materialien verwendet werden. Die szintillierenden Kristalle des CMS Experiments weisen Strahlungsschäden auf und müssen im kommenden LHC Upgrade ersetzt werden. In dieser Arbeit werden LuAG:Ce Fiber, sowie ein Samplingkalorimeter aus LuAG Fiber, eingebettet in einer Wolframmatrix, untersucht. Ein Satz gezogener Fiber war einem Protonenstrahl mit einer Energie von 180 MeV und einer Fluenz von $7.5 \cdot 10^{12}$ protons/cm² ausgesetzt und zeigte nur geringe Schäden. Ein zweiter Satz, in dem Kalorimeter eingesetzter, rechteckig geschnittener Fiber zeigte ein unregelmäßiges Abschwächungsverhalten mit Abschwächungskoeffizienten zwischen $0.25(3)$ cm⁻¹ und $0.069(3)$ cm⁻¹. Das Energieverhalten des Kalorimeters wurde mithilfe eines 56 MeV bis 767 MeV Photonenstrahls untersucht und zeigte für hohe Energien eine Energieauflösung von rund 30%. Merkmalsextraktion über die Amplitude so wie das Integral zeigen ähnliche Ergebnisse, außer für niedrige Energien, bei denen die Auflösung der Integralmethode unter dem Beitrag des Untergrunds leidet. Um die Energieauflösung zu verbessern wurde eine Pile-Up Erkennung implementiert, die jedoch nur die Auflösung der Integral methode bei kleinen Energien verbessert.

Zusätzlich wurde DSB (BaO₂*2SiO₂) eine neue, strahlungsharte, szintillierende Glasskeramik untersucht. Das niedrige effektive Z von 51 verhindert kernspaltungsspezifische Schäden. Ein kleines Samplingmodul aus 20 ein mm dünnen und 5 cm langen Fibern in einer Molybdenmatrix zeigt ein Signal von ungefähr ein- bis zweihundert Photoelektronen für kosmische Myonenstrahlung. Die Lichtausbeute eines $23 \times 23 \times 120$ mm³ Blocks mit 55,2 Photoelektronen pro MeV bei einer Integrationszeit von 10 μs und einer Temperatur von 18 °C, zeigt eine lange Emissionskomponente in der Größenordnung einiger μs. Makrodefekte in den Proben, in den Fibern, sowie auch in dem Block reduzieren die Transmission. Die Lichtausbeute des Blocks zeigt eine Abnahme von 25.1% über 12 cm.

Da eine relative Energieauflösung von 30% bei einer Energie von 767 MeV nicht den Standards moderner Detektoren entspricht und sichtbare Makrodefekte und Unvollkommenheiten in den DSB Proben die Leistung limitieren, sind weitere Entwicklungen in beiden Fällen nötig. Um eine bessere Leistung des Samplingkalorimeters zu erzielen, müssen die Auswirkungen spezifischer Aspekte, wie die *sampling fraction* und die *sampling Frequenz*, sowie die Ausrichtung der Fiber der Strahlungsrichtung gegenüber, untersucht werden. Weitere Entwicklungen der DSB Produktion für pure, als auch mit Gadolinium angereicherte Proben müssen gemacht werden, bevor eine sinnvolle Anwendung betrachtet werden kann.

Abstract

In order to withstand the growing energies reached by particle accelerators new calorimeter concepts and radiation hard materials need to be employed. Scintillator crystals in the CMS experiment suffer from radiation induced damages and need to be replaced in the upcoming LHC upgrade. In this thesis LuAG:Ce fibers as well as a sampling calorimeter with LuAG:Ce fibers in a tungsten matrix are studied. A set of pulled fibers were exposed to a 180 MeV proton beam with a fluence of $7.5 \cdot 10^{12}$ protons/cm² and showed little to no damage. A second set of rectangular cut fibers used in the calorimeter show irregular attenuation behavior with attenuation coefficients between $0.25(3)$ cm⁻¹ and $0.069(3)$ cm⁻¹. The response of the calorimeter was studied with 56 MeV to 767 MeV photons and showed a relative energy resolution of around 30 % for high energies. Feature extraction via amplitude and integral methods show similar results except for low energies where the integral method suffers from background noise. To improve the resolution a pileup rejection was implemented which improves the resolution for the integral only.

In addition to that DSB (BaO_2SiO_2) a new radiation hard scintillating glass ceramic is studied. Its low effective Z value of 51 prevents fission-specific damage. A small sampling module made out of 20 one mm thin and five cm long fibers in a molybdenum matrix shows one to two hundred photoelectrons for cosmic muons radiation. The light yield of a $23 \times 23 \times 120$ mm³ block shows a light yield of 55.2 photoelectrons per MeV for an integration time of 10 μ s at a temperature of 18 °C and a long component in the order of micro seconds for the decay time. Macro defects in the samples, in the fibers as well as in the block, reduce the transparency. The light yield of the block shows a loss of 25.1 % over 12 cm.

Since a relative energy resolution of 30 % at 767 MeV does not reach the standards of modern detectors, and visible macro defects and imperfections limit the performance of DSB, further development is necessary in both cases. To achieve a better performance of the calorimeter, the impact of specific aspects such as the sampling fraction and frequency as well as the orientation need to be studied. Further development of the DSB production of gadolinium loaded and pure DSB is necessary too, before meaningful applications can be considered.

Chapter 1

Calorimetry

Calorimeters are detectors built to measure energy. The name implies a measurement of heat energy. One calorie is the amount of heat energy needed to raise the temperature of one gram of water by one degree Celsius at a pressure of one atmosphere which is equivalent to 4.184 J. Measuring the absorption of heat energy is the main application of calorimeters. They measure temperature changes in various ways and employ phenomena such as the phase shift of water from ice to liquid water, where the amount of melted water from an ice block with a surrounding temperature of 0°C is proportional to the amount of heat energy added. In this way also kinetic energy can be measured by stopping the object and transforming its energy into heat.

In particle physics calorimeters are used to determine particle energies. In order to measure the full particle energy, it is important that the particle is stopped in the detector. Unlike measurements with wire chambers for example, which measure the momentum of a particle by tracking them in a magnetic field of known strength, calorimetry is a *destructive* way of measurement, meaning no further measurement of the particle is possible after hitting the calorimeter.

Use for these devices can be found in different areas of science. Different fields of application are in medicine, in diagnostic medical equipment such as PET scanners or gamma cameras, in astronomy on satellites examining cosmic radiation and in nuclear and high energy physics. Each field has a specific area of interest in the energy spectrum ranging from a couple of eV to 10^{20} eV. Modern physics experiments are reaching particle energies of up to some TeV, still far below the about 10^7 TeV of energy one calorie corresponds to. The resulting rise in temperature caused by such a particle with 1 TeV of energy is hardly measurable, if at all. Hence a different approach to the energy measurement must be employed, using the interactions of these particles with matter and secondary processes.

All charged particles are subjected to the Coulomb force. In matter they interact with the atomic electrons transferring energy, exciting and ionizing the atoms producing secondary particles. These emitted photons and electrons are converted into an electric current, proportional to their amount, which is easily measurable. Neutral particles first have to transfer their energy onto charged particles to be measured. Photons produce free electrons in all of their fundamental interactions, neutrons have to collide with atomic nuclei and produce protons.

In order to measure a particles total amount of kinetic energy it has to be

completely absorbed and its energy converted into free electrons or light. This scales with energy better than other methods like tracking a particle and measuring its curvature in a magnetic field.

For particles with high energies, in the range of a couple MeV and above, measurements become more complicated as threshold energies for the production of different secondary particles are surpassed and particle cascades are produced. Decelerated electrons produce photons as so called bremsstrahlung. Above about 1 MeV photons are able to convert into electron positron pairs. And heavier hadrons induce fission and spallation. To understand the production and development of these particle showers and the measures taken to determine the incident particle energy the specific particle interactions have to be studied.

1.1 Particle Interaction with Matter

1.1.1 Ionization and Excitation of Charged Particles

The particle mass and charge play a role in interaction cross sections, so that a distinction can be made between the light electron and heavier particles such as the muon, pion and other hadrons or heavy ions. The average energy loss dE per length dx can be described by the Bethe-Bloch formula given by [1]

$$-\frac{dE}{dx} = 4\pi N_A r_e^2 m_e c^2 z^2 \frac{Z}{A} \frac{1}{\beta^2} \left(\ln \frac{2m_e c^2 \gamma^2 \beta^2}{I} - \beta^2 - \frac{\delta}{2} \right) \quad (1.1.1)$$

with

z - charge of the incident particle in units of the elementary charge

Z, A - atomic number and atomic mass of the absorber

m_e - electron mass = 511 keV/c²

r_e - classical electron radius ($r_e = \frac{1}{4\pi\epsilon_0} \frac{e^2}{m_e c^2}$ with ϵ_0 - permittivity of vacuum)

N_A - Avogadro number (= number of atoms per mol) = $6.022 \cdot 10^{23} \text{ mol}^{-1}$

I - mean ionization energy, characteristic of the absorber material, which can be approximated by

$$I = 16 Z^{0.9} \text{ eV} \quad \text{for } Z > 1.$$

δ - describes how much the incident relativistic particle is screened by the charge density of the atomic electrons effectively reducing the field seen by the passing particle lowering the energy lost. This correction is important for dense matter, for gases under normal pressure it can be neglected.

$\frac{dE}{dx}$ is usually given in MeV/(g/cm²). This makes it largely independent of the properties of the material since dx is the area density which is density (g/cm³) times length (cm); $dx = \rho ds$.

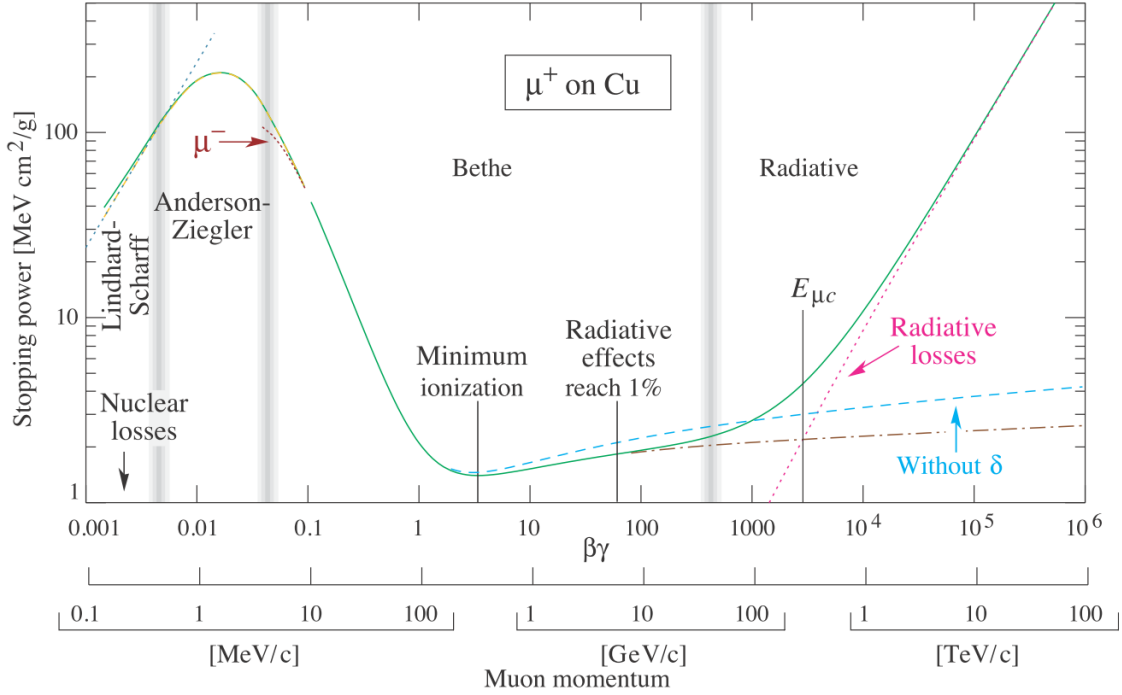


Figure 1.1: Stopping power ($-\frac{dE}{dx}$) of positive muons in copper as a function of $\beta\gamma = p/Mc$. The solid curve shows the total stopping power. Vertical lines show approximations of where different effects take over. Processes at the lower end are not discussed here but can be found with this image at [2, p. 324].

With rising energy the energy loss declines until a broad minimum is reached at around $\beta\gamma = 4$ as seen in figure 1.1, an exemplary depiction of muon energy losses over a wide energy scale. Particles in this energy region are called *minimum-ionizing particles* (MIPs). The increase in energy loss thereafter is due to the logarithmic rise of the term $\ln \gamma^2$.

Equation (1.1.1) only describes the average energy loss. The actual transmitted energy underlies statistical fluctuations which average out over the traveled distance. These fluctuations however play a big role in *thin* detectors in which only a fraction of the total energy can be deposited. This behavior can be described by a *Landau distribution* given by [1]

$$L(\lambda) = \frac{1}{\sqrt{2\pi}} \cdot \exp\left(-\frac{1}{2}(\lambda + e^\lambda)\right) \quad (1.1.2)$$

where λ describes the difference between the actual (ΔE) and *most probable* energy loss (ΔE^W) in a layer of thickness x ,

$$\lambda = \frac{\Delta E - \Delta E^W}{\xi} \quad (1.1.3)$$

with

$$\xi = 2\pi N_A r_e^2 m_e c^2 z^2 \frac{Z}{A} \frac{1}{\beta} \rho x \quad (1.1.4)$$

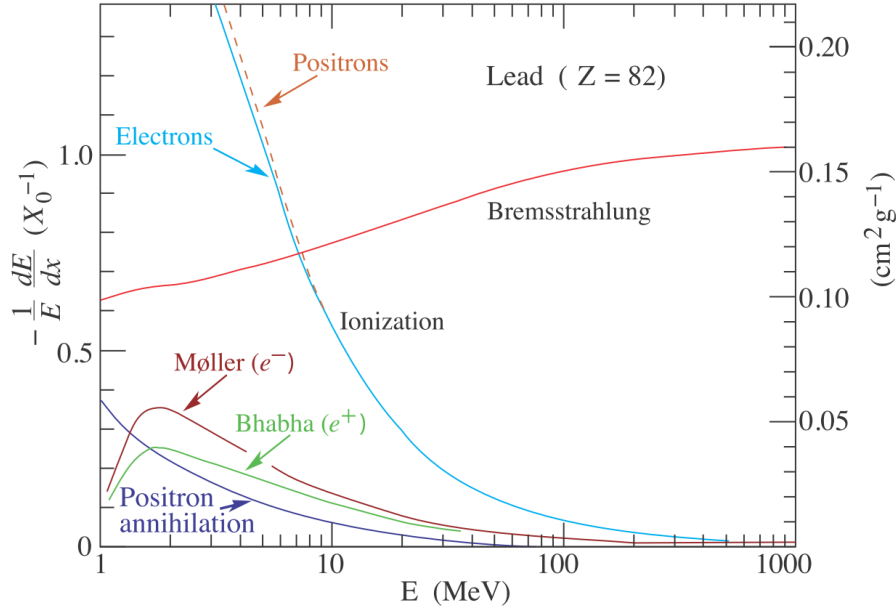


Figure 1.2: Energy loss per radiation length X_0 for electrons or positrons in lead vs energy.

and the formula for the most probable energy loss

$$\Delta E^W = \xi \left[\ln \left(\frac{2m_e c^2 \gamma^2 \beta^2}{I} \right) + \ln \frac{\xi}{I} + 0.2 - \beta^2 - \delta(\beta\gamma) \right]. \quad (1.1.5)$$

Up until now only ionization and excitation by heavy particles have been discussed. Electrons are a special case because their mass is equal to that of their collision partners, the electrons in the atomic shells. The low mass also makes other mechanisms, as can be seen in figure 1.2, more prominent. An equation similar to the Bethe formula (1.1.1) can be found for electrons

$$-\frac{dE}{dx} = 4\pi N_A r_e^2 m_e c^2 \frac{Z}{A} \frac{1}{\beta^2} \left[\ln \frac{m_e c^2 \gamma \beta \sqrt{\gamma - 1}}{\sqrt{2}I} + \frac{1}{2}(1 - \beta^2) - \frac{2\gamma - 1}{2\gamma^2} \ln 2 + \frac{1}{16} \left(\frac{\gamma - 1}{\gamma} \right)^2 \right] \quad (1.1.6)$$

and positrons; the latter mainly distinguished by their opposite charge and the fact that they annihilate with electrons.

$$-\frac{dE}{dx} = 4\pi N_A r_e^2 m_e c^2 \frac{Z}{A} \frac{1}{\beta^2} \left\{ \ln \frac{m_e c^2 \gamma \beta \sqrt{\gamma - 1}}{\sqrt{2}I} + \frac{\beta^2}{24} \left[23 + \frac{14}{\gamma + 1} + \frac{10}{(\gamma + 1)^2} \frac{4}{(\gamma + 1)^3} \right] \right\} \quad (1.1.7)$$

Positrons do not immediately annihilate with electrons in their vicinity. The cross section for annihilation is proportional to the atomic number and decreases with increasing positron energy and is given by

$$\sigma(Z, E) = \frac{Z\pi r_e^2}{\gamma + 1} \left[\frac{\gamma^2 + 4\gamma + 1}{\gamma^2 - 1} \ln \left(\gamma + \sqrt{\gamma^2 - 1} \right) - \frac{\gamma + 3}{\sqrt{\gamma^2 - 1}} \right]. \quad (1.1.8)$$

In addition to the above described ionization losses of electrons and positrons, these particles undergo Møller (electron-electron) and respectively Bhabha (electron-positron) scattering. These differ from ionization by the amount of energy transferred in single collisions. Is the energy below 0.255 MeV it is considered ionization, above that threshold it is Møller / Bhabha scattering.

1.1.2 Bremsstrahlung

From electrodynamics it is known that accelerated charges emit electromagnetic radiation; photons. This applies to all charged particles. Being surrounded by atoms they decelerate in their coulomb fields emitting bremsstrahlungs photons. The resulting energy loss can be described by [1]

$$-\frac{dE}{dx} \approx 4\alpha \cdot N_A \frac{Z^2}{A} \cdot z^2 \left(\frac{1}{4\pi\epsilon_0} \cdot \frac{e^2}{mc^2} \right)^2 \cdot E \ln \frac{183}{Z^{1/3}} \quad (1.1.9)$$

with Z and A being the atomic number and weight of the medium and z, m, E charge number, mass and energy of the incident particle.

The cross section for Bremsstrahlung is proportional to the inverse of the mass squared of the incident particle. Therefore, the contribution to electron and positron interactions has to be considered in the relevant energy regime while these losses are negligible for heavier particles.

The energy loss for electrons in equation (1.1.9) can be parameterized by

$$-\frac{dE}{dx} = \frac{E}{X_0}. \quad (1.1.10)$$

The constant X_0 , usually measured in g/cm², describes the distance traveled by a high energy electron, dominated by bremsstrahlungs losses, until its energy is reduced by a factor of 1/e. X_0 is called the *radiation length*.

Taking other effects into account, like bremsstrahlung caused by the coulomb fields of other electrons and screening effects of these electrons on the coulomb field of the nuclei, the radiation length can be better approximated by [1]

$$X_0 = \frac{716.4 \cdot A[\text{g/mol}]}{Z(Z+1) \ln(287/\sqrt{Z})} \quad [\text{g/cm}^2]. \quad (1.1.11)$$

1.1.3 Cherenkov Radiation

The speed of light in vacuum c is its upper limit. However the velocity of light is not constant, since electromagnetic waves travel through a medium depending on the index of refraction $n = v_m/v_V$. Relativistic particles are able to reach velocities above the corresponding speed of light in a medium. Charged particles above the respective speed of light emit so called *Cherenkov radiation*.

This radiation forms a cone behind the particle similar to a sonic shock wave of a faster-than-sound object. The angle of this cone to the trajectory of the particle is well defined as

$$\theta_C = \frac{1}{\beta n(\omega)}, \quad (1.1.12)$$

depending on the speed $\beta = v/c$ and the emitted frequency, for particles in infinite, nondispersive material.

The emission of photons constitutes an energy loss that can be described by [3]

$$-\frac{dE}{dx} = z^2 \frac{\alpha \hbar}{c} \int \omega d\omega \left(1 - \frac{1}{\beta^2 n^2(\omega)} \right) \quad (1.1.13)$$

integrating over all emitted wavelengths and depends on the charge and speed of the particle traveling through the medium. These losses increase with higher velocities but are at about 10^{-3} MeVcm²/g still small compared to ionization losses.

The spectra of light emitted by these faster-than-light particles does not show any spectral lines as seen in other emission spectra. The emitted wavelengths follow a continuous distribution with higher intensities at shorter wavelengths. In fact most of the light is in the ultra violet spectrum. This distribution is described by the *Frank-Tamma formula* of which equation (1.1.13) is derived off.

1.1.4 Photon Interactions

Photon carry no charge so they do not lose energy by gradual ionization. Their behavior is different to the previously discussed interactions. They are either scattered under a large angle in *Compton scattering* or absorbed completely in *the photoelectric effect* and *pair production*. This means that there is a decrease in photon numbers moving forward rather than a decrease in photon energy by photons traveling through matter. This attenuation can be described exponentially

$$I = I_0 \cdot e^{-\mu x} \quad \text{with} \quad \mu = \frac{N_a}{A} \sum_i \sigma_i \quad (1.1.14)$$

with μ being the *mass attenuation coefficient* and σ_i the cross section of process i . With increasing energy different effects dominate the interaction process.

1.1.4.1 Photoelectric Effect

Electrons are able to absorb a photon and its energy completely. Due to momentum conservation the interaction with a free electron is not possible. In an atomic field the nucleus serves as a third interaction partner absorbing part of the momentum. Proximity to the nucleus increases the chances for the photoelectric effect to occur at a particular electron. This causes a significant rise in cross section when the photon energy surpasses the excitation energy for K shell electrons. Apart from the absorption edges of the different shells, the cross section can be described by the non-relativistic *Born approximation* [1]

$$\sigma_{photo} = \left(\frac{32}{\varepsilon^7} \right)^{1/2} \alpha^4 Z^5 \sigma_{Th}^e \quad [\text{cm}^2/\text{atom}] \quad (1.1.15)$$

with $\varepsilon = E_\gamma/m_e c^2$ as the reduced photon energy and $\sigma_{Th}^e = \frac{8}{3} \pi r_e^2 = 6.65 \cdot 10^{-25}$ cm² as the Thomson cross section. At higher energies ($\varepsilon \gg 1$) the energy dependence decreases to $\sim \frac{1}{\varepsilon}$.

1.1.4.2 Compton Scattering

The Compton effect is the scattering of photons on a quasi-free electron, transferring energy and changing its direction up to 180°. At energies where Compton scattering becomes significant the binding energy of the scattered electrons can be neglected.

The cross section for a single electron is given by

$$\sigma_c^e = 2\pi r_e^2 \left[\frac{1 + \varepsilon}{\varepsilon^2} \left(\frac{2(1 + \varepsilon)}{1 + 2\varepsilon} - \frac{1}{\varepsilon} \ln(1 + 2\varepsilon) \right) + \frac{1}{2\varepsilon} \ln(1 + 2\varepsilon) - \frac{1 + 3\varepsilon}{(1 + 2\varepsilon)^2} \right] \quad (1.1.16)$$

with $\varepsilon = E_\gamma/m_e c^2$ as the reduced photon energy. The energy dependence at high energies can be estimated to be

$$\sigma_c^e \sim \frac{\ln \varepsilon}{\varepsilon}. \quad (1.1.17)$$

The transferred energy from photon to scattered electron depends on the angle of the scattered photon with respect to the initial direction. The energy ratio of scattered to initial photon energy is given by [1]

$$\frac{E'_\gamma}{E_\gamma} = \frac{1}{1 + \varepsilon(1 + \cos \theta_\gamma)}. \quad (1.1.18)$$

The maximum transferable energy is observed for back scattered photons, photons with a scattering angle of $\theta_\gamma = 180^\circ$. Above 1 MeV the scattered electron already receives over 80 % of the initial energy.

1.1.4.3 Pair Production

With rising energy a point is reached where the energy of a photon is sufficient to convert into an electron-positron pair. The isolated production of two particles from one photon would violate the momentum conservation. For this reason this effect is only observed in the vicinity of a third particle absorbing part of the momentum. The threshold energy for this production lies at the rest mass of the produced leptons¹ and the fraction the other particle absorbs ($2\frac{m_e}{m_i}c^2$), which can be neglected for large mass differences as in case of a nucleus.

The cross section for higher energies², where screening effects have been taken into account can be described by [1]

$$\sigma_{pair} = 4\alpha r_e^2 Z^2 \left(\frac{7}{9} \ln \frac{138}{Z^{1/3}} - \frac{1}{54} \right) \quad (1.1.19)$$

This equation is energy independent and, neglecting the second term, can be rewritten as

$$\sigma_{pair} \approx \frac{7}{9} \cdot \frac{A}{N_A} \cdot \frac{1}{X_0}. \quad (1.1.20)$$

¹ $2m_e c^2 = 511 \text{ keV}$

² $\varepsilon > \frac{1}{\alpha Z^{1/3}}$

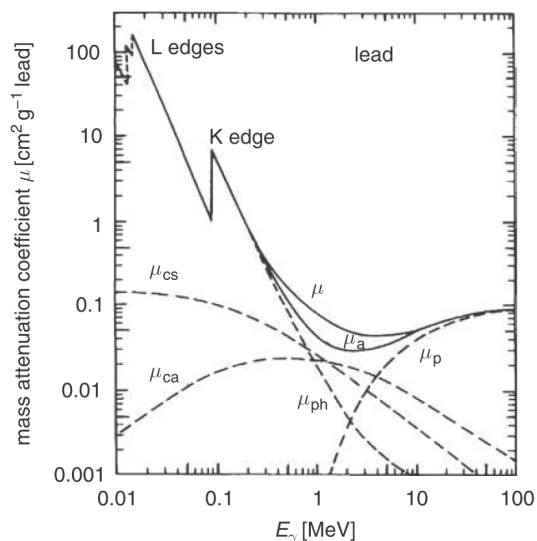


Figure 1.3: The mass attenuation of photons in lead.

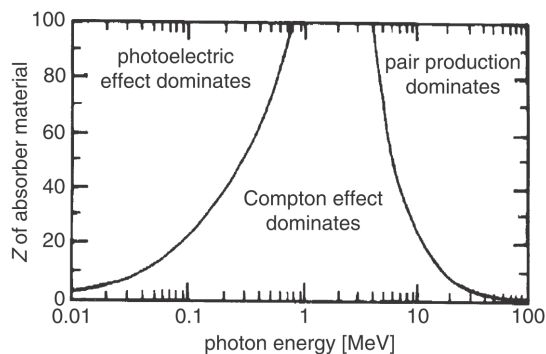


Figure 1.4: A comprehensive visualization of which effects dominate at a certain energy and atomic number. The lines indicate where neighboring cross sections are equal.

This leads to a possible comparison of electron and photon interaction lengths of X_0 for electrons and $\frac{9}{7}X_0$ for the average length before pair production for photons.

Without the screening effects at low energies, where the electron needs to be close to the nucleus to interact, the cross section becomes proportional to $Z^2 \cdot \ln E_\gamma$.

The energy distributions of the positron and electron are similar at low energies. At higher energies the energy splitting becomes asymmetric.

Due to the with energy increasing cross section pair production becomes the primary mode of interaction above a few MeV.

1.1.4.4 Total Mass Attenuation

The combined effect of the Photo and Compton effect as well as the pair production gives us the mass absorption coefficient defined in equation (1.1.14). As an example, the energy dependence of μ is shown for lead in figure 1.3. With increasing energy the dominating photon interaction changes from the photoelectric to the Compton effect and the pair production. The transition point depends on the atomic number of the surrounding material as seen in figure 1.4.

1.1.5 Nuclear Interactions

As energies rise, and particles have enough energy to penetrate the electric fields of the electron shell and the nucleus, nuclear interactions start to occur. Particles such as protons and neutrons and other high energy hadrons are able to hit nuclei. If this happens at relativistic energies *spallation*, the emission of nucleons out of

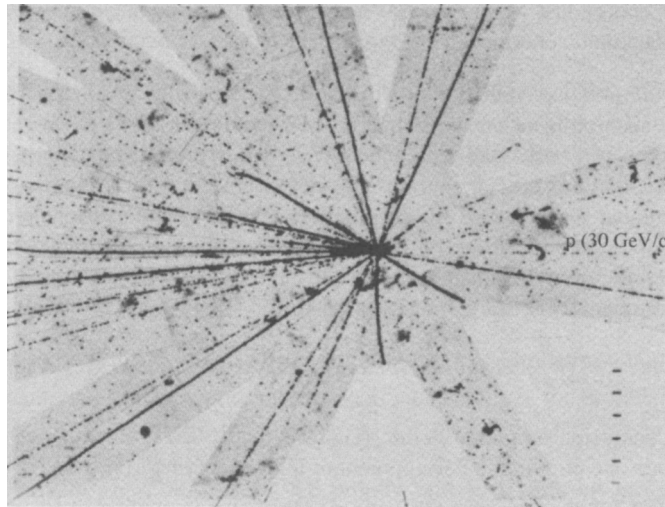


Figure 1.5: A nuclear reaction between an atomic nucleus and a proton of 30 GeV/c entering from the right [4].

the nucleus, and *fission*, the splitting of the nucleus into lighter nuclei occurs.

The emission in the spallation process happens in two steps. First the incoming particle collides with quasi free nucleons, transferring energy and knocking them out of the nucleus in a cascade type manner. After that the remaining excited nucleus relaxes via particle evaporation or fissioning. Neutrons constitute the majority of the evaporated particles since protons have to overcome a higher binding energy due to their charge. If the remaining excitation energy is lower than the binding energy of nucleons, the energy is released via γ radiation.

In addition to that, similarly to the pair production of photons, hadrons can be produced in these interactions as long as their production energy threshold is exceeded. Since π^0 are the lightest hadrons they are predominantly produced in these interactions along with the slightly heavier π^\pm .

Such a process of a 30 GeV/c proton interaction with an atomic nucleus has been captured in a photographic emulsion at CERN and can be seen in figure 1.5. The incident proton is entering from the right and hitting a nucleus in the center. Thick lines indicate strong ionization e.g. by protons being emitted almost isotropically. Lighter tracks roughly in the direction of the incident particle are most likely mesons such as pions. Neutrons can not be visualized in this picture since they are not directly ionizing.

1.2 Shower Development

As discussed in the previous chapter 1.1, particles traveling through a medium at high energies produce secondary particles. Electrons³ emit photons via bremsstrahlung. Photons on the other hand produce electrons predominantly via pair production. This interplay of bremsstrahlung and pair production produces an

³from here on electrons refer to both electrons and positrons

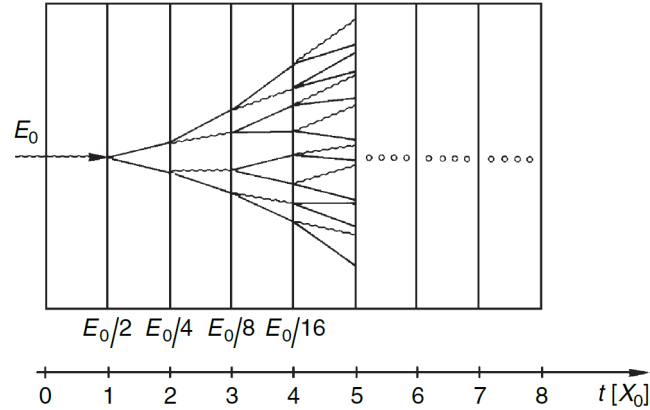


Figure 1.6: Shower development of an incoming photon, drawn as a wavy line, with the energy E_0 . Produced electrons are shown as straight lines. The vertical lines illustrate the development considering the radiation length [5].

increasing number of photons and electrons cascading through the material forming an *electromagnetic* (em) shower.

Showers initiated by other particles include *em* sub-showers but develop in a more complicated manner. For this reason they will be treated separately in the section 1.2.2.

1.2.1 Electromagnetic Shower

An incoming photon of sufficient energy produces an electron-positron pair, after about one radiation length ($9/7X_0$) on average. Electrons at comparable energies on the other hand produce photons of varying energies continually via bremsstrahlung.

These complementary interactions of electrons and photons produce a growing shower of particles, cascading through the medium as one can see in figure 1.6. A useful way to look at shower development is by normalizing the distance to radiation lengths, $t = x/X_0$, making the plot generally material independent. Some typical values for the radiation length and critical energy can be seen in table 1.1.

Table 1.1: Short list of radiation lengths and critical energies of some absorber materials [5]

Material	Z	A	X_0 [g/cm ²]	X_0 [cm]	E_c [MeV]
Carbon	6	12.01	43	18.8	90
Aluminium	13	26.98	24	8.9	40
Iron	26	55.85	13.9	1.76	20.7
Tungsten	74	183.9	6.8	0.35	8
Lead	82	207.2	6.4	0.56	7.4

A simplified model helps to understand the basic properties of an electron cascade. Looking at the shower production again, one photon creates an electron pair after about one radiation length. After another radiation length each electron emits a

bremstrahlungs photon of sufficient energy to each undergo pair production. Under the assumption that energy is distributed equally at each particle interaction, an estimation for the amount of particles in the shower can be calculated,

$$N(t) = 2^t \tag{1.2.1}$$

where each particle of the generation t has the Energy

$$E(t) = E_0 \cdot 2^{-t}. \tag{1.2.2}$$

This cascade will spread as long as new particles are created. As the energy per particle drops and eventually falls below the critical value E_c the probability for absorption increases, and processes such as ionization for electrons and Compton scattering and the photoelectric effect start to dominate.

The critical energy E_c has different definitions. One is that E_c is the energy at which the energy loss due to ionization and bremsstrahlung become equal. On the other hand *Bruno Rossi* defines the critical energy as, when the ionization loss per radiation length is equal to the electron energy itself [2, p. 331]. These definitions become equivalent when considering equation (1.1.10) although they show slight differences in experiment. Once this energy is reached the number of particles starts to decrease since the remaining energy is not sufficient to produce new ones.

At this stage the maximum shower position is reached.

$$E_c = E_0 \cdot 2^{-t_{max}} \tag{1.2.3}$$

$$\Rightarrow t_{max} = \frac{\ln(E_0/E_c)}{\ln 2}. \tag{1.2.4}$$

As an example a typical shower of a 2 GeV photon hitting iron with a critical energy $E_c \approx 20$ MeV can be calculated. This shower yields about $E_0/E_c = 100$ particles in the shower maximum at a depth of $\approx 6.6X_0$. Electrons at this point will give off all their remaining energy in about one radiation length. Photons however travel further creating new free electrons along their way.

Monte Carlo simulations for such shower developments can be seen in figure 1.7 and 1.8. Figure 1.7 shows a typical energy deposition distribution for a 30 GeV electron in iron. The graph is also split up into electrons and photons visualizing the number of particles crossing each plane.

Actual electromagnetic cascades have a more complex shower development than depicted in figure 1.6 and are difficult to describe analytically. A numerical approach does suffice with the computing power available today.

Although the radiation length X_0 was designed to give material independent behavior e.g. for the shower development, looking at figure 1.8 shows a clear Z dependence.

The fraction of the total energy deposition in the detector by particles of different energies also depends on the material. This is shown by a Monte Carlo simulation seen in figure 1.9. The majority of the energy is deposited by electrons under 4 MeV with a significant fraction under 1 MeV.

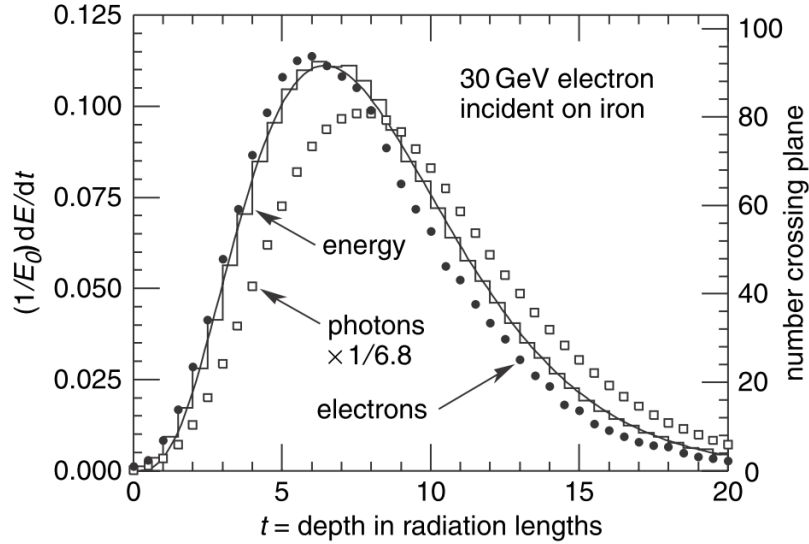


Figure 1.7: Monte Carlo simulation of the longitudinal shower development of a cascade induced by a 30 GeV electron. The energy loss is depicted as the solid histogram with the electrons as solid dots, and photons as open squares, above 1.5 MeV. [4].

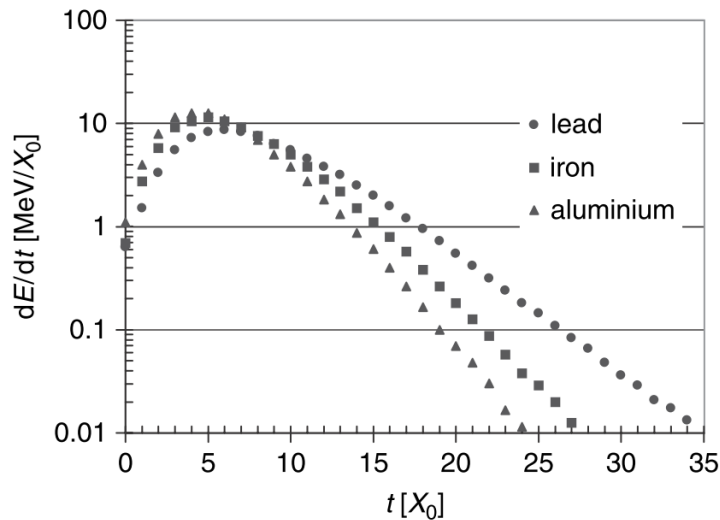


Figure 1.8: Monte Carlo simulation for the development of the energy loss of electromagnetic showers for a 10 GeV electron in different absorber materials [5].

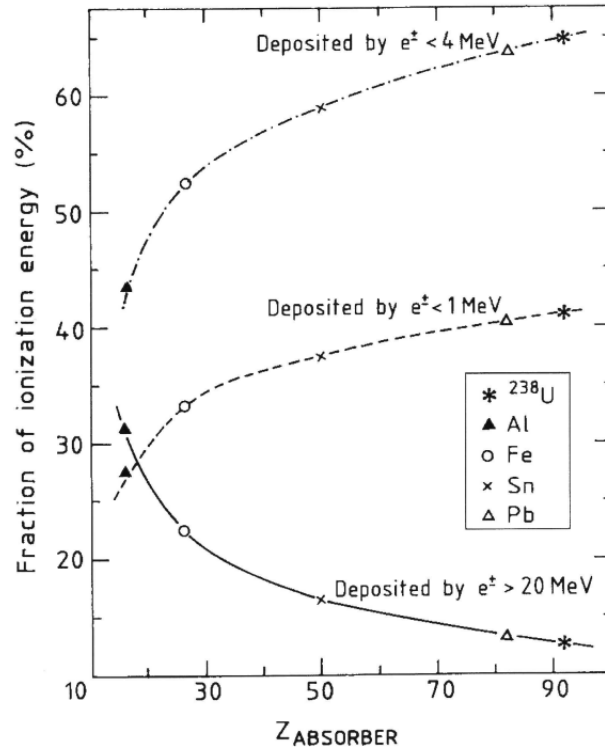


Figure 1.9: Simulation of the fraction of the total energy deposition by particles at different energies in different absorber materials for a 10 GeV *em* shower [4].

The lateral width of the shower is mainly determined by multiple scattering since bremsstrahlung and pair production have a narrow angular distribution. For a containment level of 90% the width can be described by the Molière radius

$$R_M = \frac{21 \text{ MeV}}{E_c} X_0 [\text{g/cm}^2] \quad (1.2.5)$$

and $2R_M$ for a 95% containment level. This is almost independent of the energy of the incident particle [5].

1.2.2 Hadronic Shower

Hadronic showers follow the same basic principals as *em* showers but in addition to their electromagnetic interactions, hadrons undergo processes of the *strong force*. The main difference is the scale of the shower process. The longitudinal development of hadronic showers is described by the *interaction length* λ_I which can be estimated to an accuracy of 0.8% by [2, p. 360]

$$\lambda_I = 37.8 \text{ g/cm}^2 A^{0.312} \quad \text{for } Z > 15. \quad (1.2.6)$$

The value for the nuclear interaction length, depending on the material, is much larger than the corresponding radiation length X_0 . As an example the radiation length X_0 for lead is 6.37 g/cm^2 while λ_I is 199.6 g/cm^2 . For carbon however it would be $X_0 = 42.7 \text{ g/cm}^2$ and $\lambda_I = 85.8 \text{ g/cm}^2$. As a consequence much more

material is needed to contain a hadronic shower. Detectors are usually built to be about 5 to 8 λ_I long.

Charged hadrons show a continual energy loss through ionization similar to electrons. At some point however the incident hadron will interact with a nucleus in strong interaction producing new hadrons and possibly changing its own particle identity.

Particles produced in such strong interactions are foremost pions (π^0, π^\pm). Some particles such as π^0 s or η s decay electromagnetically into two or more photons $\pi^0, \eta \rightarrow \gamma\gamma$, creating subsequent *em* showers. About one-third of the mesons produced in a nuclear reaction are π^0 s. This suggests an exponential scaling of the electromagnetic shower fraction f_{em} of

$$f_{em} = 1 - \left(1 - \frac{1}{3}\right)^n, \quad (1.2.7)$$

since each new generation of hadrons n is left with 2/3 of the energy to produce new π^0 , until the energy drops below the π^0 production threshold.

This simplistic approach neglects some important dependencies e.g. that the pion fraction (f_{π^0}) of 1/3 is only an upper limit, that ionization losses are strongly media dependent, or that the average number of produced mesons, the multiplicity $\langle m \rangle$, increases slightly with energy. A better estimation is given by [4]

$$f_{em} = 1 - \left(\frac{E}{E_0}\right)^{(k-1)} \quad (1.2.8)$$

where E_0 is a scaling factor equal to the average energy needed to produce a π^0 . The exponent k depends on the multiplicity and the fraction of π^0 production and typically has a value of around 0.8. It has been found that E_0 seems to be Z dependent whereas k hardly is.

A dependence on the initial particle also has been found. Proton induced showers show a 15% smaller *em* shower fraction than showers caused by incident pions of the same energy. This is due to quantum mechanical effects in the interactions. The baryon number is a constant that must be conserved in each interaction limiting the energy available for meson production. This constraint does not limit pion production for pion interactions.

In addition to the newly produced particles, fission and spallation products such as protons and neutrons are emitted.

The average shower development shows a sharp rise and a slow falloff longitudinally similar to *em* showers only over about eight λ_I . The lateral profile shows a narrow core at which most of the energy is deposited with exponentially falling intensity to the sides. In comparison to *em* showers the width of hadronic showers is about 9 times wider. This is caused by the energy transferred to fission fragments spreading laterally. The longitudinal dimensions turn out to be about 9 times larger too resulting in the necessity to use $9 \cdot 9 \cdot 9 \approx 700$ times the material to contain hadronic showers.

Single shower profiles may look significantly different to the average profile since the shower development depends heavily on the pion production as seen in figure

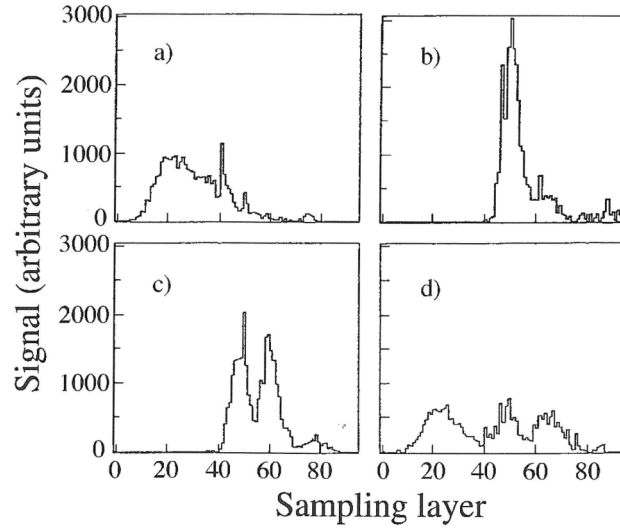


Figure 1.10: Different longitudinal shower developments for 4 different events of incident 270 GeV pions in a lead-iron-plastic sampling calorimeter [4].

1.10. Profile a) shows a typical development close to the average of many such interactions. Profiles b) and c) however show interactions where an incident pion was able to travel a long way before interacting with a nucleon transferring a large fraction of the energy onto one or many π^0 in the first respectively and second interaction. Since these pions produce *em* showers the density of the deposited energy is much greater than for other shower components. The short range of *em* showers leads to a sharp fall off in transferred energy. From figure 1.10 b) to c) to d) the increase of pion generations from 1 to 2 to 3 can be clearly distinguished.

Fluctuations in π^0 production influence the fraction of the electromagnetic shower components. This fluctuation leads to challenges for the detection process as explained later in section 1.4.3.

1.3 Desirable Properties for Calorimeter

Depending on the specific experimental goals and specifications the property of the calorimeter has to be adapted. Some technical aspects are the following [6].

- **Energy resolution** The quality of experimental results is determined by the resolution achieved by the detector. This resolution depends on fluctuations in the absorption process; variances in the way the shower develops and is registered. In case of stochastic fluctuations, that obey i.e. Poisson statistics, the relative energy resolution should improve with increasing energy providing increasing statistics as

$$\frac{\sigma}{E} \sim \frac{1}{\sqrt{E}}. \quad (1.3.1)$$

As energies rise non-stochastic effects play an increasing role in decreasing the resolution and limiting the overall measurement quality adding a constant

term quadratically.

$$\frac{\sigma}{E} \approx \frac{c_1[\%]}{\sqrt{E[\text{GeV}]}} \oplus c_2[\%] \quad (1.3.2)$$

- **Size** To limit some of the non-stochastic fluctuations it is important to have a detector of sufficient size. Higher energy means a wider spread of the particle shower in the material. If the size of the absorber is too small parts of the shower may leak, in other words leave the detector without being registered. Through this leakage important information is lost and fluctuations of the leakage leads to a degraded resolution. It is impossible to capture 100% of the shower as particles can leave through the front of the detector, but sufficient depth has a high priority.
- **Signal speed** Depending on the setup of the experiment, signal speed can play a big part in the functionality of the detector. In large, complex experiments, such as ATLAS or CMS at CERN or PANDA at FAIR, with high interaction rates, overlap of the produced signals would lead to incorrect measurements. A fast signal decay time is necessary.
- **Spacial resolution** In experiments where interactions need to be reconstructed and distinguished from other interaction vertices sufficient spatial resolution is important. In order to reconstruct the decay of a π^0 two separate but correlated photons need to be detected. To ensure such separation the calorimeter has to be segmented.
- **Hermeticity** To ensure accurate reconstructions i.e. of π^0 or η decays both photons need to be detected. Also to apply techniques such as 'missing mass' the detection of all detectable particles has to be ensured. In order to do that the calorimeter has to cover the entire 4π solid angle around the interaction vertex.

This poses a challenge for the construction since one needs to create space for the readout system. To meet the tight needs different setups have been designed. These are discussed in section 1.4.

- **Radiation hardness** As time goes on material in high radiation environments is subjected to aging effects degrading the quality of the detector. This poses a considerable problem especially in collider experiments with ongoing particle collisions and consequent radiation multiple times a second. The radiation hardness of the used materials is important in order to prolong the modules lifetime.

1.4 Calorimeter Setups

Depending on the experimental conditions and performance requirements different concepts for calorimetry are possible. The optimum performance for electromagnetic calorimeters, focused on the measurement of photons and electrons, can be

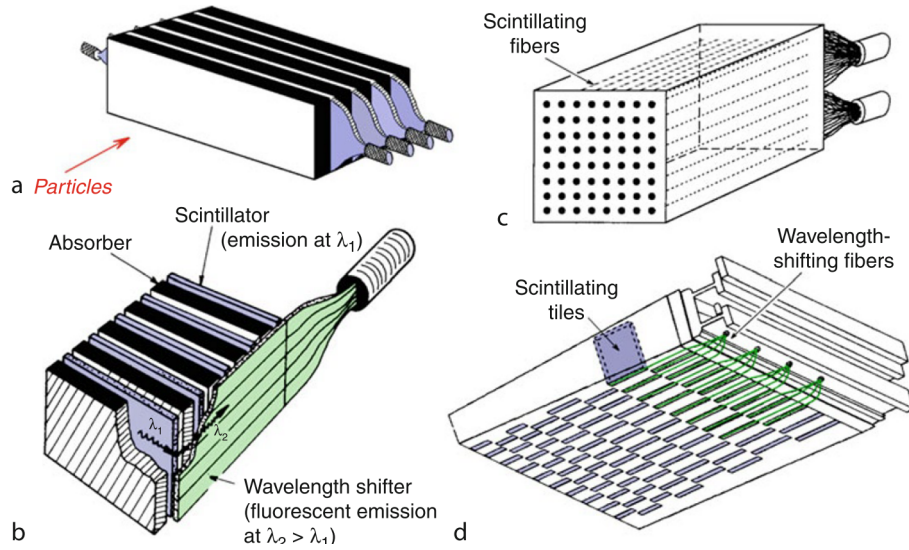


Figure 1.11: Different designs for sampling calorimeter: **a)** scintillating plates in between absorber read out by PMTs, **b)** Scintillating plates read out together by wavelength shifting plates, **c)** scintillating fibers read out by PMTs, **d)** scintillator tiles oriented longitudinally coupled to wavelength shifting fibers [6].

achieved by *homogeneous calorimeters* composed of heavy inorganic crystals for example. An alternative to homogeneous calorimeters is a *sampling calorimeter*. Built out of multiple detector layers sandwiched with inactive absorbing material in different configurations. High Z materials are used as absorbers causing incoming particles to cascade and lose energy. The active part consists of signal generating materials connected to the readout electronics such as gases, liquid gases, solid state detectors or scintillators.

1.4.1 Homogeneous Calorimeter

Homogeneous calorimeters are made of material that combines the roles of an absorber, inducing the energy transfer from particles to the detector, and active material producing measurable signals. This makes the whole detector sensitive to radiation.

In a best case scenario the measured particle is supposed to produce a shower that is contained in and deposits all its energy inside the detector. By the simple model of section 1.2 the amount of produced particles depends on the incident energy linearly; $N = E_0/E_c$. This suggests a linearity of the detector signal, creating signals twice as strong for particles with double the energy. This however is not always the case. Non-linearities in the signal production and read out such as position dependencies of signal production and readout need to be considered and avoided as possible by using optimized materials.

A homogeneous calorimeter is not necessarily built out of one block. To achieve location sensitivity the material is segmented. Each segment is read out individually. This also makes for a simpler construction.

Due to their homogeneity and sensitivity throughout the detector which

converts the whole shower into a detector signal and provides a very good resolution, homogeneous calorimeters are the first choice for high precision electromagnetic calorimeters.

The use as hadronic calorimeters is limited due to the long interaction lengths of hadrons and the consequent size of the hadronic showers. Especially in hermetic setups a homogeneous hadronic calorimeter would need about 700 times more material than an electromagnetic calorimeter. Which at the moment is not financially feasible for the expensive materials needed.

1.4.2 Sampling Calorimeter

Contrary to homogeneous calorimeters *sampling calorimeters* are put together from different materials with different purposes, separating detection in the active material and cascade development in the passive material. Summarizing the ratio of active to passive material in a applicable way is the *sampling fraction* defined as the ratio of energy deposited in the active material to the total energy deposited by these particles.

They are attractive due to their simplicity and low cost. The most commonly used active type of material are scintillators that produce light in the visible and UV spectrum. Signal extraction for scintillators however presents a challenge since the light needs to be collected from every layer. In order to achieve hermetic calorimeters, single or double readout of every plane of active material can not take place at the edges as in figure 1.11 a). The development of wavelength shifters, absorbing light at one wavelength and reemitting it at another, has made it possible to read out multiple planes at once. The wls plate itself however takes up space that can not be used to produce particle signals causing possible energy and hence information loss. This problem could be avoided by using scintillating fiber in an absorber matrix in direction of the beam. This allows readout at the downstream end of the fiber and circumvents detection gaps caused by the readout system.

In sampling calorimeters the majority of the energy is deposited in the dead material. For this reason generally a worse resolution than for homogeneous calorimeters can be assumed. The restrictive factor however are fluctuations of the measured energy fraction. The contribution of these fluctuations to the resolution depends on a constant factor determined by the used materials as well as the *sampling fraction* f_{samp} and the thickness d of one active layer [4]

$$\left(\frac{\sigma}{E}\right) = c\sqrt{d/f_{samp}} \cdot \frac{1}{\sqrt{E}} \quad (1.4.1)$$

To reduce the sampling fluctuations and improve the resolution the fraction of measured energy can be increased, by increasing the total amount of active material. This increases the sampling fraction. Too much low Z active material however produces other problems associated with low density such as a wide shower spread that increases the risk of overlapping showers and an increase in necessary detector material.

As seen in equation (1.4.1) the resolution can be increased by reducing the thickness of the active/absorber layers while increasing the number of plates which

results in an increased sampling frequency. A large fraction of the deposited energy is lost by low energy electrons. In lead and iron such electrons have a range below 1 mm so only electrons produced at the back edge, the last few hundred μm , of the absorber manage to travel to the active material and produce signals. Increasing the fraction of contributing electrons reduces fluctuations.

1.4.3 Challenges of Hadron Callorimetry

As described in section 1.1.5 hadrons undergo nuclear interactions. In these interactions energy is spent to break up nuclear bonds via fission or spallation. Energy spent in this way is lost to detection. Furthermore it is very challenging to detect and measure neutrons and their energy as they must first transfer their energy onto charged particles like protons to create a measurable signal. Both of these effects contribute to the phenomenon of *invisible energy*.

This invisible energy leads to a diminished response for the non electromagnetic part of the shower, hence the signal produced by an electromagnetic cascade (e) is larger than that created by a hadronic one (h), $\frac{e}{h} > 1$. This disparity causes major resolution issues since the ratio of electromagnetic and hadronic shower energy varies from event to event depending on the pion production for example as seen in figure 1.10.

1.4.3.1 Compensation

To reduce this effect the response to the hadronic shower component (h) needs to be similar to the em component (e): $\frac{e}{h} = 1$. One possibility is to *reduce the em response*. This can be done by using high Z materials as absorber material in sampling calorimeters. These layers absorb a majority of the low energy photons due to the Z^5 dependency of the photoelectric effect that would otherwise ionize the active material. The em response can be further lowered by shielding the active layers from electrons freed at the boundary to the absorber, with a thin layer of low Z material in the range of a few hundred μm . This thin layer effectively prevents any low energy photoelectric electrons from crossing the boundary region to reach the active material.

The second possibility is to *enhance the hadronic response*. This is the more promising approach since any reduction in signal means a reduction in statistics which automatically degrades the resolution. One idea was to employ uranium as an absorber material to use the created neutrons to induce fission which would lead to excited daughter nuclei emitting charged particles and γ rays which then could be picked up again by the active material.

First good results were documented for a calorimeter with 1.7 mm uranium plates submerged in liquid argon with 2 mm gaps between the plates [7]. The main contribution to the resolution however turned out to be due to the damping effects on the em shower for high Z absorbers as described above.

A different approach is to try to transfer the neutron energy onto protons which in turn are able to ionize the active material. This can be done by using hydrogen rich materials for the active part of the detector.

Calorimeters that achieve a signal ratio $e/h = 1$ for em and hadronic showers are called *compensating*. Are the calorimeter parameters modified in a way to achieve $e/h > 1$ the calorimeter is *over-compensating* leading to a degradation of resolution since it suffers from the same limitations as non-compensating calorimeters.

The application of compensation in calorimeters is limited since signals can only be suppressed or enhanced to a certain degree. This means that only calorimeters with a small sampling fraction are able to be compensating. In addition to that neutrons travel relatively far reducing the inherent spacial resolution of these approaches.

1.4.3.2 Dual-Readout

A different approach is to estimate the fraction of electromagnetic shower in the overall shower f_{em} of every single event. Knowing this fraction allows an offline or calculated compensation. The deposited energy can be calculated by

$$S = c \left[1 + f_{em} \left(\frac{e}{h} - 1 \right) \right] E \quad (1.4.2)$$

with c as an empirical constant and e/h as the relation of the signal strength of em and hadronic shower.

In order to get to such an estimation two detector types can be combined; one part that reacts to ionizing radiation in general such as scintillators and a part that reacts to the em part. Due to the low mass of the electrons in the em shower they reach higher velocities for the same kinetic energy as particles in the hadronic shower, which leads to an almost exclusive sensitivity of the Cherenkov radiation to the electromagnetic part. This makes it possible for the latter part to be achieved by inserting material that creates Cherenkov light allowing an estimation of the em fraction of the overall shower.

1.4.4 Active Detector Material

Particle energy measurements can be performed by measuring the emitted Cherenkov radiation. The produced signal however is so small that in most cases detection via the ionization or excitation of the detector material, measured as a current of free electrons or emitted radiation due to de-excitation, delivers a superior performance due to better statistics.

An example of a calorimeter measuring ionization currents is the liquid argon calorimeter of the ATLAS experiment at CERN. This thesis however focuses on scintillators as are used to build the homogeneous electromagnetic calorimeter for the CMS experiment at CERN as well.

Scintillators are a class of material that is able to convert deposited energy into a measurable or even visible signal. In solid form they are available as organic plastic compounds or inorganic crystals, liquid and gaseous scintillators.

Since this study is about scintillating materials from here on designs using such materials will be discussed.

Scintillation is the secondary emission of light pulses after intrinsic excitation of the atoms when a particle passes through a certain optically transparent material.

This effect is not to be mixed up with the previously described Cherenkov effect. Materials with this quality are called scintillators. When this phenomenon was first discovered it was used for counting events just like the first measurements of Rutherford using scintillating screens. At that time there were no appropriate readout system available for qualitative and quantitative counting. With the invention of *Photo multiplier Tubes* (PMTs) the sensitivity to single photons and the intrinsic amplification allowed a measurement of the current signal at the last stage of these multi-stage devices. Devices like that opened up new possibilities since the amount of light emitted by the scintillator is correlated to the amount of energy deposited inside the material.

Many materials show this luminescence but not all are appropriate as detector material. In order to be of use they need a high conversion efficiency of excitation energy into photon yield and transparency to the corresponding wavelength range to be able to transmit the light internally to the readout system. The emitted light should be in a practical spectral range of the sensor sensitivity and the decay time of the emission process should be short enough to avoid overlapping signals at high event rates.

In organic scintillators the deposited energy excites molecular states of molecules embedded into a host material which then relax under photon emission. However, in most cases the primary emitter creates emission in the UV-range and would be self-absorbed in the medium. Therefore, the photons are shifted using several wavelength shifters to longer wavelengths adapted to the common photo sensors. The molecular excitation is almost independent of the state of the material which enables many shapes of organic scintillators. These materials usually have a very fast decay time and good light yield but lack stopping power due to the low Z -value of the composites and are primarily used for charged particle and not γ detection.

Inorganic scintillators are the other major group of materials used in detection physics and the main focus of this work. They are insulators, usually used in crystalline form. Being insulators they have a distinct band gap between their highest filled band of electron states, the valence band and the next highest band the conduction band. The excitation occurs inside these energy bands arising from the crystal structure of the atoms. The by radiation excited electrons are lifted from the valence band to the conduction band. In the conduction band they are free to migrate throughout the crystal until they release their energy again.

The de-excitation from the conduction to the valence band via photon emission is an inefficient process since it often de-excites non radiatively and due to the high probability for self-absorption of the emitted photons. To enhance and optimize the emission a so called *Stokes shift* between absorption and emission can be provided by creating activators or luminescence centers. These activators create energy states in between the valence and conduction band, depending on which materials are used. From these states photons with a longer wavelength are released. This longer wavelength prevents the re-absorption of the photons.

Inorganic scintillators have a wide range of decay times. The light yield varies strongly from material to material depending on different mechanisms. The big advantage is the density and hence the stopping power. This makes for good

detector material especially in high energy physics.

1.4.4.1 Material

For calorimeter setups there is a variety of scintillating materials to choose from. The choice depends on different factors determined by the specific application, like the type of interaction and their products that are to be studied. Decay channels with many photons may call for a high resolution electromagnetic calorimeter. Other factors to consider are the *density* ρ and connected to that the *radiation length* X_0 and the *Molière radius* R_M , as well as the *wavelength* of the emission spectrum peak λ_{\max} , the *decay time* τ and the *light yield*. The light yield is usually given in comparison to NaI(Tl) as it is a material that has been popular since early on with a high light yield of about 40 000 photons /MeV [2, p. 344]. It is still one of the most common and widely used materials.

Despite its popularity it has some drawbacks. It is highly hygroscopic, meaning it attracts and absorbs water molecules from its environment changing and degrading its structure. The low density also limits the applicability for high energy applications. It was used in the crystal ball experiment from 1979 in Stanford at the SPEAR accelerator. An alternative is CsI, most commonly doped with thallium to increase the light yield by about one order of magnitude, which is used in multiple experiments such as CLEO II at CESR, Crystal Barrel at LEAR, KTeV at the Tevatron, BaBar at SLAC and BELLE at KEK. The material is quite rigid but the surface needs careful treatment.

BaF₂ is the fastest known inorganic scintillator with a decay time of its fast component below 1 ns. Its slow component however is much slower with about 630 seconds. It was used in the TAPS detector currently at MAMI and ELSA. Bismuth germanate (Bi₄Ge₃O₁₂ or BGO) is a dense and easy to handle material that was used in the L3 experiment at LEP. Even denser than BGO is lead tungstate (PbWO₄ or PWO). Its compactness due to its short radiation length made it the material of choice for the CMS experiment at the LHC at CERN as well as for PANDA and FAIR.

Promising materials are cerium doped lutetium oxyorthosilicate (Lu₂SiO₅:Ce or LSO:CE) and cerium doped lutetium-yttrium oxyorthosilicate (Lu_{2(1-x)}Y_{2x}SiO₅ or LYSO:CE). Both materials show excellent radiation hardness. Only LSO are listed in table 1.2 since their properties are very similar except for a lower density of LYSO which depends on the manufacturer's used yttrium fraction. Another radiation hard material is cerium fluoride (CeF₃) as a bright hard and dense crystal.

A material that is examined in this thesis, that has gained interest for specific applications is cerium doped *lutetium aluminium garnet* (Lu₃Al₅O₁₂) or short LuAG:Ce as well as Y₃Al₅O₁₂(Ce) or YAG:Ce⁴. It is further discussed later on.

1.4.5 Readout

In order to turn the scintillation light into an electric signal different devices need to be employed. The first device that made qualitative scintillation measurements

⁴from here abbreviated as LuAG and YAG

Table 1.2: List of inorganic scintillating material interesting for high energy physics applications, listing the radiation length X_0 , density ρ , signal decay time τ , wavelength of the signal maximum λ_{max} , light yield (LY) and melting point (MP). Double values belong to the fast respectively slow component of the scintillation light. [2] [8]

	NaI(TL)	BaF ₂	CsI(Tl)	CeF ₃	BGO	PWO	LSO	LuAG:Ce
X_0 [cm]	2.59	2.03	1.86	1.66	1.12	0.89	1.14	1.41
ρ [g/cm ³]	3.67	4.89	4.51	6.16	7.13	8.3	7.4	6.73
τ [ns]	245	0.9 650	1220	30	300	30	40	60
λ_{max} [nm]	410	220 300	550	310 340	480	425	402	535
LY [%NaI]	100	40	85	5	21	0.3	165	50
MP [°C]	651	1280	621	1430	1050	1123	2050	1980

possible is the **Photo-Multiplier Tube (PMT)**. The setup of such a PMT can be seen in figure 1.12. It consists of a photo-cathode turning initial photons into electrons. These are focused and accelerated onto dynodes that emit secondary electrons that are again accelerated onto another dynode multiplying the number of electrons in each step to reach a gain of about 10^6 . These electrons are all collected at the anode that produces a measurable electric charge. Due to their internal electric field accelerating the electrons from dynode to dynode, PMTs are sensitive to an external magnetic field limiting their use in large multilayer experiments.

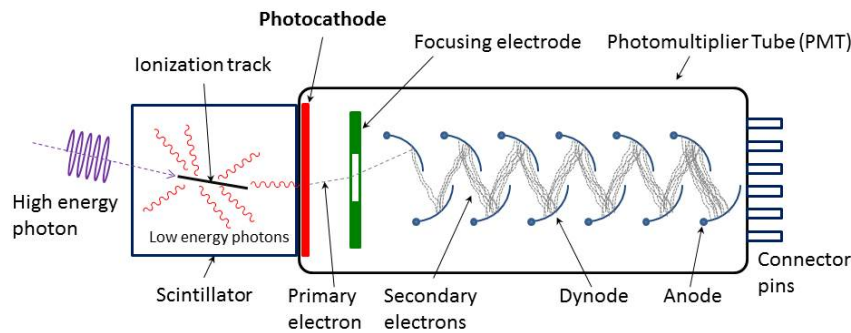


Figure 1.12: Schematic setup of a photo-multiplier tube coupled to a scintillator [9].

Smaller and less sensitive to magnetic fields are semiconductor devices such as **photodiodes**. Combining an n-doped and a p-doped semiconductor forms a diode with a depletion zone at the boundary between the materials, free of mobile charge carriers. If a reverse bias voltage is applied to such a diode the depletion zone grows and electron-hole pairs, that are created inside by incident photons via the photoelectric effect, are separated by the potential difference and produce a small current.

The produced signal is too small to measure single photons. To enhance the signal, the bias voltage can be increased leading to an acceleration of the electrons.

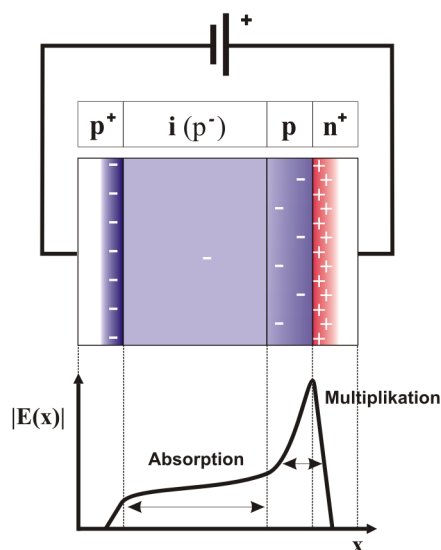


Figure 1.13: Schematic of an avalanche photodiode [10]. Photons would enter from the left.

With sufficient energy these electrons are then again able to produce more electron-hole pairs creating a growing number of electrons; an avalanche. These devices are then called **Avalanche Photodiodes (APD)**. A typical configuration of an APD can be seen in figure 1.13 with the bulk of the material forming a drift region in which initial electrons are created and drift to the p-n junction where they produce the avalanche. The produced avalanche current is proportional to the initial amount of electron-hole pairs and therefore the amount of incident photons. It is possible to raise the bias voltage above the breakdown point at which a current can flow through the depletion zone once an avalanche was initiated. The breakdown then however needs to be halted externally. This puts the APD in Geiger mode. In this mode the gain is increased even further which allows single photons to be measured. This comes at a loss of information as the avalanches become uniform and lose their dependency on the initial photon count.

The gain of APDs is highly dependent on the applied voltage and temperature, increasing exponentially with higher voltage and decreasing with higher temperatures. Additionally the noise of these semiconductor devices increases with temperature which makes cooling important in some cases.

1.5 Radiation Damage in Scintillators

Being in an environment subject to high doses of ionizing radiation is harsh on all materials. Aging effects reduce the quality of the active material or readout. In scintillators these damages lead to a loss of light yield due to degrading transparency or an increased phosphorescence (after glow) increasing the readout noise. The reduction of the measurable light output is not due to a change in the scintillation process but an increase in the attenuation of the light caused by color center formation inside the crystal structure primarily due to defects in the crystal

matrix [11].

So called color centers are vacancies in the crystal structure populated with electrons. The electrons form discrete energy states in the vacancies. These states are excitable creating absorption bands for specific wavelengths inside the crystal. Photons of this wavelength that would pass through undamaged crystal now can be absorbed with a higher probability, reducing the transmission for this wavelength.

The sensitivity of a scintillator crystal to radiation damage is highly dependent on the crystal production. The color centers which may be electrons populating anion vacancies (F center) or holes filling cation vacancies (H center) can be reduced by minimizing crystal defects while growing.

In order to quantify the radiation induced damage to the optical transmission the *absorption coefficient*

$$dk = \frac{1}{d} \ln \left(\frac{T_{before}}{T_{after}} \right), \quad (1.5.1)$$

with T as the transmission before, respectively after irradiation and d as the crystal thickness, can be defined.

1.5.1 Radiation Dependency of the Damage

The damage to crystals depends on the type of radiation. Electrons and gamma quanta excite electrons in the material that populate single color centers but do not displace atoms in the crystal lattice due to their low mass. They can only transmit a small portion of their kinetic energy onto nuclei in a collision limiting the damage that can be done. The population of these color centers is also completely reversible. This also means that the measured damage is expected to saturate with higher doses as all centers become populated.

Heavier particles such as protons or other hadrons are able to transfer more energy and as a consequence induce a different kind of damage. This can be seen in the transmission spectrum, in this example of PbWO_4 in figure 1.14. γ -radiation induces a clear loss of transmission over the total range of measurement. For proton radiation however the absorption edge shifts towards longer wavelengths and is not easily reversible.

Under closer inspection it was seen that proton damage does not saturate for the studied doses, as seen in figure 1.15. This suggests new defects in the crystal matrix are being created.

A study of a PbWO_4 crystal, irradiated by 24 GeV protons, with a high resolution Ge-detector showed several radioactive isotopes in the material, 4 months after irradiation [13]. These isotopes, seen in figure 1.16 are not part of a naturally occurring decay chain but products of nuclear reactions. They were created inside the crystal by proton induced reactions with the matrix material causing fission and spallation, with spallation being the dominant interaction of protons at these energies.

Spallation creates light fragments and heavy nuclei with high kinetic energies. Due to the high Z -values and charge they are strongly ionizing in short distances. Along their path they cause *Frenkel type defects* (FTD), displacements of nuclei in

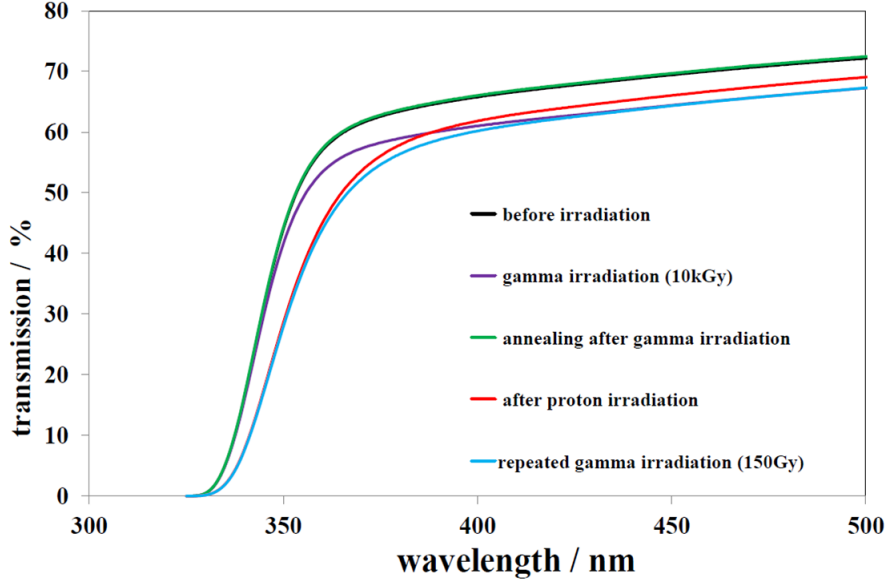


Figure 1.14: Exemplary radiation induced transmission losses due to γ and proton (150 MeV) irradiation of PbWO_4 .

close proximity to the vacancy, inside the crystal. These can be so dense that they form clusters and macro defects.

Evidence that the damage is done by the fragments of fission and spallation rather than by the protons themselves was confirmed in a test with 150 MeV protons. The observed damage patterns in the transmission for 150 MeV protons are the same as for 24 GeV protons at a similar fluence [14].

Lighter materials such as CeF_3 show less hadron specific damage than materials with a high effective Z, as seen in figure 1.15. For this reason efforts are made to develop lighter materials which do not suffer from this kind of degradation due to a significantly lower fission probability.

1.5.2 Damage Recovery

Damage in scintillators worsening the detector response are mostly due to defects or traps in the crystal matrix being populated with electrons creating excitable energy states. Releasing the electrons from these traps, by procuring enough energy, restores the lost transmission. This relaxation is a thermodynamical process that can be accelerated by further stimulation and, if the carriers recombine without being captured, can be described by

$$n_i = n_0 \exp \left(-w_T^i - \sum_j b_j I_j \right) t \quad (1.5.2)$$

with n_i and n_0 as the current and initial color center concentration of type i , $w_T^i = A_i \exp(-E_{TA}/kT)$ as the spontaneous relaxation probability, E_{TA} as the thermo-activation energy of the color center, k the Boltzmann constant, T the temperature, A_i the normalization factor, I_j the specific energy flux, and b_i

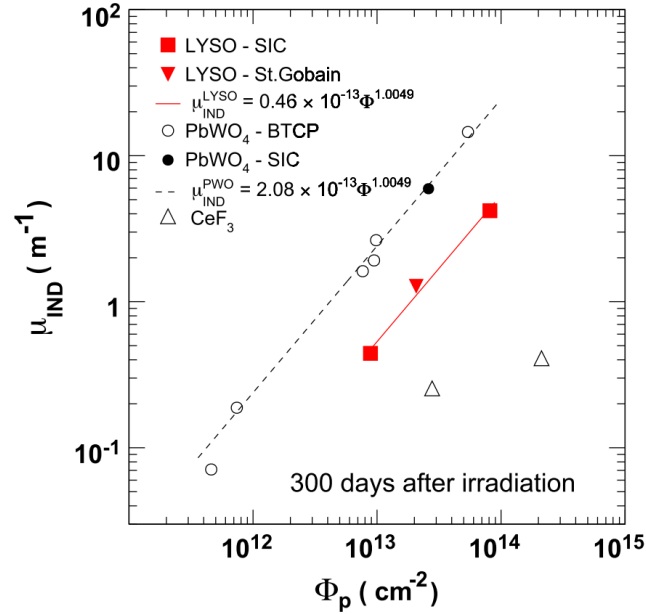


Figure 1.15: Double logarithmic relation between exposed proton fluence and the induced absorption coefficient, previously referred to as dk in equation (1.5.1) [12].

describing the interaction of a color center with a specific flux. It is important to take note that the relaxation speed depends on the temperature exponentially [15]. Since raising the temperature quickens the recovery process damaged crystals are annealed at high temperatures. High thermal energies approaching the melting point also enable FTDs to be closed.

Recovery processes in the crystal at room temperature after and even during irradiation are the reason for a dose rate dependence of the damage. By changing the radiation flux the equilibrium state of populating and depopulating the vacancies is moved, so crystals irradiated with a higher particle flux show a higher transmission loss than crystals that absorbed the same dose over a longer period of time.

For large detector setups thermal annealing is not a practical method to control radiation damage. While annealing may take place at room temperature it is very slow. Higher temperatures require the crystals to be removed from the detector first which is not feasible for complex detector setups. Another solution is *optical bleaching* and/or *stimulated recovery* during offline periods, in which depending on the scintillator UV, visible or infra red light is sent into the crystal. This is also possible during operation if the photo sensor is blind to that spectral range. These injected photons provide the energy needed to free the electrons and holes out of the traps and depopulate them, clearing the crystal from the absorption bands.

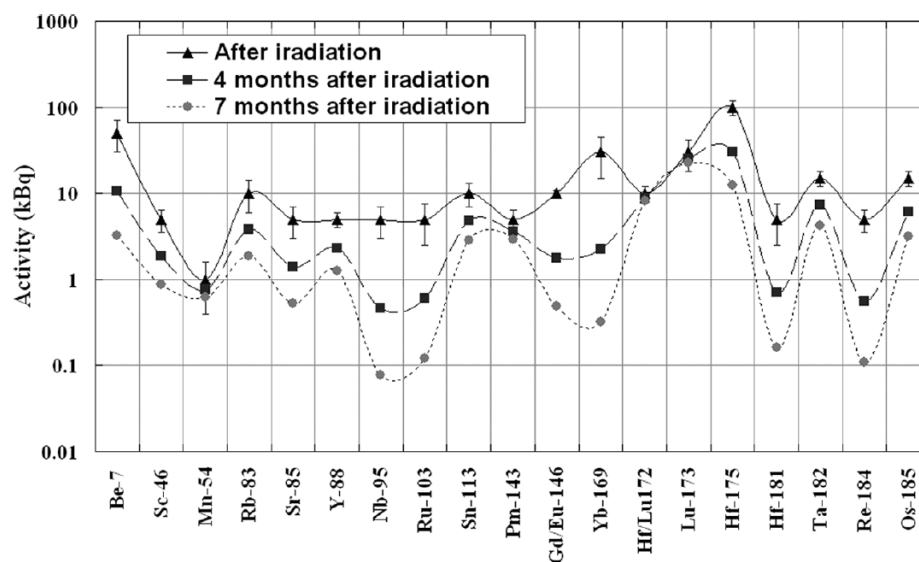


Figure 1.16: *Isotopes and their activity inside the irradiated crystal measured 4 months after exposure to 24 GeV protons, extrapolated to after irradiation and 7 months after irradiation.*

Chapter 2

LuAG and YAG fibers

2.1 Motivation

Over the years many materials have been used in high energy physics detectors, as seen in chapter 1.4.4.1, in medical applications and in homeland security. The availability of new materials have created new possibilities. The high density and consequently short radiation length of lead tungstate made it possible for a very compact homogeneous crystal calorimeter to be built for the CMS experiment for the high energies of the LHC at CERN in Geneva.

This calorimeter however faces longevity problems, as it is exposed to a high fluence of radiation, especially in the forward endcap. Measures to decrease the radiation damages are planned for the upcoming upgrade of CMS together with the upgrade of the LHC to higher luminosity. In order to decrease the effects of the absorbed radiation two things can be done.

- Reducing the length of the crystal penetrated by the radiation by employing a sampling calorimeter design.
- Radiation hard materials like the materials studied in this thesis, can be employed.

The passive material used in between the active layers absorbs a part of the energy depending on the sampling fraction. This reduces the dose deposited in the active material limiting the damage in exchange for a reduction of sensitivity and statistics in the active section.

Possible configurations include either plate based designs or fiber calorimeter. A plate based solution with wavelength shifting fibers running along the edges of the modules is seen in figure 2.1. It is a prototype of a CeF_3 sampling calorimeter built as R&D project of the CMS group.

Although radiation damage is reduced in sampling calorimeters radiation hard active materials are still of need, leading to ongoing investigations of suitable materials.

A fiber setup would consist of fibers placed in an absorber matrix similar to the one seen in figure 2.9. Due to the many scintillating components fiber calorimeter allow a high granularity to be achieved. The distribution of single elements also allows a distribution of different purpose fibers making the readout of different phenomena possible. This is interesting for hadron calorimeter that suffer from

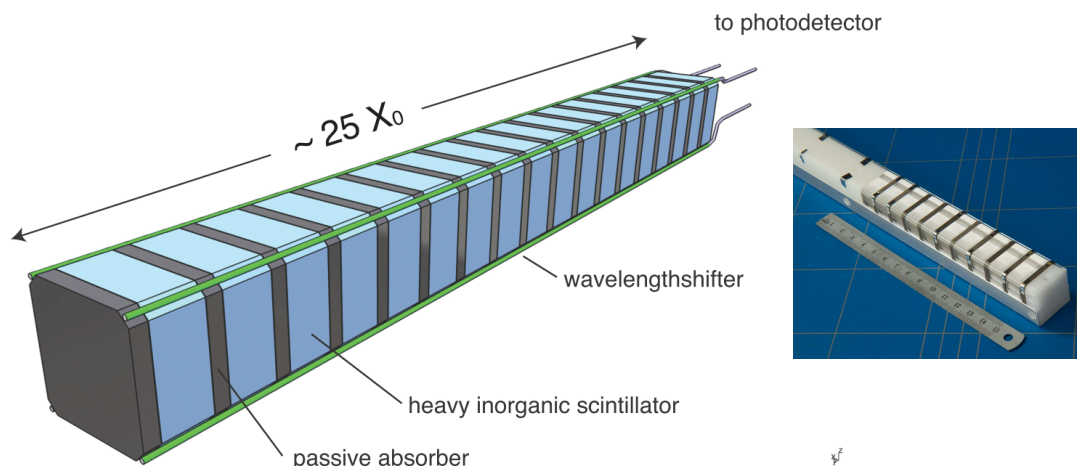


Figure 2.1: Sampling calorimeter module with CeF_3 as active material and tungsten as absorber [16].

the high fluctuations of hadronic to electromagnetic shower fractions from event to event. As mentioned in section 1.4.3.2 it is possible to get an estimation of this fraction by measuring the produced Cherenkov light in comparison to the measured scintillation light. In order to measure this Cherenkov radiation without it drowning in the scintillation light two different fiber types can be used. The majority of the fibers will be scintillating with a few fibers only emitting Cherenkov light. To keep the detector or at least the active part homogeneous, doped and undoped fibers of the same material can be used, where the dopant creates the scintillation in part of the fibers.

A promising material candidate for future calorimeters is LYSO. It is reasonably radiation hard, has a high density (7.4 g/cm^3), short radiation length (1.14 cm), fast decay time (40 ns) and is bright ($165\% \text{ NaI}$) [17]. Initially, when interest arose in lutetium based materials doped with cerium, LYSO was considered best suited for high energy physics applications due to its high density and short radiation length in comparison to other studied materials. LuAG was dismissed at the time due to the lower density (6.7 g/cm^3), longer decay time (60 ns) and significantly lower light yield than LYSO.

However, further studies have shown that the light yield of LuAG could be improved [18]. Light yield itself is not necessarily an intrinsic property but depends also on the quality of the specific crystal. Early crystals might have been of lower quality but by improving the growing techniques it was possible to improve the light yield.

Furthermore LuAG has other advantages that make it a good candidate for a dual readout calorimeter. The fundamental absorption edge at 177 nm allows optical transmission of the ultra violet Cherenkov light as seen in the transmission spectrum 2.2, and the high refractive index of $n = 1.84$ which lowers the Cherenkov threshold, make it an excellent Cherenkov radiator [19]. In addition to that it is mechanically and chemically stable which makes production and handling easier. Benefiting production even further is the by about 90 K lower melting temperature

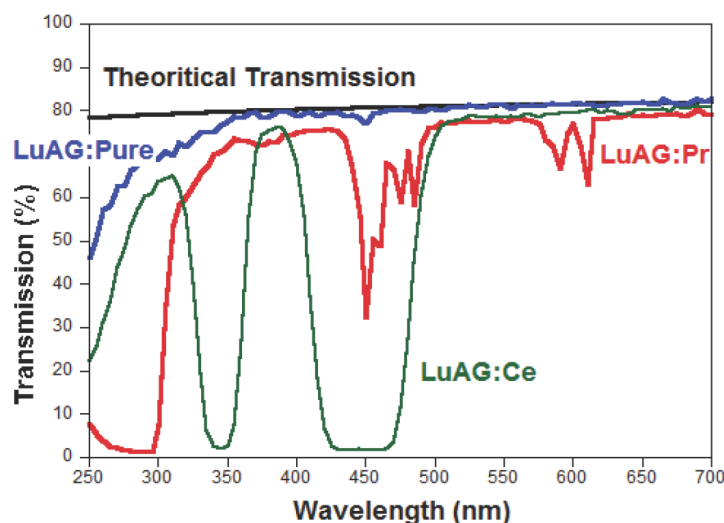


Figure 2.2: Transmission spectra for LuAG with different dopants. Pure LuAG in blue, LuAG doped with cerium in green, and LuAG doped with praseodymium. The black line shows the expected transmission for only Fresnel or reflection losses.

reducing cost and ease of production.

It is possible to produce LuAG fibers by the micro pulling down method (μ PD). This avoids the process of growing the crystals in bulk by traditional methods like the Czochralski or Bridgeman methods, cutting it into long segments and polishing each of those, by growing the crystals directly in fiber form. The applicability of this growth method however may be limited since the homogeneity of the material becomes a higher challenge for small samples.

The μ PD method is capable of creating long fibers with a variable diameter down to below 1 mm in diameter directly from the melt. The material is heated in a crucible with a nozzle at the bottom as seen in figure 2.3. A crystal seed is brought in contact with the first drop of melt and starts moving downward effectively pulling the crystal out of the crucible as it forms at the nozzle. The crystal quality depends on this pulling speed typically between 0.1 and 0.5 mm/min as it determines the temperature gradient at the point of crystallization. An unoptimized temperature gradient may induce structural damages.

Due to extensive experience growing YAG ($Y_3Al_5O_{12}$) fibers for laser applications the step towards growing fibers of the crystallographically similar material LuAG was easy and sample fibers have been studied [19–22]. LYSO fibers in good quality have yet to be produced.

A second set of $1 \times 1 \times 10 \text{ mm}^3$ LuAG and YAG fibers produced by Crytur, cut out of bulk material by wire cutting techniques, are examined too. They are 10 mm long with a 1 mm by 1 mm wide face side. A set of the used fibers is shown in figure 2.4.

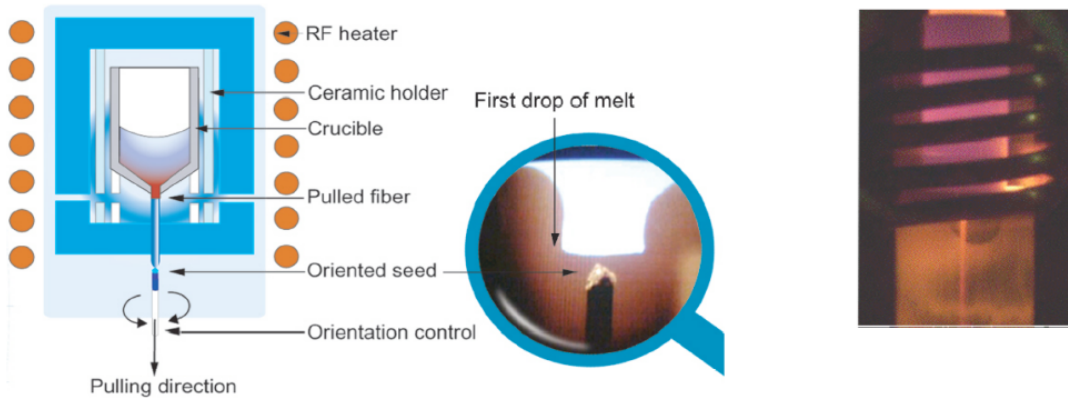


Figure 2.3: The micro pulling down method to grow thin crystal fibers [20]. A crucible is heated by a radio frequency coil. At a nozzle at the bottom of the crucible, melt escapes and forms a crystalline fiber starting from an oriented seed.

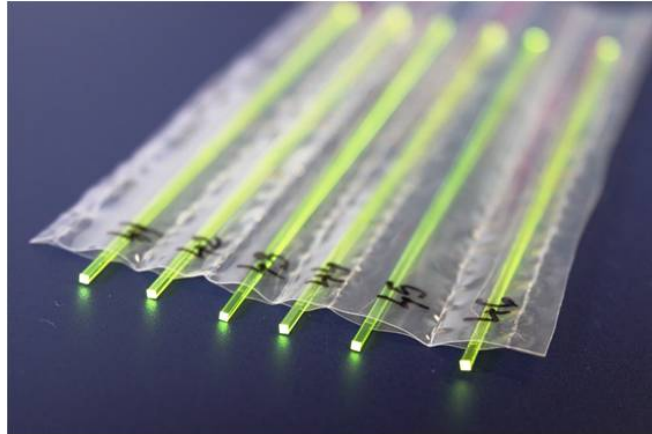


Figure 2.4: A set of $1 \times 1 \times 10 \text{ mm}^3$ LuAG fibers produced by Crytur.

2.2 Attenuation Measurement Setup

To readout the fibers they were positioned and supported by plastic rods and read out by silicon photo-multiplier (SiPM) optically coupled to by high viscosity optical grease. A movable, collimated americium (^{241}Am) source was placed right above the fibers, as seen in figure 2.5, emitting α particles with an energy of 5.64 MeV that lose energy on the way and hit the fiber with a mean energy of 4.06 MeV. Due to the short range of α -particles in the fiber material, scintillation light is produced in a narrow spot within the fiber. This allows for a precise measurement of the attenuation of the light on the way to the sensor.

The LuAG fibers were read out either using a *Hamamatsu* type S12572-050C SiPM with a peak sensitivity photon detection efficiency of 35 % at 450 nm and a pixel size of 50 μm , a 25 μm *Hamamatsu* S12572-025C with a peak sensitivity photon detection efficiency of 25 % at 460 nm or a 15 μm *Hamamatsu* S12572-015C with a peak sensitivity photon detection efficiency of 25 % at 460 nm.

Every pixel of these SiPMs, which are also referred to as MPPC (Multi-Pixel

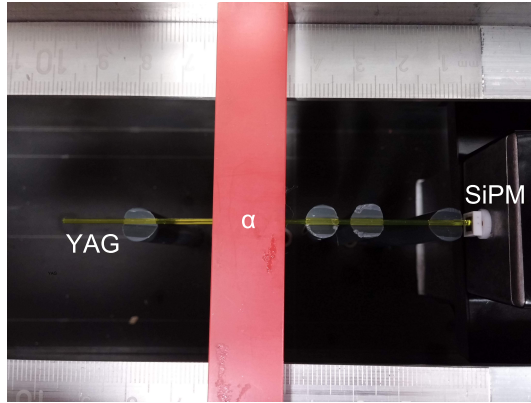


Figure 2.5: Measurement setup for LuAg and YAG fibers read out by an SiPM. Fibers were irradiated by an americium source in a collimator above the fibers.

Photon Counter), acts as an avalanche diode producing a signal of fixed amplitude when hit by at least one photon. Every further photon that hits this pixel at the same time does not get registered. If multiple photons hit separate pixels, the signals of each pixel add up to produce a larger signal proportional to the number of hit pixels and therefore the total light output [23].

A schematic of the electronic setup of the readout is shown in figure 2.6. The signal of the optical fiber readout, in this case an SiPM, is split. One signal branch is digitized by the discriminator if it surpasses a fixed threshold and activates the *input/output (I/O) control*. This threshold is set to suppress single photon signals that would block the readout system since every event takes time to be processed. The default output of the I/O control is high making the AND gate transparent. Once a signal surpasses the threshold the I/O control switches to low preventing further data acquisition. Signals that pass the AND logic produce a gate signal in the *gate generator* that activates the *ADC*¹ as long as the gate voltage is high. The ADC samples the raw readout signal of the other branch and passes a digital value on to the PC where the data is stored. To time the two signals branches to ensure that they overlap delays are used.

2.2.1 Measurement of Irradiated LuAG Fibers

A set of LuAG:Ce fibers of different diameters, lengths and Ce concentration were irradiated at the KVI-Center for Advanced Radiation Technology in Groningen. The fibers were exposed to a 180 MeV proton beam with a fluence of $7.5 \cdot 10^{12}$ protons/cm². Six fibers were irradiated.

After the irradiation the fibers became activated, emitting a dose of 1 μ Sv to 1.5 μ Sv showing about 200 counts/s and therefore had to be locked at Groningen. The fibers were kept cold and in the dark to minimize thermal annealing.

The measured attenuation coefficients for the fibers before (pre) and after (post) irradiation are listed in table 2.1. Before irradiation the fibers were measured using a 25 μ m MPPC, post irradiation a 50 μ m MPPC was used. Due to this difference

¹Analog to Digital Converter

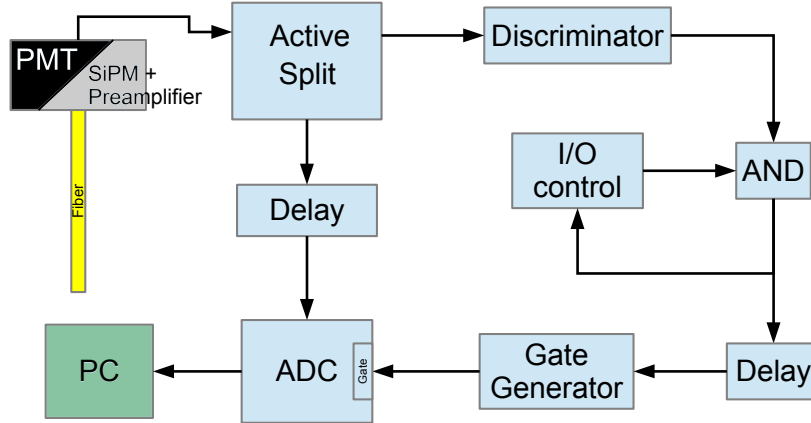


Figure 2.6: Schematic of the readout electronics for the attenuation measurements of single fibers.

the attenuation measurements had to be normalized in order to compare them. These normalized measurements are seen in figure 2.7.

Table 2.1: Irradiated LuAG fibers and their dopant concentration, length and diameter. If not specified the Ce concentration is unknown.

Fiber	Ce [%]	length [cm]	\varnothing [mm]	μ_{pre} [cm^{-1}]	μ_{post} [cm^{-1}]
1438	20	23	2	0.093 ± 0.008	0.195 ± 0.019
1437	40	23	2	0.142 ± 0.009	0.179 ± 0.010
1440	60	23	2	0.150 ± 0.008	0.145 ± 0.004
1425		20	1	0.455 ± 0.099	0.380 ± 0.096
1378.1		10	1	0.413 ± 0.010	0.426 ± 0.019
1378.5		10	1	0.943 ± 0.022	0.877 ± 0.026

2.2.2 Measurement of rectangular YAG and LuAG fibers

The LuAG fibers were read out by the 50 μm MPPC. The obtained position dependent light yield measurements are shown on the left hand side of figure 2.8. A clear exponential attenuation can not be seen. Some fibers even show a rise in light yield towards the far side of the SiPM.

Despite the irregular attenuation all fibers show a sharp falloff of light yield in the first two cm. For the LuAG fibers the attenuation coefficient μ for this region lies between $0.25(3) \text{ cm}^{-1}$ and $0.069(3) \text{ cm}^{-1}$. YAG fibers show an attenuation coefficient between $0.10(2) \text{ cm}^{-1}$ and $0.036(1) \text{ cm}^{-1}$.

Similar results are obtained for the measurements of the YAG fibers read out by the 15 μm MPPC. The results are shown on the right hand side of figure 2.8. Optically the LuAG and YAG fibers do not differ in shape or quality but the YAG fibers exhibit a much higher light yield.

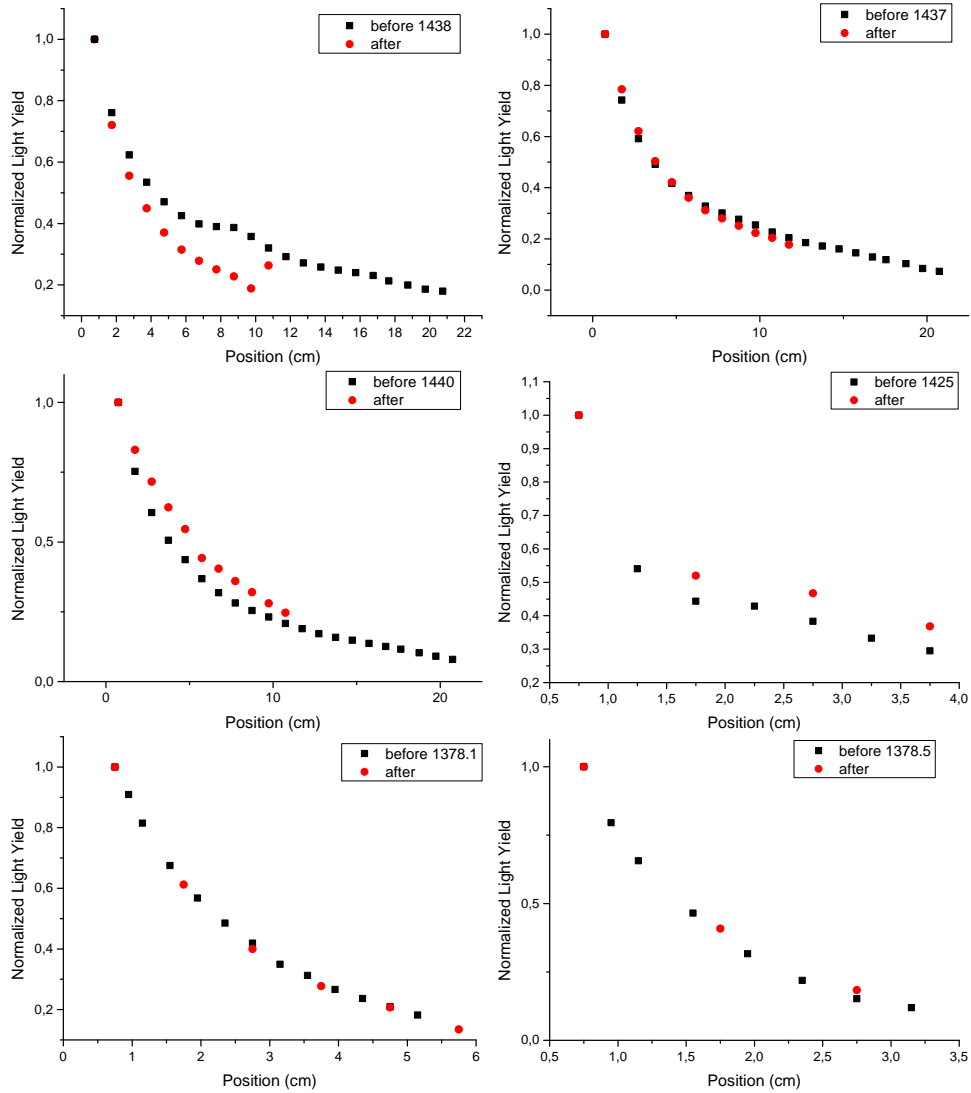


Figure 2.7: Attenuation measurements of the LuAG fibers described in table 2.1 before and after irradiation at KVI with 180 MeV protons. The light yield is given in arbitrary units normalized to the first measurement.

2.3 First Beam Time at MAMI in Mainz

Out of the LuAG and YAG fibers two arrays were built. They consisted of 10 cm fibers in a 6 by 6 configuration loosely assembled in a tungsten matrix with a wall thickness of 1 mm as seen in figure 2.9, producing a module of 13 mm by 13 mm and 100 mm length. All fibers were optically coupled to a plastic light guide, directing the light into a round 19 mm Phillips XP1911 bi-alkali PMT.

The Molière radius of the module can be calculated from the constituents, tungsten ($R_{MW} = 0.93$ cm [24]) and LuAG ($R_{MLuAG} = 2.17$ cm [24]). To obtain the combined Molière radius the mass ratio needs to be factored in. As tungsten and LuAG take up the same volume in the module core it can be calculated from the

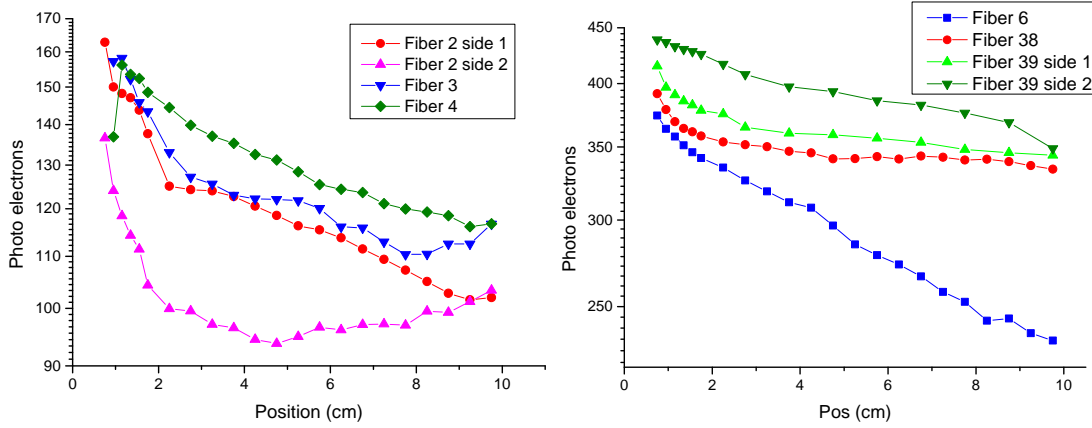


Figure 2.8: Attenuation measurements of *left:* LuAG fibers readout by a $50\ \mu\text{m}$ MMPC, *right:* of YAG fibers readout by a $15\ \mu\text{m}$ MMPC scaled logarithmically. One fiber in each diagram was measured twice; measured in one direction and then turned 180° connecting the other side to the SiPM. Both diagrams are scaled logarithmically.

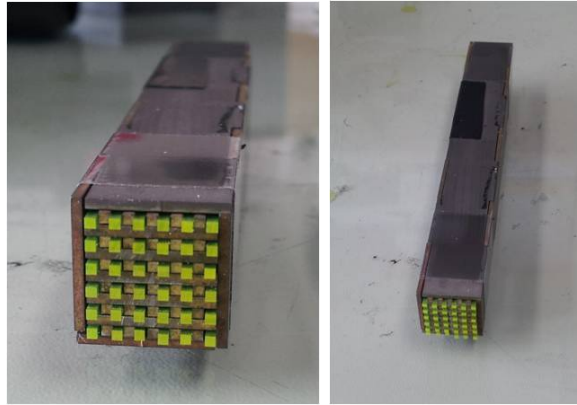


Figure 2.9: A single fiber module with LuAG fibers in a tungsten matrix with a wall thickness of 1 mm

densities as followed.

$$\frac{1}{R_M} = \frac{\rho_W}{(\rho_W + \rho_{LuAG})R_{M_W}} + \frac{\rho_{LuAG}}{(\rho_W + \rho_{LuAG})R_{M_W}} = 0.91\ \text{cm}^{-1} \quad (2.3.1)$$

$$\Rightarrow R_M = 1.09\ \text{cm} \quad (2.3.2)$$

This calculation however does not take the outer tungsten layer into account since it only consist of dead material.

The array was then irradiated by high energy photons in the range of 49 MeV to 744 MeV at the MAMI facility at the Johannes-Gutenberg-University in Mainz.

2.3.1 MAMI Irradiation Facility

MAMI stands for *Mainzer Microtron* which belongs to the *Institut für Kernphysik* of the Johannes-Gutenberg-University in Mainz. The experiment was conducted in the experimental hall A2 that provides a continuous photon beam.

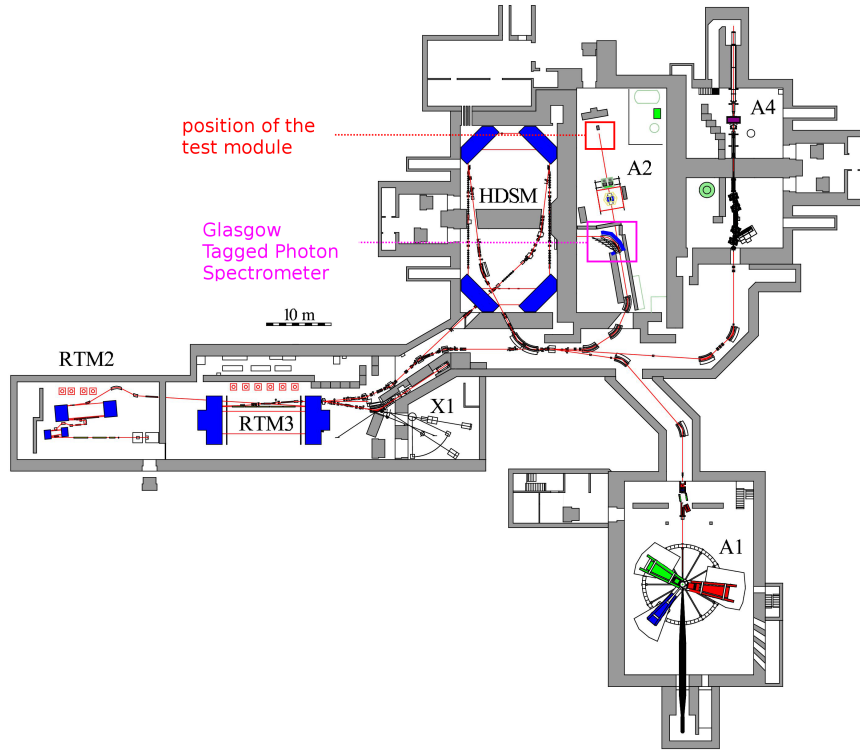


Figure 2.10: The floor plan of the MAMI facility with its four experimental halls A1 to A4 as well as X1 [25]. The LuAG test module was placed on a xy -table in hall A2 at the marked position.

The photons are produced as bremsstrahlung photons of a continuous 855.1 MeV electron beam hitting a thin radiator [25]. The electrons are accelerated in multiple steps. Thermal electrons first gain energy by traversing a linear accelerator and are then accelerated further by three *Race Track Microtrons* (RTM) and finally the *Harmonic Double Sided Microtron* (HDSM), as seen in the floor plan in figure 2.10. After passing the radiator the electrons are then deflected in a homogeneous magnetic field. The bending radius of each electron depends on its energy after passing the radiator. The Glasgow Tagged Photon Spectrometer² makes it possible to associate the electrons with photon energies. The tagger is comprised of a series of overlapping plastic scintillators registering the deflected electrons and their position on the focal plane. Due to the conservation of energy, the energy of the emitted bremsstrahlung photon has to be the difference of the beam energy and the electron energy. This allows the derivation the photon energy from the bending radius of the electron

$$E_{ph}(r) = E_0 - E_{el}(r) \quad \wedge \quad E_{el}(r) = \sqrt{(qBcr)^2 + (m_e c^2)^2}. \quad (2.3.3)$$

with q and m_e as the charge and mass of an electron. Measuring the coincidence of the tagger signals with the relevant detector signals allows the determination of the photon energy. For this beam time 16 tagger energies were used seen in table 2.2.

²from now on only referred to as *tagger*

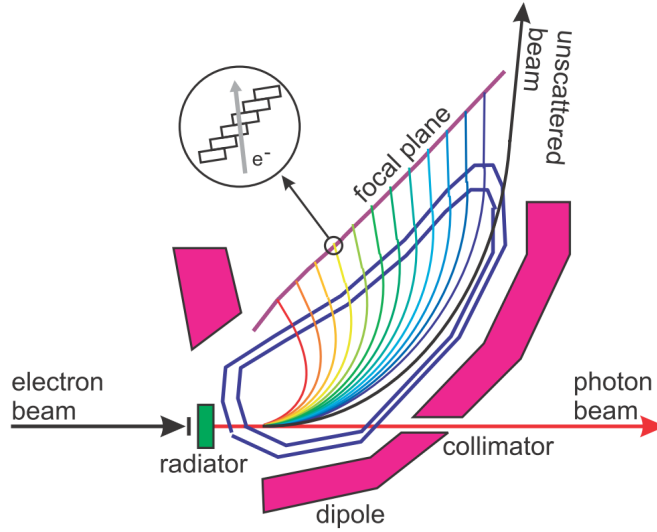


Figure 2.11: Schematic of the Glasgow Tagged Photon Spectrometer [25].

Table 2.2: Energies corresponding to the active tagger channels given in MeV.

tagger #	Energy [MeV]	tagger #	Energy [MeV]
0	56.35 ± 2.74	8	406.30 ± 2.72
1	80.12 ± 2.78	9	438.13 ± 2.65
2	104.08 ± 2.83	10	462.34 ± 2.64
3	128.20 ± 2.80	11	599.91 ± 2.26
4	159.78 ± 2.86	12	641.73 ± 2.12
5	191.58 ± 2.84	13	681.17 ± 2.04
6	238.34 ± 2.78	14	743.92 ± 1.72
7	376.65 ± 2.75	15	766.76 ± 1.69

The photons pass through a lead collimator with a diameter of 1.5 mm, 2.5 m away from the radiator. The LuAG modules were positioned about 13 m from the collimator. Therefore the photon beam has a diameter of up to 9.3 mm projected at the front face of the detector.

2.3.2 Experimental Setup

A schematic of the readout electronics used for the measurements at the MAMI facility is given in [26]. The basic functionality is described in the following. For the coincidence the tagger signal generates a gate of several ns. Inside this time window the coincidence of the tagger signal and a signal corresponding to the OR of all employed LuAG modules, one for the first beam test and four for the second, determines the time at which the data acquisition begins.

The LuAG signals are digitized by a sampling ADC which has an internal threshold that needs to be surpassed to generate a trigger. Due to the variation of the rise time of the detector signal, the trigger signal depends on the amplitude.

Therefore, the time information for each detector signal shows a variation, called *walk*. This effect leads to a smearing of the coincidence time between the detector and the individual tagger channel. A spectrum of timed events of one tagger channel is shown in figure 2.12, with a clear peak distributed between channel 1700 to about 2000.

The exact position of this peak varies from module to module and from tagger channel to tagger channel because of different cable lengths and PMT voltages. For this reason the window defining a true coincidence has to be set for every module and every tagger separately. Events outside of this time frame are random events which form a background to all measurements and are mostly rejected by setting appropriate time cuts, although a partial contribution under the peak remains.

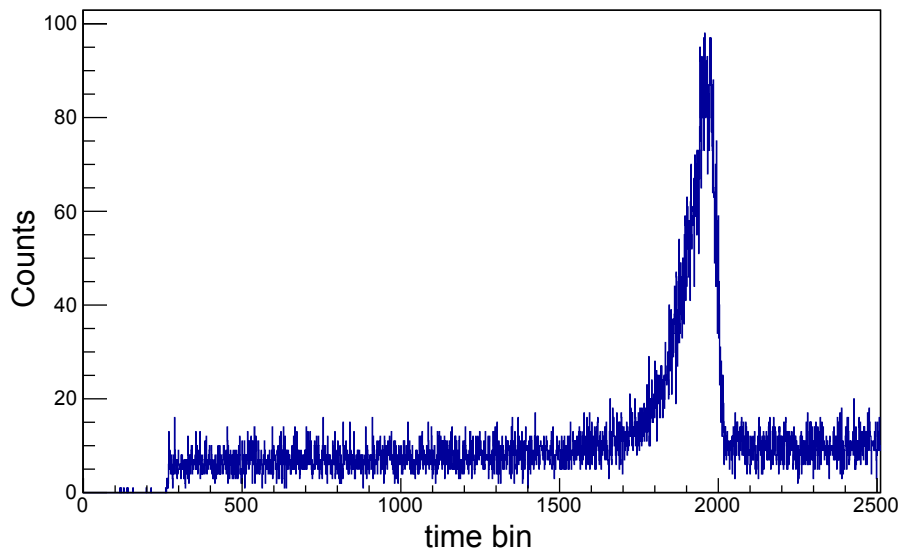


Figure 2.12: A spectrum of the recorded tagger times for all events of tagger channel 0 during the calibration run for module 4.

2.3.3 Data Analysis

The data acquisition stores the pulse shape of each event with its corresponding tagger channel. The data was then reorganized and analyzed offline. The ADC used sampled the signals at 100 Hz making a time bin 10 ns long. The pedestal, the component dependent base value of the ADC, was determined event by event by averaging a section of the pulse shape before the actual pulse. This yields the baseline for the measurements and is determined by the utilized electronic components. In order to extract information from the pulse shape two approaches were applied, to either extract the information from the pulse amplitude or the area under the pulse namely the integral. Both approaches are visualized for a pulse shape of an event in the LuAG module, in figure 2.13.

In order to receive the amplitude, the pulse minimum is subtracted from the pedestal. The integral is calculated similarly, by subtracting every point of the pulse in a set window from the pedestal and adding up the results. This window is

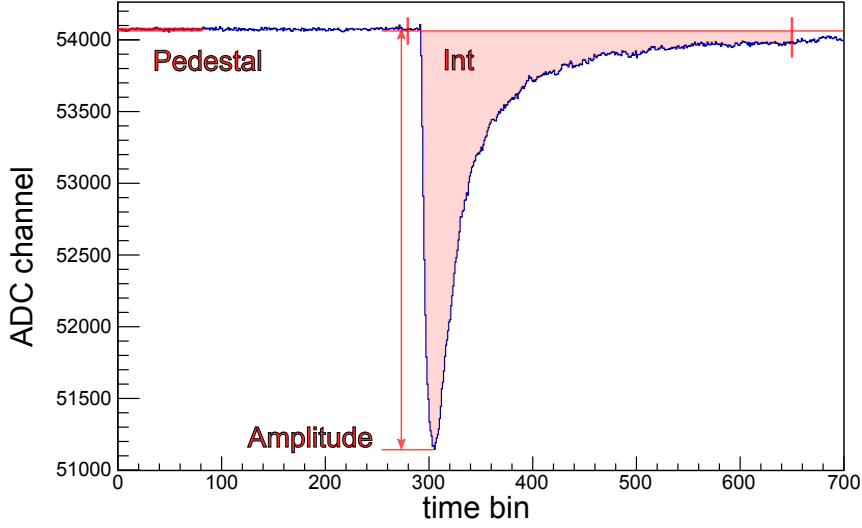


Figure 2.13: Visualization of the feature extraction through amplitude and integral calculation for a single pulse shape.

set after estimating the general start and end of a pulse, before the main analysis starts.

2.3.4 Experimental Results

All events were compiled in histograms separated by the tagger coincidence corresponding to different photon energies of a typical energy width of 2 to 4 MeV. To extract the energy resolution the obtained line shapes were fitted using the Novosibirsk function in order to determine the peak position (energy) and the width σ of the distribution. The Novosibirsk function is defined

$$f(E) = A \cdot e^{-\frac{\ln[1+\chi\Lambda(E-E_0)]^2}{2\Lambda^2}} + \Lambda^2 \quad \text{with} \quad \chi = \frac{\sinh(\Lambda\sqrt{\ln 4})}{\sigma\Lambda\sqrt{\ln 4}} \quad (2.3.4)$$

where Λ parameterizes the tail, σ the width and E_0 the peak energy. The *full width at half maximum* (FWHM) can easily be calculated from the width as $\sigma = \frac{FWHM}{2.35}$, as is the case for Gaussian distributions.

Figure 2.14 shows a fit of the histogram for incident photons with 377 MeV with the Novosibirsk function. A tail to higher energies is observed.

The response of the detector for the LuAG and YAG fibers can be seen in figure 2.15, plotted logarithmically for selected photon energies. The histograms contain a large contribution of random signals which prevent a clear distinction of the signal peaks at low energies. For this reason no distinct peaks were found at 56 MeV and 80 MeV for the feature extraction via the amplitude. The fits for the feature extraction via the integral can also only be seen as position and width estimations because their falloff to lower energies is dominated by random events making the fit very sensitive to fit boundaries. Although clear peaks were visible for the LuAG

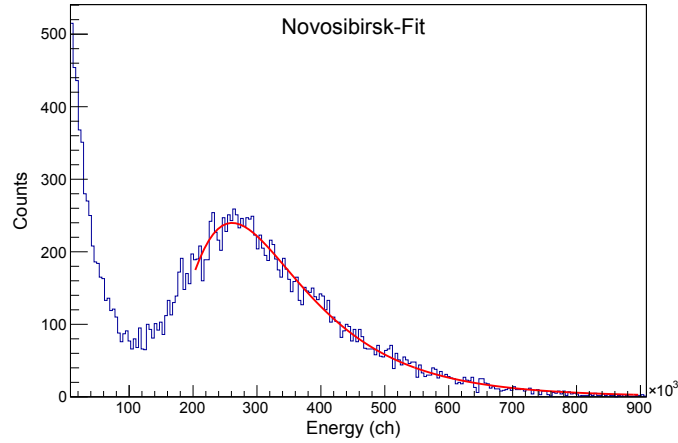


Figure 2.14: Exemplary Novosibirsk fit of a histogram for 377 MeV photons.

fibers the YAG fibers only showed an exponentially declining line shape in their histograms with no clear structure.

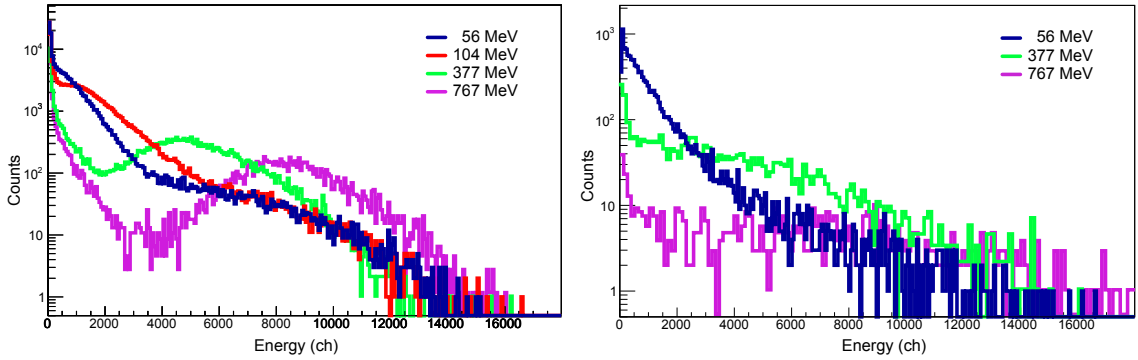


Figure 2.15: Response of the detector plotted logarithmically for the LuAG (left) and YAG fiber (right) module for amplitude feature extraction at three selected energies.

A measure for the quality of the detector is its linearity of deposited energy to peak position shown in figure 2.16 with the photon energy plotted against the respective detector signal.

The LuAG module showed a similar resolution for amplitude and integral approach for the feature extraction with a high relative resolution of almost 200 % falling off rapidly to about 80 %. The asymptotic approach to about 30 % suggests a constant term of the resolution of the order of 20 %. The deduced relative resolution improves with rising energy faster than one would expect from the $\sim \frac{c}{\sqrt{E}}$ dependency; especially at the lower energies. This prevents a fit with the expected equation in (1.3.2) as it produces values with a vanishing constant term.

2.4 Second Beam Time at MAMI

For the second beam time at MAMI in Mainz at the same facility, four of the LuAG fiber modules were combined. Each module was read out individually. The

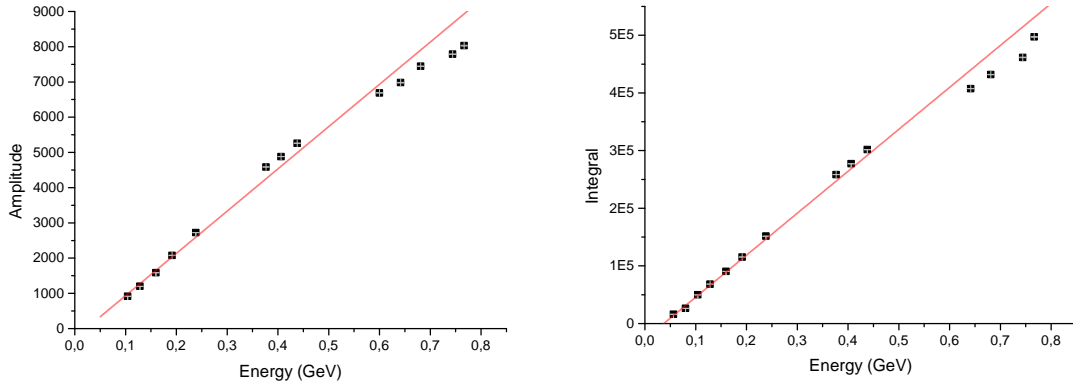


Figure 2.16: *Linearity of the module for feature extraction via the amplitude (left) and the integral (right).*

modules were placed on a XY-table in order to expose each module directly to the beam. Data was taken for five beam positions aiming the beam at the center of each of the modules as well as at the general center in between the modules as seen in figure 2.18.

2.4.1 Extended Data Analysis

The data analysis of the digitized signal shape was improved upon for the second run. Since the gate settings for the integral calculation are somewhat arbitrary two sets, for a longer and shorter integration window from time bin 200 to 1200 and from 450 to 900 respectively, were implemented. A shorter window is more sensitive to timing variances of the pulses but picks up less noise from the background. As seen in figure 2.19, the shorter integration window leads to a slightly better resolution, so for the further analysis the shorter window was chosen.

To analyze the total response of the 2×2 matrix with the beam aimed at position 5, the signals of every single event in each module need to be added. The responses of the PMTs are not equal and, in order to add them up they need to be calibrated according to their signal strength. To adjust the responses, the measurements of the individual modules at beam positions, 1 to 4 are used to normalize the responses to the first module. The peak positions of each module were normalized to module 1 energy by energy. Some normalized responses for 56 MeV, 377 MeV and 767 MeV are seen in figure 2.20 with the normalizing factors for each tagger energy shown in figure 2.21.

To calculate the sum of the four modules the signal pulses of each module were analyzed separately and then added up scaled by their respective factor to obtain the total signal. Especially at low energies where the shower does not spread very far laterally, energy is not deposited in every module.

Adding up all modules nonetheless would introduce unnecessary noise to the sum. To get an idea of this background two histograms for events with a tagger signal in a time window between time bin 1500 and 1700 are plotted in figure 2.22 as an amplitude spectrum on the left and an integral spectrum on the right. In order for a channel to be added to the total signal it has to surpass a noise

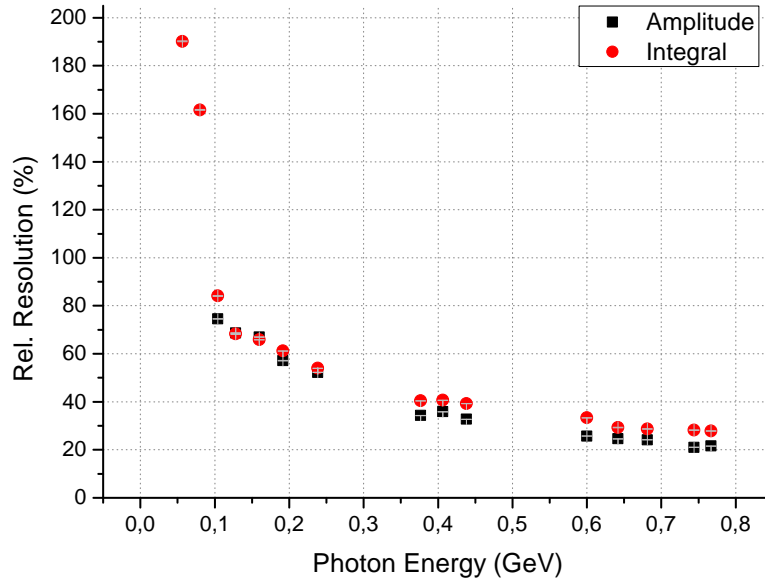


Figure 2.17: Resolution of the LuAG module for amplitude and integral feature extraction. For the first two tagger channels a peak was not distinguishable from the background noise.

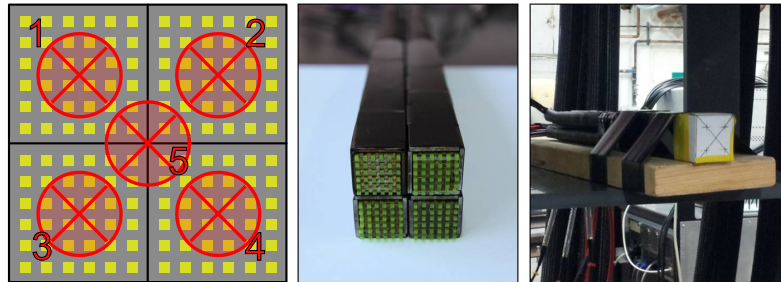


Figure 2.18: Four 6×6 LuAG fiber modules combined. Data was taken with the beam aimed at the five marked positions.

threshold. This threshold was set at 50 for the amplitude and 3000 for the integral.

The multiplicity of responding modules for each event as seen in figure 2.23 increases with energy. For 56 MeV the majority of the energy is deposited in one module with about 70.6% of events registering in only one module and 26.5% in two. For 767 MeV photons 52.2% of events deposit energy in all four modules with only 4.5% showering in a single module.

Another feature that was implemented to improve the energy resolution is the *pileup rejection*. Two photons interacting with the detector at almost the same time can cause an overlap of the signal pulses leading to distorted features. Such pulses are seen in figure 2.24. Due to the fact that only 16 out of 350 tagger channels were chosen to be read out it is not sufficient to reject events based on the overlap of two tagger signals. Since the photons are produced randomly via bremsstrahlung they have a continuous energy spectrum up to 800 MeV and many photons do not fall into the energy range of the selected tagger channels.

In order to reject these events the ratio of integral to amplitude can be employed.

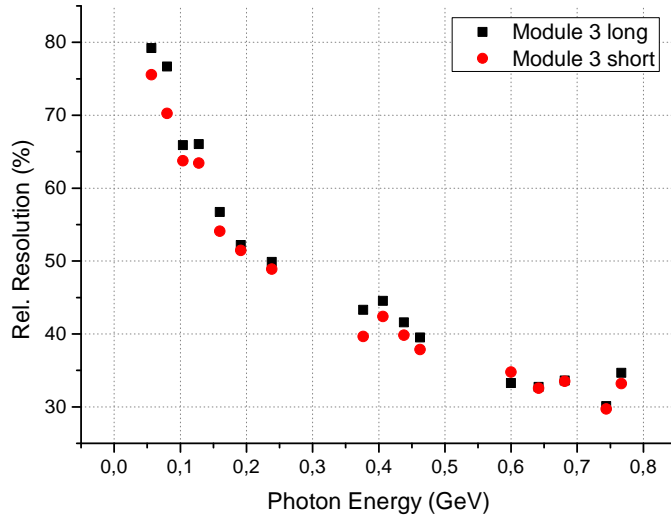


Figure 2.19: Comparison of the resolution for a longer and shorter window of integration (200-1200, 450-900 time bins) in module 3.

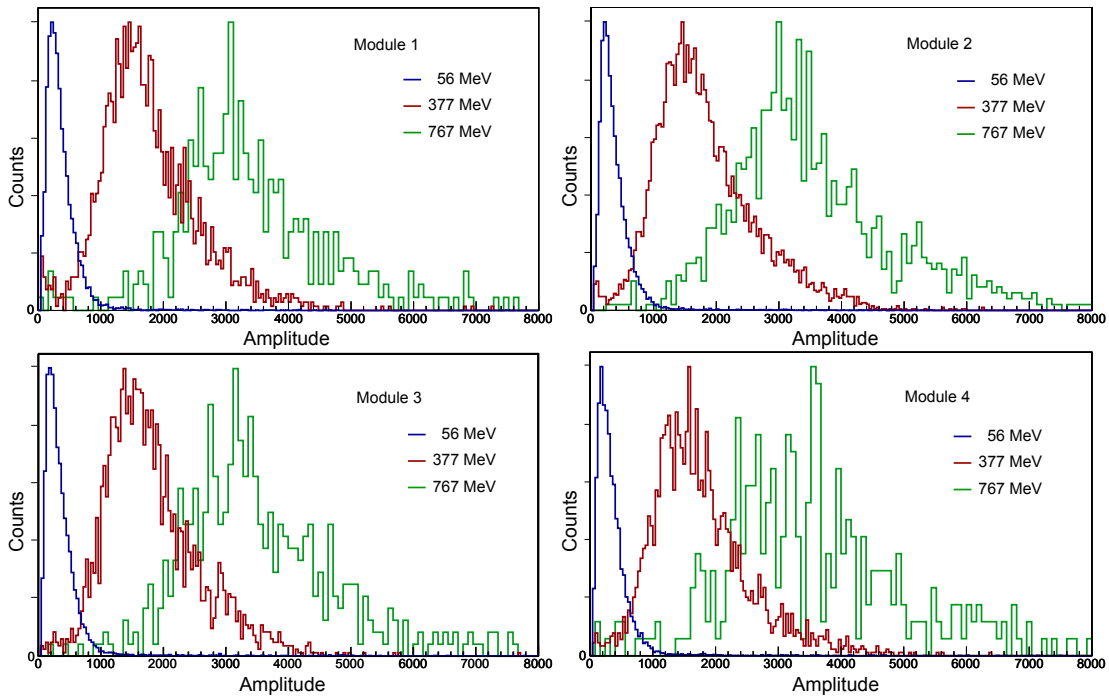


Figure 2.20: Calibrated responses of single modules for the calibration measurements 1 to 4 plotted as normalized counts against energy given in ADC channels at three selected energies: 56.35 MeV, 376.65 MeV and 766.76 MeV.

For single events this ratio usually is constant except for a slight drop off at low energies [27]. Signals with overlapping pulses show a larger area under the line shape with little to no shift in amplitude.

To find the *cutoff factor* the ratio was plotted for all measured events and can be seen in figure 2.25. Plotting the I/A ratio versus the amplitude shows that the majority of the events have a ratio of around 80. The cut was set at a ratio of 100

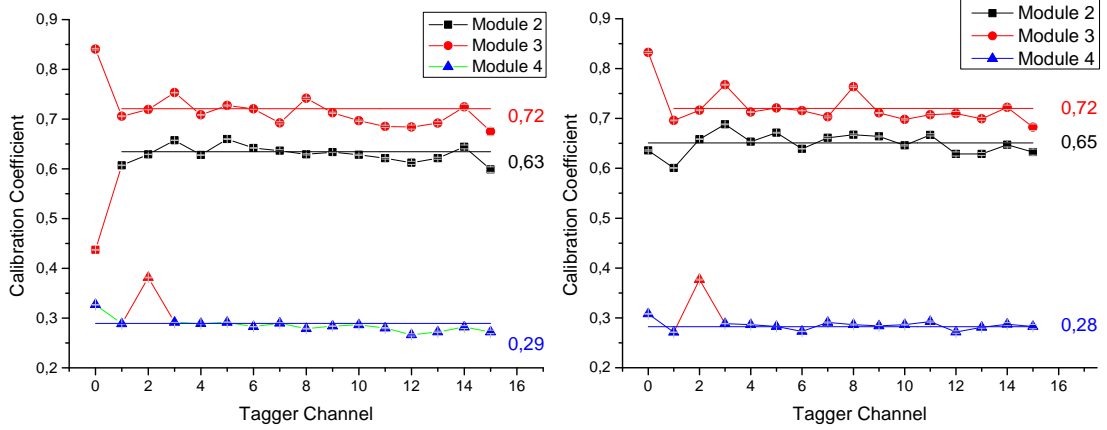


Figure 2.21: *Detector responses of each module normalized to module 1. Coefficients determined for the amplitudes on the left and coefficients for the integrals on the right.*

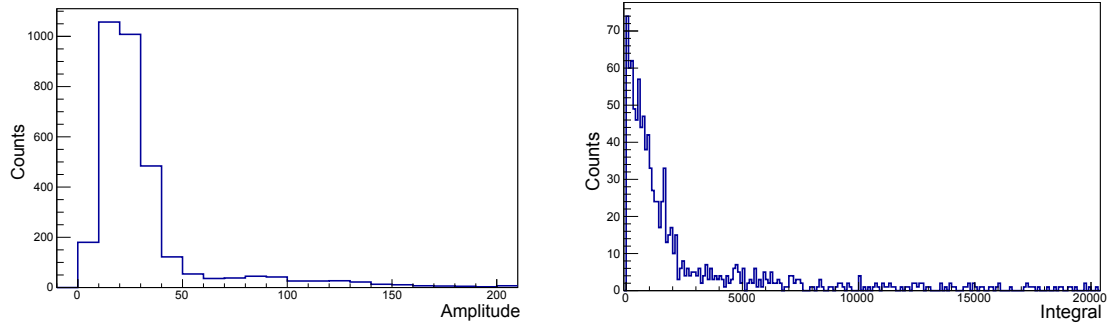


Figure 2.22: *Noise distributions for a tagger time window outside of the signal window for (left:) the feature extraction via the amplitude and (right:) via integral.*

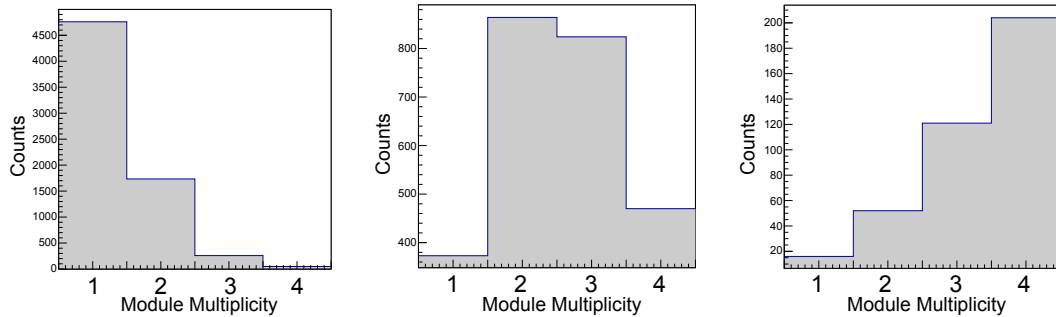


Figure 2.23: *Multiplicity of modules with a signal above the amplitude threshold for three selected energies (56 MeV, 377 MeV, 767 MeV).*

to include signals with slight variations but reject events with a clear pileup.

For the multi-module analysis events were rejected if one of the modules showed an I/A ratio above the cutoff factor.

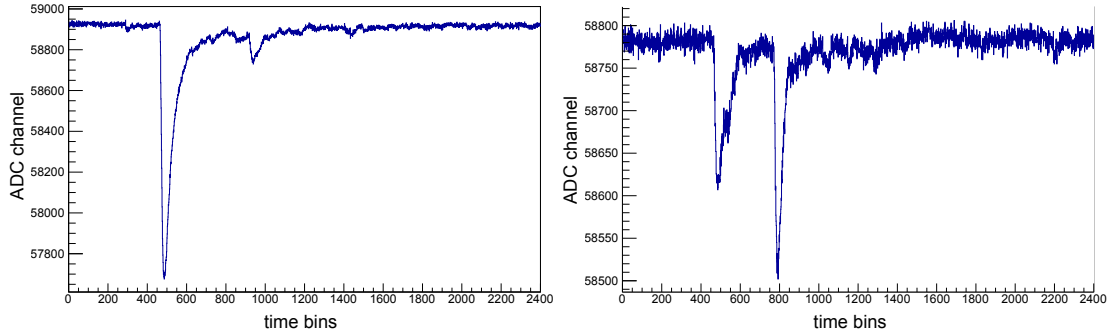


Figure 2.24: Pulse shapes of two irregular events with a tagger multiplicity of 1.

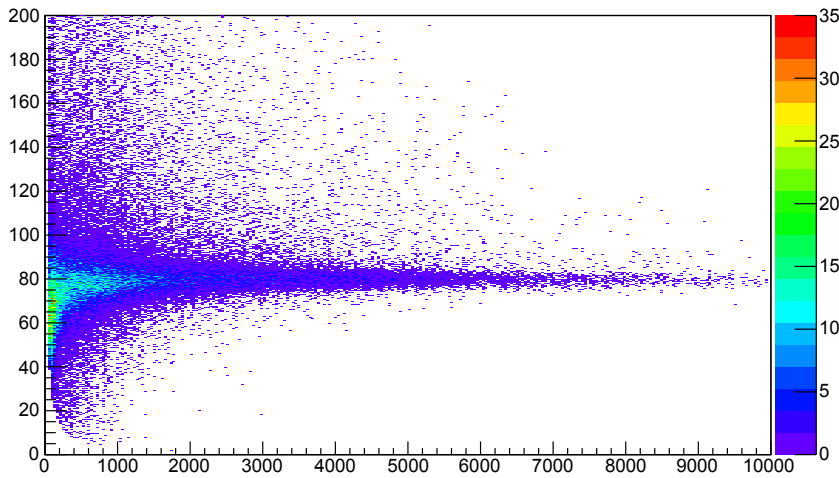


Figure 2.25: The relation of pulse integral to amplitude vs the amplitude for all recorded events in the set time window with amplitude and integral above the threshold.

2.4.2 Experimental Results

The individual modules, when irradiated directly, showed reasonably good linearity for feature extraction via the integral and amplitude. The resolution for both approaches are again very similar. The line shapes exhibit a heavily reduced noise background when comparing figure 2.15 and figure 2.20. The amplitude distribution features a slightly better resolution than the integral distribution.

The distributions produced for the central irradiation at beam position 5 are shown in figure 2.26 for every module individually and figure 2.27 for the weighted sum of the responses.

Comparing the responses of the calibration and sum measurements, a decrease of energy deposited in the LuAG fibers is visible. The sum of the amplitudes of all four modules was on average $(77 \pm 4)\%$ smaller at beam position 5 than for measurements done in module 1 at beam position 1 with a relatively constant ratio. The integral was more energy dependent with a largely reduced response of 50 % at 56 MeV growing to a ratio of up to above 90 % as seen in figure 2.28.

This also reflects in the resolution as can be seen in figure 2.29 where the sum shows a worse resolution than for single module measurements. A fit of the resolution with the expression (1.3.2) gives a statistical term of $c_1 = (19.83 \pm 0.49)\%$

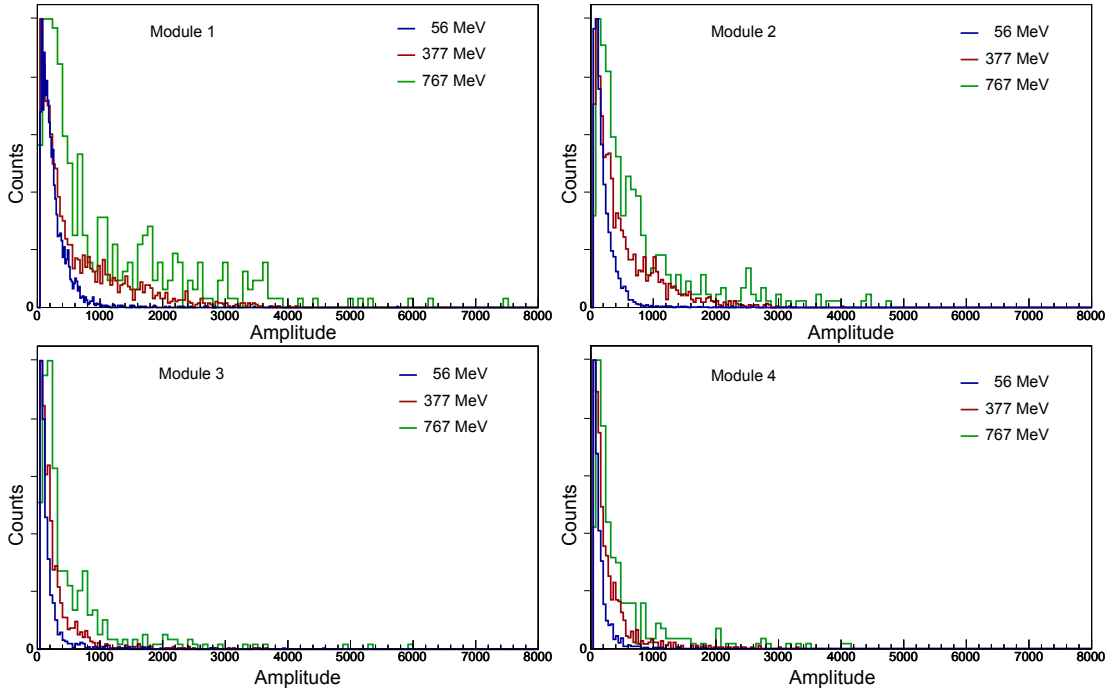


Figure 2.26: Amplitude distributions of single modules for irradiation at position 5 plotted as normalized counts against energy given in ADC channels for three selected energies.

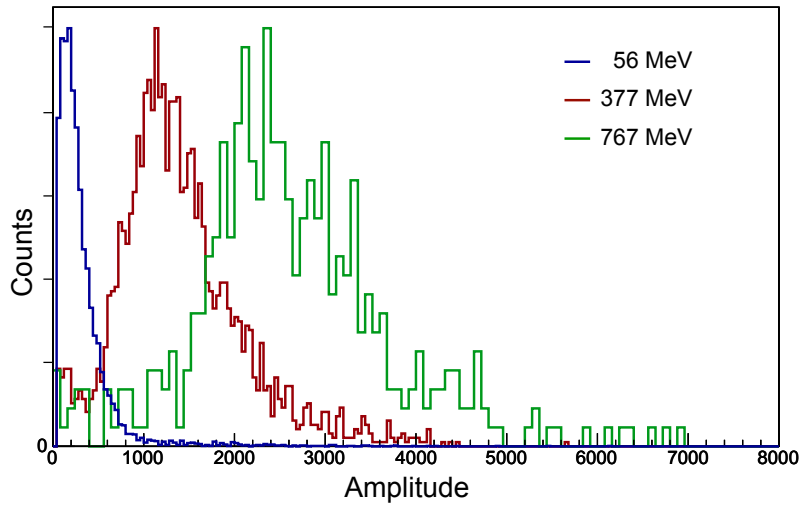


Figure 2.27: Signal distribution after summation of the amplitudes of all four calibrated modules for three selected energies.

and a constant term of $c_2 = (25.2 \pm 1.7) \%$.

Employing the feature extraction via the integral shows a worse energy resolution. Results for the resolution and linearity are plotted in figure 2.30. The resolution of the energy for the integral approach shows a significant worsening at low energies when multiple modules are summed up. In general, when comparing the amplitude and integral approach as seen in figure 2.31, the feature extraction via amplitude shows a better resolution especially at lower energies.

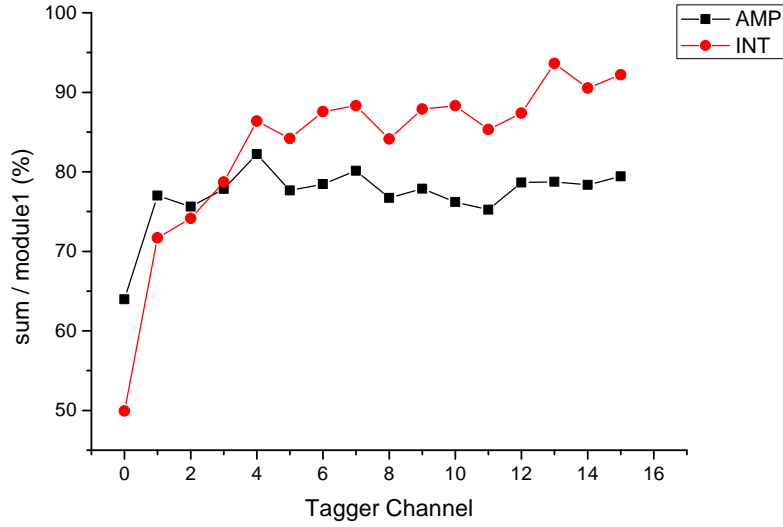


Figure 2.28: Peak position of the sum relative to the calibration measurement of module 1.

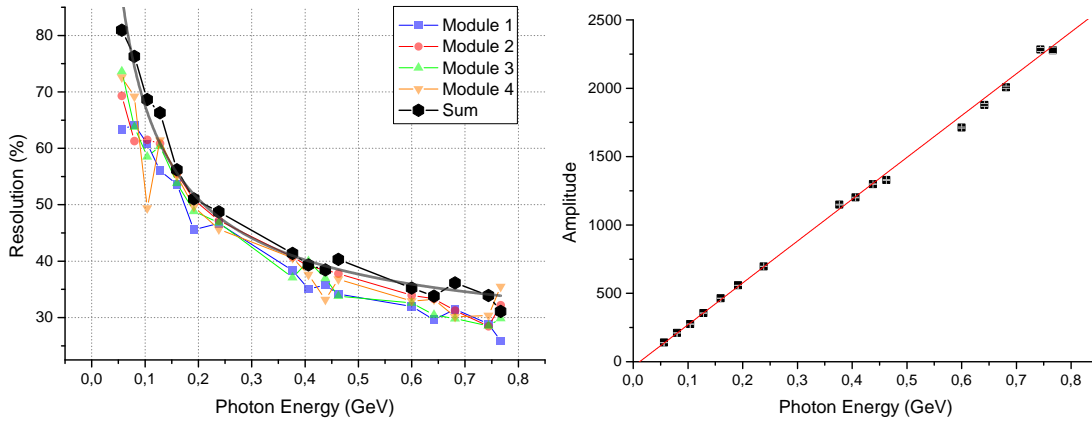


Figure 2.29: left: Comparison of the resolution for all four calibration measurements and the sum of the four modules at beam position 5 for feature extraction via the amplitude. The grey curve was fitted to the resolution of the sum, with a statistical term of $c_1 = (19.83 \pm 0.49)\%$ and a constant term of $c_2 = (25.2 \pm 1.7)\%$. **right:** Linearity of the summed measurements at beam position 5.

The implementation of the pileup rejection leads to an insignificant improvement of the resolution for the feature extraction via the amplitude. This is observed for single modules as well as for the sum as seen in figure 2.32. Distributions of the feature extraction via the integral benefit slightly from the pileup correction, especially in the sum of multiple modules at low energies as can be seen in figure 2.33.

Between 40% and 5% of events are rejected depending on the measurement and the tagger channel. For single module integral measurements 17.5% fewer events are seen in the lowest energy tagger channel whereas it is only 5.5% for the highest energy tagger channel. Higher rejection rates are observed for the measurements of the sum of the four modules. In that case a drop from 38.8% to 17.6% is seen.

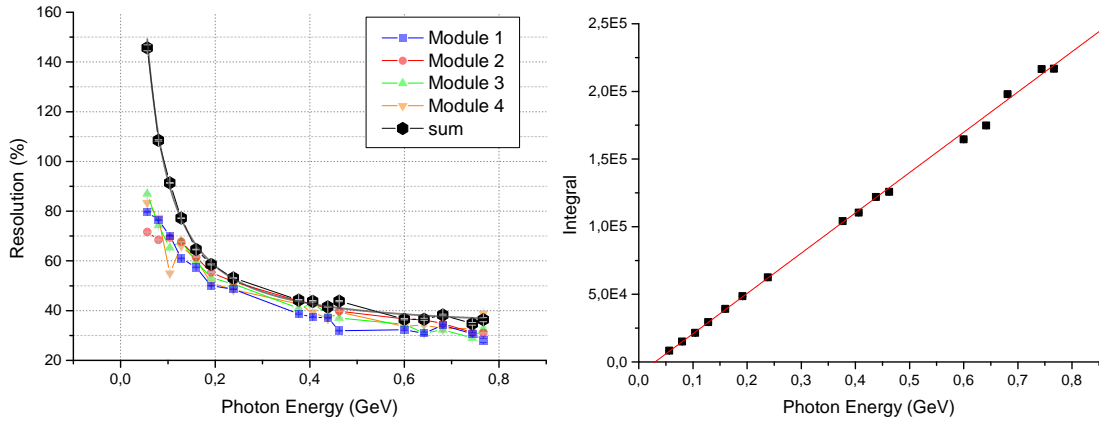


Figure 2.30: *left:* Comparison of the resolution for all four calibration measurements and the sum of the four modules at beam position 5 for feature extraction via the integral. The grey curve was fitted to the resolution of the sum, with a statistical term of $c_1 = (13.34 \pm 2.20)\%$ and a constant term of $c_2 = (32.12 \pm 2.00)\%$. In addition to that a term with a linear energy dependence of $(7.58 \pm 0.35)\%/E$ parameterizing noise at low energies is added in quadrature. *right:* Linearity of the summed measurements at beam position 5.

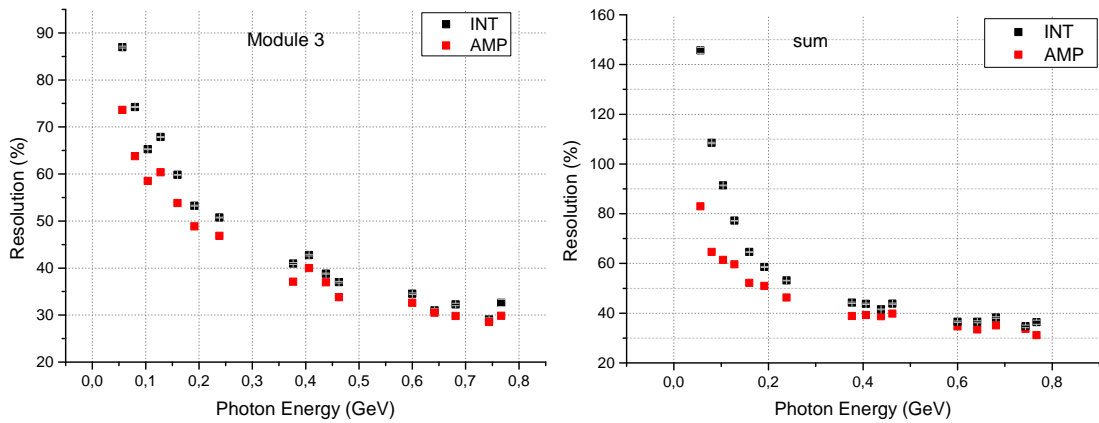


Figure 2.31: A comparison of the obtained resolution for feature extraction via amplitude and integral for a single module (on the left) and the sum of four modules (on the right).

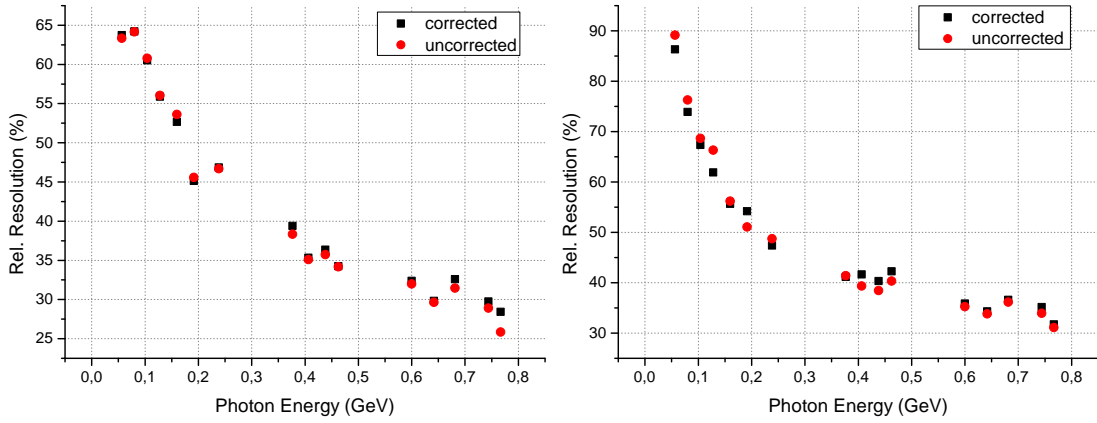


Figure 2.32: Comparison of the pileup corrected and uncorrected relative resolutions for feature extraction via the amplitude.

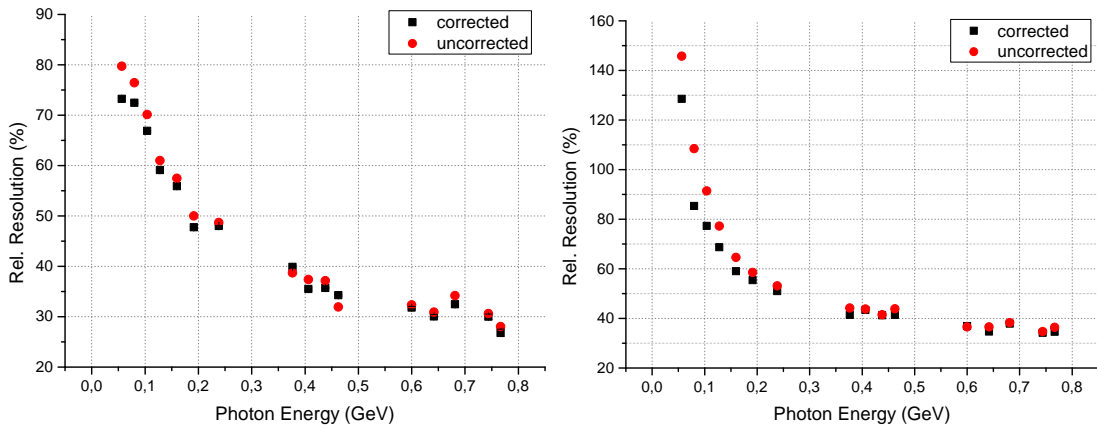


Figure 2.33: Comparison of the pileup corrected and uncorrected relative resolutions for feature extraction via the integral.

Chapter 3

Study of the optical properties of DSB

3.1 Motivation

LYSO as well as LuAG, which was discussed previously, contain lutetium with an atomic number of $Z = 71$. With this atomic number it is right at the experimentally found effective threshold for fission. Elements with a $Z > 71$ are expected to show hadron specific radiation damage created by fission inside the material [12]. Studies performed on LYSO crystals show cumulative radiation damage, increasing with absorbed dose [12], as seen in figure 1.15.

A scintillator material that has gained interest is DSB:Ce, a colorless cerium doped glass ceramic made out of $\text{BaO}_2^*2\text{SiO}_2$. It can be produced with standard glass production technology with subsequent annealing at relatively low temperatures ($<1000^\circ\text{C}$) which makes mass production at low cost possible. Due to their amorphous structure that allows defects which facilitate color center formation, glasses usually show low radiation hardness. Unless they are annealed to produce the crystalline nano structure [28].

The material can be produced in bulk or fiber form. DSB has an effective Z of 51, a density of 3.8 g/cm^3 and a radiation length X_0 of 3.3 cm [28]. Due to its stopping power being lower than most heavy inorganic scintillators and its long radiation length it will have to be used in a sampling setup with an additional absorber to achieve a compact form factor.

3.2 DSB:Ce Fibers

One hundred 20 cm long fibers with a diameter of about 1 mm and different coloration as seen in figure 3.1 were produced in Belarus and provided by the Institute for Nuclear Problems (INP) at the Belarus State University (BSU) in Minsk. The diameter varies from fiber to fiber and from one end to the other. When illuminated cracks inside the material become visible. Two distinct colors can be seen. Some fibers have a more blueish tint while others are more yellow. The difference between them is further investigated in the following section.

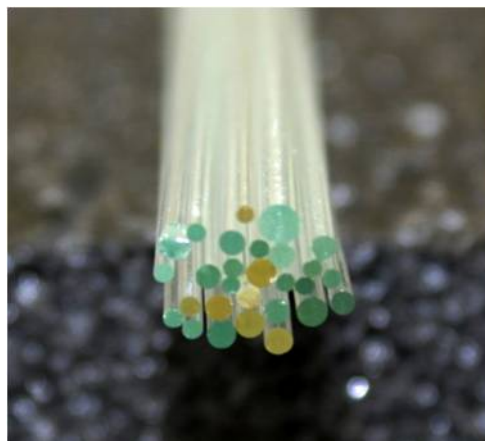


Figure 3.1: A bundle of DSB:Ce fibers from the INP in Belarus.

3.2.1 Attenuation Measurements

A first attempt to measure the fiber attenuation was made using a new setup, similar to the one used in section 2.2, replacing the SiPM by a PMT for a lower noise level.

Using the new setup the signal however could not be distinguished from the γ -background the ^{241}Am source produced in the PMT directly. A second batch of fibers with a diameter of about 2 mm showed the same result.

The optical transmission of a small $13 \times 15 \times 5 \text{ mm}^3$ sample of DSB was measured, seen in figure 3.2 with an air reference measurement, meaning Fresnel losses are still included in the shown spectra¹. In order to confirm the luminescence process in the fiber samples the emission after excitation by a laser was investigated. Three fibers, two fibers of 1 mm diameter with a yellow and blue tint as well as a thicker fiber, have been selected. The emission spectra were measured with a *Spex 1982 0.22 m* optical spectrometer, with a resolution of 0.25 nm at a slit width of 0.1 mm.

The fibers were wrapped to ensure that only light traveling through the fibers reach the spectrometer. Three cutouts were placed along the fiber wrapping to irradiate the fibers and excite them as seen in figure 3.3. To excite the fibers UV-light of different wavelengths was used. The first measurements were done with a 266 nm Nd:YAG laser, then a 325 nm HeCd laser and finally a 365 nm LED.

The spectra show no significant difference for the different excitation wavelengths. A set of spectra excited with the 325 nm laser are shown in figure 3.4. The intensities are given in normalized, arbitrary units since the measurement was very susceptible to small position changes of the fiber. Two peaks at about 425 nm and 470 nm, respectively, are seen. Their relative intensity depends on the position of the excitation. The intensity of the 425 nm component decreases in comparison to the 470 nm component as the excitation spot is moved further away from the spectrometer and the scintillation light travels further through the material.

A slight difference between the blue and yellow colored fibers is visible too.

¹This is the case for all following transmission measurements.

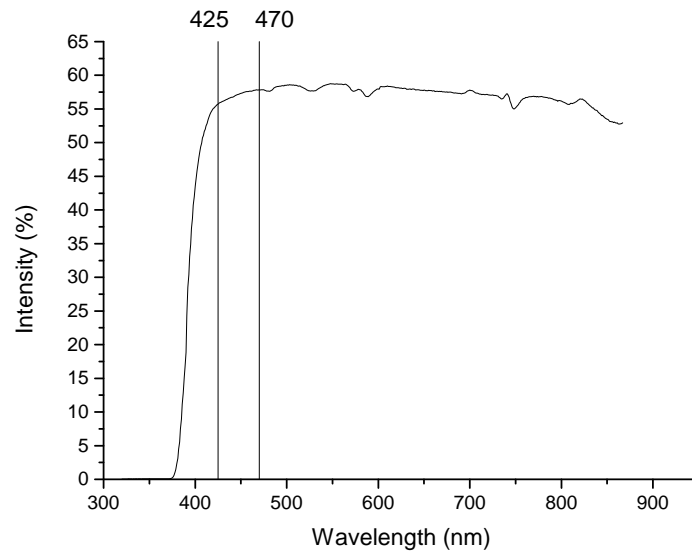


Figure 3.2: Transmission of a $13 \times 15 \times 5 \text{ mm}^3$ piece of DSB, with the wavelengths of the emission peaks marked at 425 nm and 470 nm.



Figure 3.3: Schematic setup of the spectrum measurements of the DSB fibers.

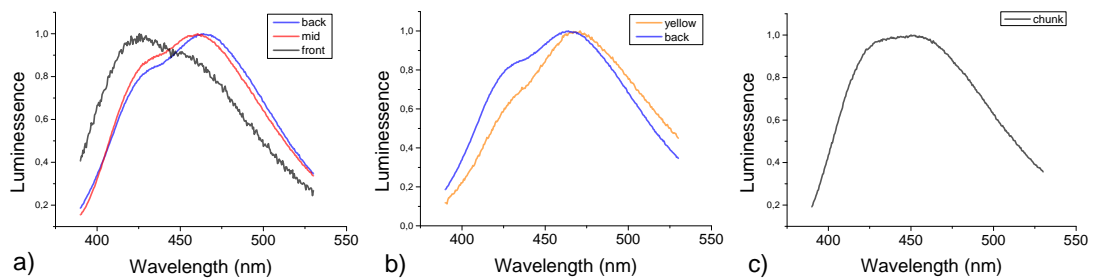


Figure 3.4: A set of different luminescence spectra. The intensities are given in arbitrary units. **a)** Emission spectra of a fiber irradiated with a 325 nm laser at different positions along the fiber as seen in figure 3.3. **b)** Emission spectra for a blue and a yellow tinted fiber at the same position. **c)** spectrum of a small ($13 \times 15 \times 5 \text{ mm}^3$) chunk of DSB.

Looking at figure 3.4 b) one can see that the blue fibers show a slightly higher relative intensity for the longer wavelength component.

The larger $13 \times 15 \times 5 \text{ mm}^3$ piece of DSB was measured too. Its emission spectrum is shown in figure 3.4 c). It is an overlay of both previously seen peaks with no significant difference in intensity between two components.

3.2.2 Fiber Scintillation Measurement

In order to improve the sensitivity a coincidence measurement was set up between the PMT measuring the emitting light of the fiber and a plastic scintillator behind the fiber, firing when it is hit by an electron from the source passing the fiber. A β -emitter (^{90}Sr) behind a lead collimator was employed. A strontium source produces electrons of up to 0.546 MeV in the decay of strontium into yttrium and up to 2.282 MeV electrons in its the following decay of yttrium [29]. In addition to that the PMT was shielded with a 5 mm thick lead plate to reduce the noise. A schematic setup can be seen in figure 3.5.

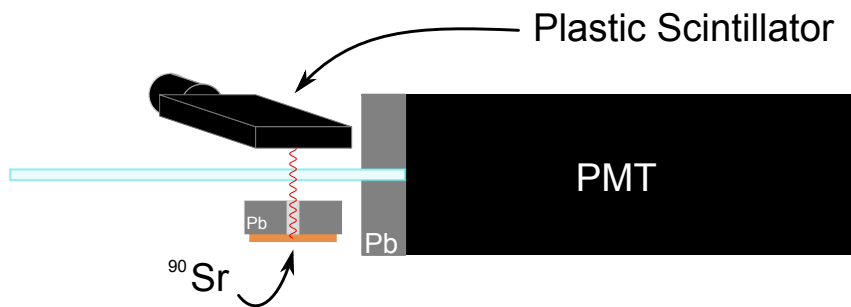


Figure 3.5: Schematic view of the coincidence measurement setup. A fiber is placed onto a PMT through a hole in the lead shielding. A ^{90}Sr β source was placed underneath the fiber and a thin plastic scintillator.

The response was measured for 5730 s followed by a background measurement of 70 400 s for which the fiber was removed. The resulting histograms were scaled to their acquisition time and the background subtracted resulting in the distribution shown in figure 3.6. A signal corresponding to one to two photoelectrons is produced after subtracting the pedestal.

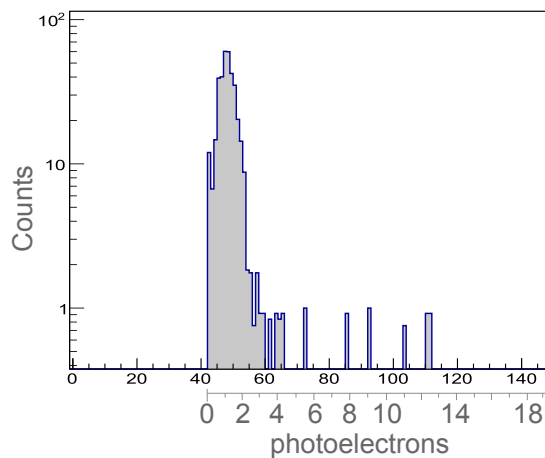


Figure 3.6: Measured photons emitted by a DSB fiber, read out as seen in the schematic 3.5.

3.2.3 Fiber Matrix

In order to measure the response of a higher energy source a measurement with cosmic radiation was set up. Cosmic radiation at sea level consists of secondary particles created to 90 % by primary protons interacting in the atmosphere. They consist in part of π^\pm , p , e^\pm , n but mostly μ^\pm [2, p. 379]. Shielded by the concrete of the building only muons are expected in the lab. These cosmic muons have a mean energy of ≈ 4 GeV with decreasing numbers to below 1 GeV and a steepening falloff in rate as energies approach 100 or even 1000 GeV [2, p. 307].

A 4×5 molybdenum matrix with thin, 5 mm long DSB fibers seen in figure 3.7 was assembled and used to measure responses to cosmic muons. The fibers were wrapped in one to two layers of thin teflon. The module then was connected to two PMTs on each end and read out in coincidence. A schematic of the electronics used for the readout is shown in figure 3.8. It is essentially the same setup as in section 2.2 only for two signals processed in parallel and read out if both PMTs measure a pulse at the same time.

Figure 3.7: An array of 4×5 5 mm long DSB fibers, placed in a molybdenum matrix.

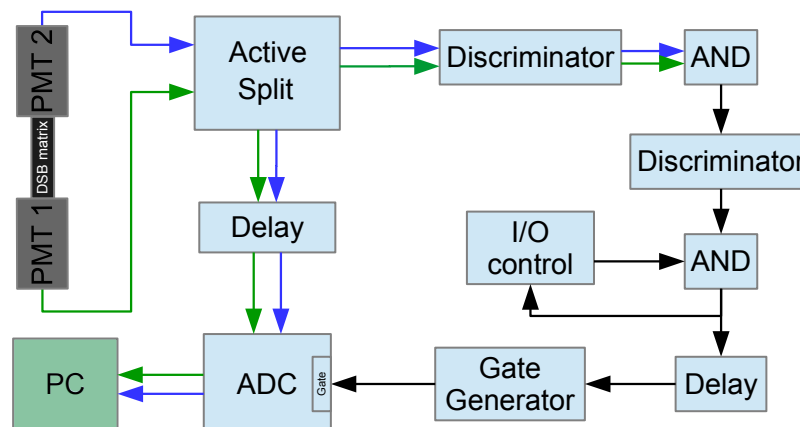


Figure 3.8: Schematic setup of the electronics for a double readout of the DSB fiber matrix.

This setup ran for 1 031 000 s or almost 12 days, collecting data continuously. The obtained signal distributions are shown in figure 3.9. Although still some

random coincidences are observed leading to the low amplitude component, a clear signal corresponding to ≥ 100 photoelectrons can be seen. The upper images show the response of each PMT separately. The 2D distribution of the correlation of the two PMT signals is shown in the image below.

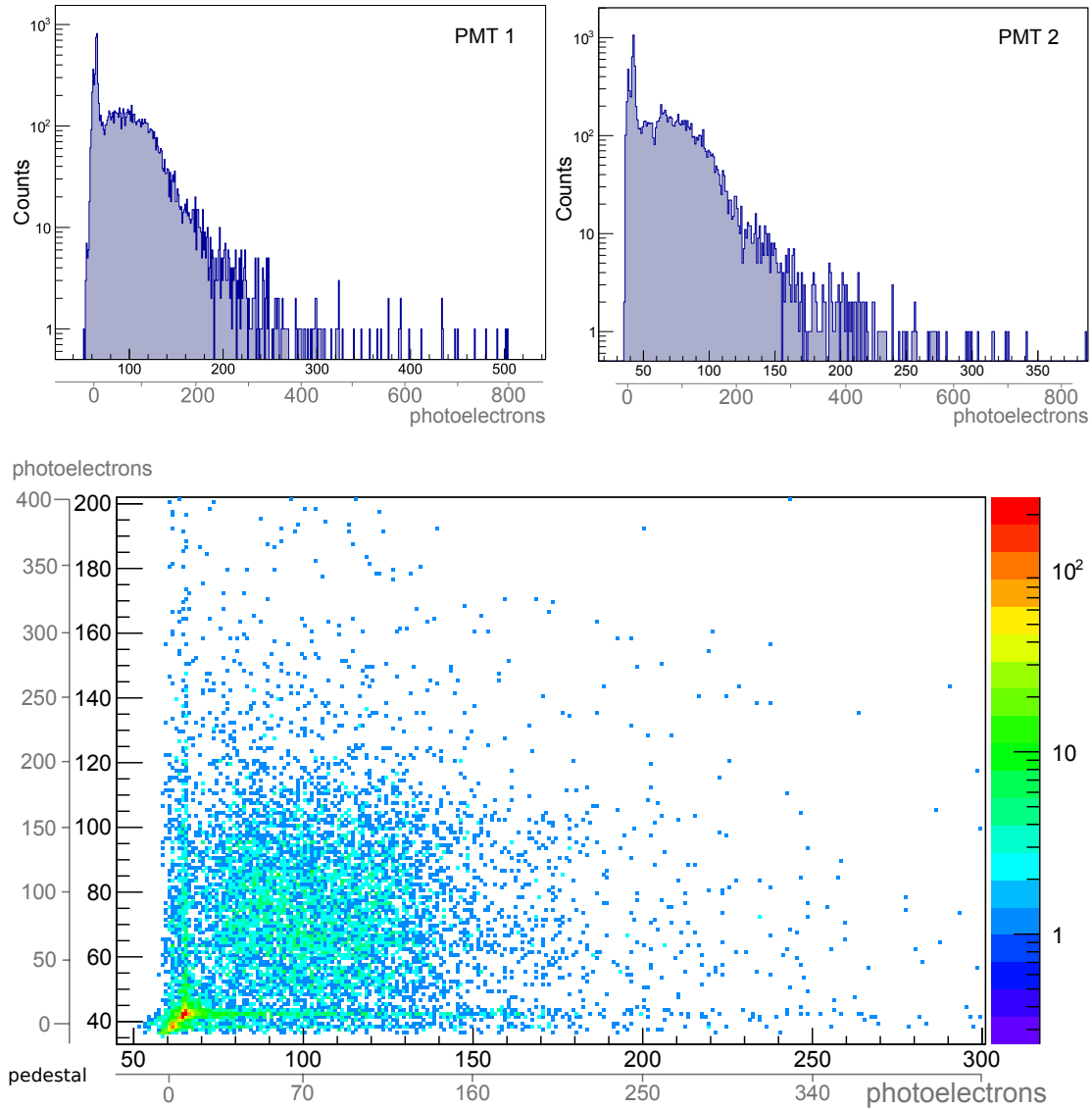


Figure 3.9: Signal distributions of the two PMTs in 3.8 read out in coincidence shown separately and the distribution of the signals measured in one PMTs versus the other.

3.3 DSB Block

A first larger piece of DSB ($23 \times 23 \times 120 \text{ mm}^3$) has been delivered by the INP. This block has a slightly milky appearance since it contains many visible macro defects inside of the material. Light scattered by these defects can be seen in the illuminated block shown in figure 3.10 which diminishes the optical transparency.

3.3.1 Transmission Measurements

Transmission measurements were done for wavelengths from 300 nm to 900 nm in transversal and longitudinal direction as seen in figure 3.11. Along the full length of the block a transparency of only up to about 25 % was measured, depending on the position. The transversal transmission measurements also yielded position dependent values in the range of 60 to 75 %, respectively.

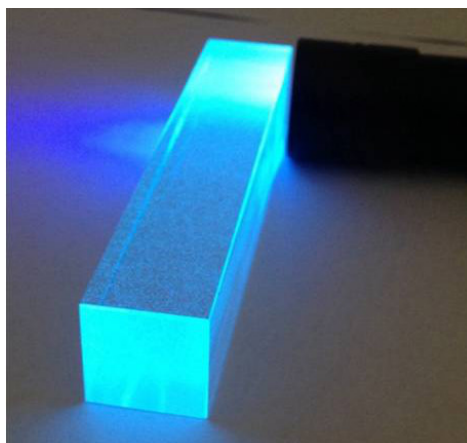


Figure 3.10: $23 \times 23 \times 120 \text{ mm}^3$ block of DSB illuminated to make the defects inside the material visible.

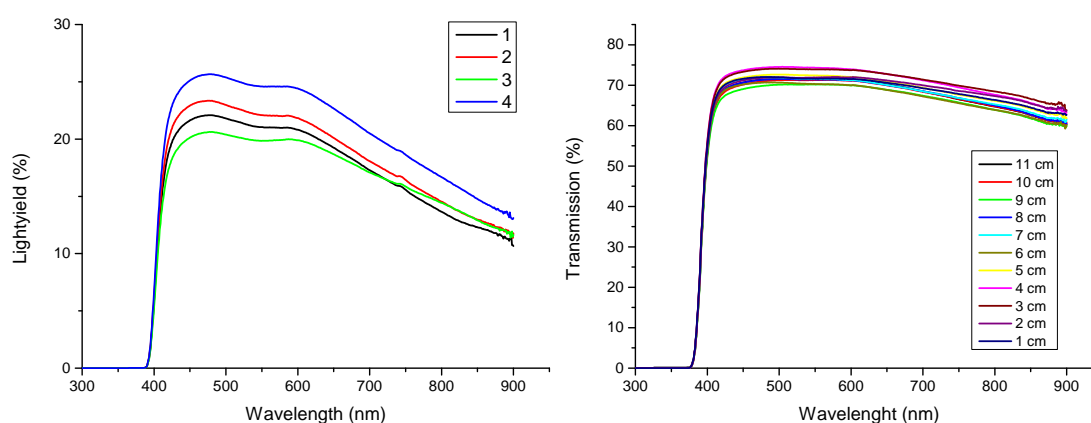


Figure 3.11: Transmission of the DSB block, **left:** measured longitudinally at different positions in the central are of the sample **right:** and laterally at multiple positions.

3.3.2 Light Yield Measurements

In addition to the transmission measurements the light yield of the DSB block was analyzed. The measurement was performed in a temperature controlled chamber to control the temperature from room temperature down to -45°C . The scintillation light was read out by a *Hamamatsu* R2059 PMT with a quantum efficiency of 22.57 % for 330 nm photons and 18.30 % for 370 nm in the region of the emission

wavelengths. This setup, for which the schematic of the electronics behind it is shown in figure 3.12, was used to examine the kinematics of the scintillation process, by varying the integration gate of the signal, and the temperature dependence of the light yield. In order to ensure a proper sampling of the pulse, the gate was set to start 40 ns before the pulse would rise, effectively being set for 140 ns for an integration time of 100 ns.

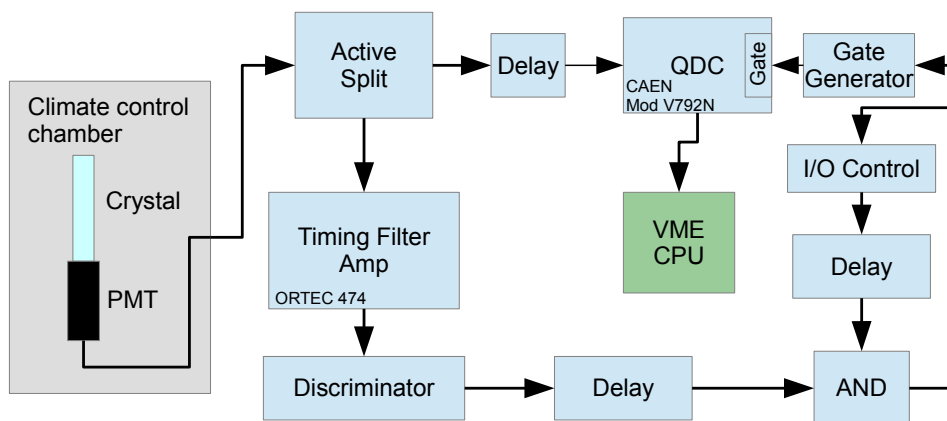


Figure 3.12: Wiring of the readout electronics for the light yield measurements.

As in the measurement setup is similar to the setup shown in section 2.2. The PMT signal was split and one branch is shaped in a timing filter amplifier and digitized. This signal runs by the I/O control blocking data acquisition as long as an event is being processed. The gate generator stretches incoming logic signals to produces a gate of variable length, setting the integration time of the QDC reading out the other branch, the analog PMT signal.

As the light yield is low, using a discriminator only, might lead to a delayed trigger for the data acquisition. Since the data acquisition rate is limited, it is necessary to set the discriminator level high enough to cut out the noise of random PMT signals that would block the acquisition electronics. In order to separate the random noise signals from the longer signal of the scintillation processes the PMT signal has been shaped with an appropriate integration time using a timing filter amplifier.

The sample was exposed to a ^{60}Co source positioned at the top of the block to produce scintillation events. ^{60}Co was chosen as a source since it showed a good separation of the photopeak to the high contribution of the Compton spectrum. As seen in figure 3.13 the resolution is not sufficient to resolve the two emitted γ lines at 1.17 MeV and 1.33 MeV. The signals were digitized by a *charge to digital converter* (QDC). Measurements were performed for different gate lengths at different temperatures. Such a measured photoelectron distribution for different integration times is shown in figure 3.13 for a measurement done at -45°C .

The light yield increases with increasing integration times up to $10\ \mu\text{s}$. A slight temperature dependence of the light yield is observable with an increase of light for higher temperatures. As seen in figure 3.14, the measurement at 18°C shows the highest light yield with a decrease to lower temperatures. Since a cobalt source

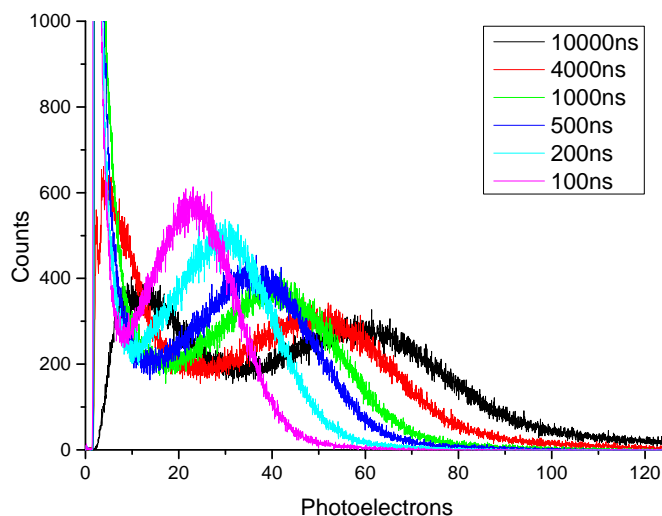


Figure 3.13: Histogram of a 300 second long light yield measurement with different integration times at a temperature of -45°C .

with two emission lines was used all data points were divided by the mean energy of 1.25 MeV to obtain the light yield per MeV.

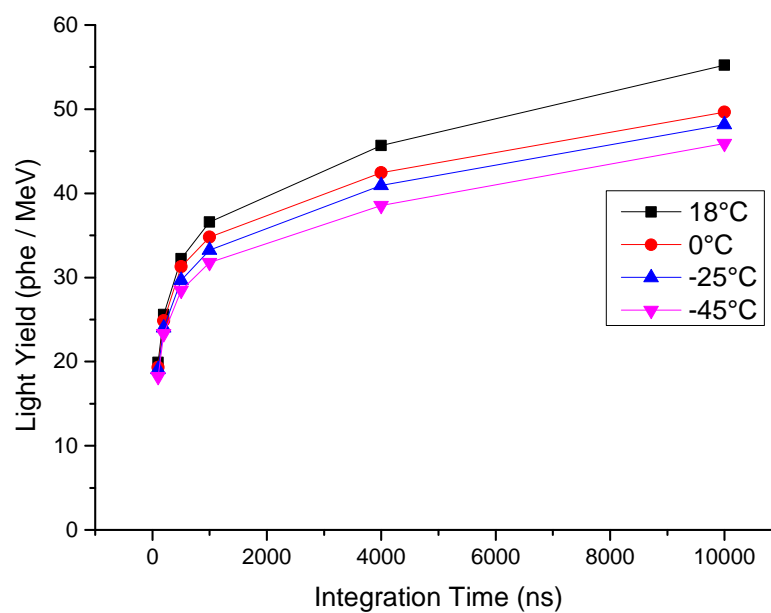


Figure 3.14: Measurements of the integration time dependent light yield at different temperatures for gates between 100 ns and 10 μs .

From this distribution the scintillation decay times (τ_1, τ_2, τ_3) can be determined. Previous measurements sampling the emitted light pulses over 300 ns showed three emission centers with decay times of $\tau_1 = 5.7 \text{ ns}$, $\tau_2 = 30.2 \text{ ns}$, $\tau_3 = 175.5 \text{ ns}$ [28]. So, for this measurement three components were expected, in addition to a long component in the order of μs . For long gate lengths the collected light saturates. With an exponential decrease in light yield over time an inverse exponential growth

of the light yield with $LY(t) = I_\infty - A_0 \cdot e^{-t/\tau}$ is expected. For four emission centers this leads to

$$LY(t) = I_\infty - A_1 \cdot e^{-t/\tau_1} - A_2 \cdot e^{-t/\tau_2} - A_3 \cdot e^{-t/\tau_3} - A_4 \cdot e^{-t/\tau_4}. \quad (3.3.1)$$

The time frame of the measurement done in [28] was only 300 ns, much shorter than the 10 μ s the light was collected for in these measurements. In addition to that, the shortest integration time utilized in these measurements was 100 ns which is considerably longer than the short scintillation decay times. For these reasons it can not be expected to approximate the shortest decay time very accurately. More data points for a better description of the decay time were recorded and are plotted in figure 3.15 with a fit of the equation (3.3.1). The fits produce two different sets of decay times: (25 ± 38) ns, (179 ± 99) ns, (677 ± 580) ns and (6411 ± 1729) ns as well as an offset of $I_\infty = (66.2 \pm 2.1)$ photoelectrons for 18 °C, and (62 ± 37) ns, (242 ± 70) ns, (2101 ± 2256) ns and (17812 ± 86179) ns as well as I_∞ set at a boundary of (70 ± 55) photoelectrons for -25 °C.

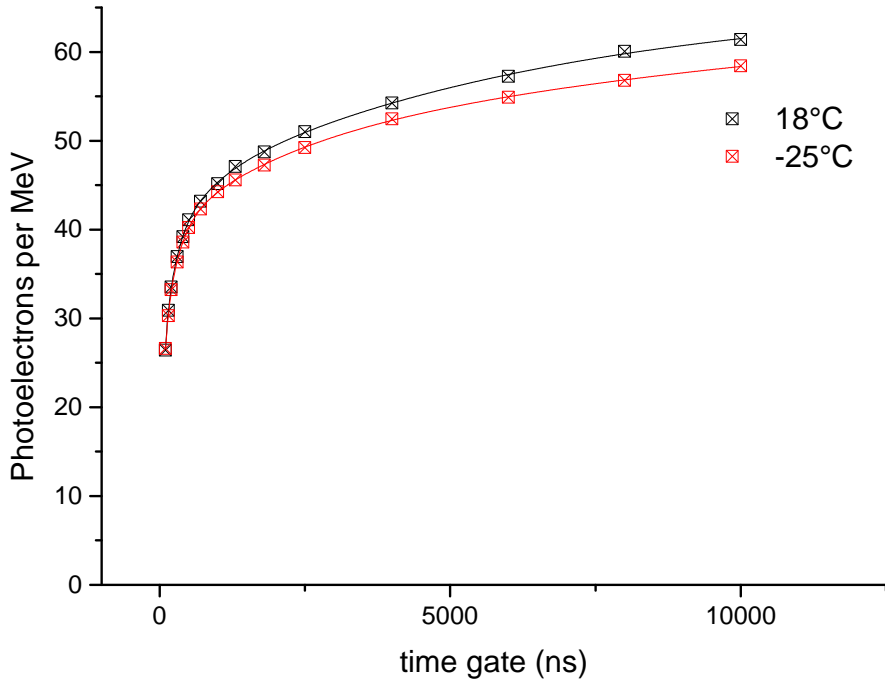


Figure 3.15: Light yield measurements for different integration times with a fit according to (3.3.1).

To describe the temperature dependence of the light yield of DSB, the collected photoelectrons are plotted against the temperature separated by integration lengths. The dependence is seen in figure 3.16. The slopes of the light yield for each integration time, shown in table 3.1, parameterizes the increase in measured photons per K which increases for longer integration times.

Measurements of the position dependent response of the sample were conducted at 18 °C and are shown in figure 3.17. These measurements show a high dependence of the collected light on the position of the source. To estimate this dependence

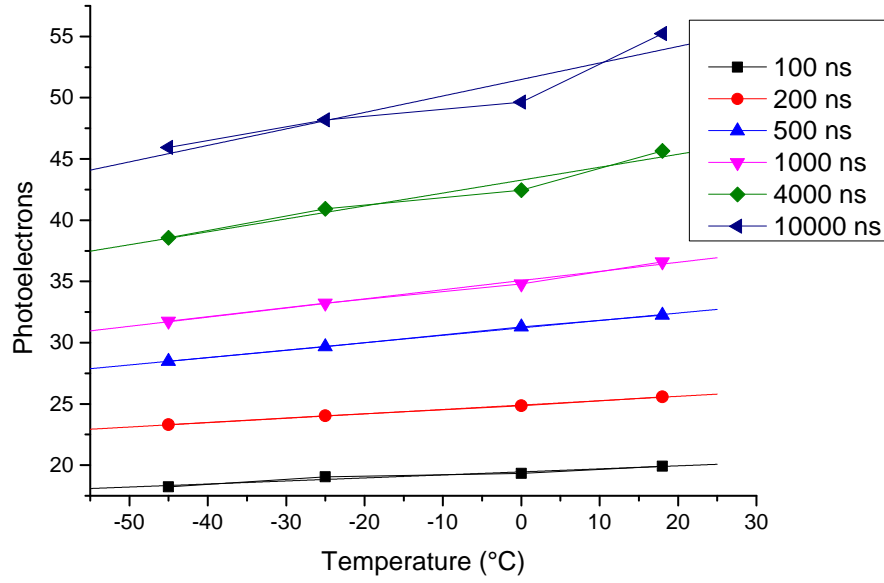


Figure 3.16: Temperature dependence of the light yield for different integration times.

Table 3.1: Temperature dependence of light yield in photoelectrons per 100°C and %per $^\circ\text{C}$.

integration time [ns]	100	200	500	1000	4000	10 000
phe/ 100°C	0.247(41)	3.58(10)	6.10(17)	7.50(47)	10.5(15)	13.5(34)
%per $^\circ\text{C}$	0.13(2)	0.14(2)	0.19(3)	0.21(4)	0.24(4)	0.27(6)

data points were fitted with an exponential curve offset by a constant term.

$$LY(x) = A_0 \cdot e^{-\frac{x}{\Lambda}} + y_0 \quad (3.3.2)$$

The fit produced the following values: $A_0 = (28.66 \pm 0.97)$ photoelectrons, $y_0 = (48.02 \pm 1.42)$ photoelectrons and $\Lambda = (6.69 \pm 0.84)$ cm, which means the light yield is reduced by (13.90 ± 2.18) % per cm up to the offset.

3.3.3 Measurement of the Radiation Damage

To examine the radiation hardness of the material it was subjected to a dose of 100 Gy over one hour, irradiated by a ^{60}Co source. The transmission was subsequently measured again and is depicted in figure 3.18 compared to the transmission at the same position before the radiation. The error of the transmission measurements is below 1 % meaning the observed transmission loss is no statistical fluctuation. In between the irradiation and subsequent transmission measurement done one hour later, the sample was wrapped and placed in a box, minimizing the light exposure of the sample to reduce stimulated recovery of the damages. The measured spectra show some damage as seen in figure 3.18 visualized in the right image by the induced absorption coefficient dk described in (1.5.1).

The high induced absorption coefficient at 300 nm to 400 nm was cut off in the plot since the high value is due to the sharp falloff of the transmission at the

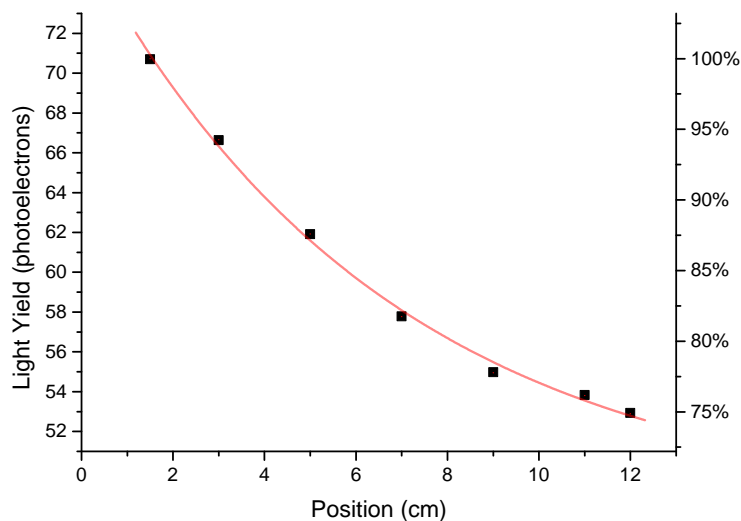


Figure 3.17: Nonuniformity measurement of the DSB block. An exponential decay was fitted to the data points showing a light loss of (13.90 ± 2.18) % per cm.

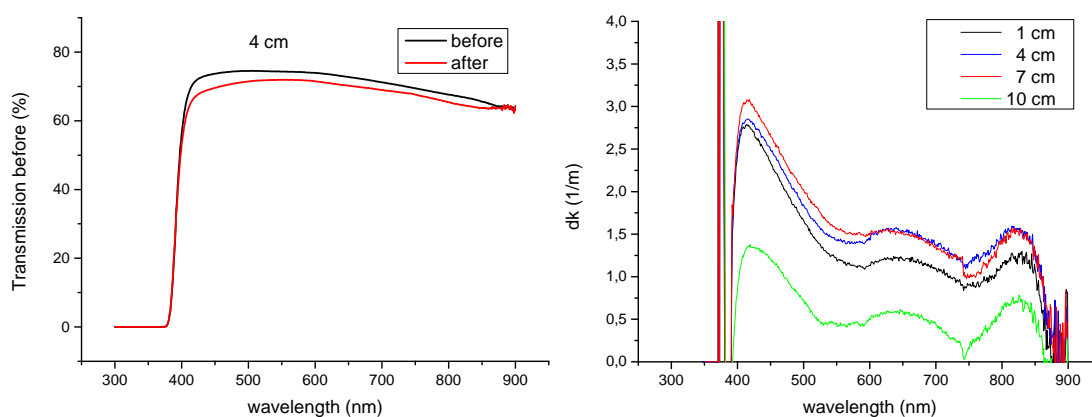


Figure 3.18: left: Comparison of the transversal transmission of the DSB sample at a height of 4 cm before and after irradiation with a dose of 100 Gy of ^{60}Co gammas. **right:** Plot of the induced absorption coefficient at different positions.

absorption edge enhancing the gap at a given wavelength. A minute shift of the absorption edge however is not of significance for the performance of the material. The measured damage shows a position dependence without any sign of regularity along the sample length.

3.4 DSB Block II

To increase the density of the material a $20 \times 20 \times 123 \text{ mm}^3$ DSB sample enriched with gadolinium was produced. The increased density leads to a higher stopping power and consequently a more desirable radiation length and higher γ capture efficiency, improving potential calorimeter performance. The material shows scratches on its surface, macro defects as well as opaque spots inside the otherwise colorless and clear sample. This block is seen in figure 3.19.



Figure 3.19: The block of DSB enriched with gadolinium with opaque, white spots inside.

3.4.1 Transmission Measurements

The transmission was measured longitudinally and transversely. Due to visible imperfections inside the material a longitudinal transmission of $\leq 4\%$ was measured. The transversal transmission strongly depends on the position even varying strongly for orthogonal light paths at the same height when the crystal is rotated by 90° as shown on the right side of figure 3.20.

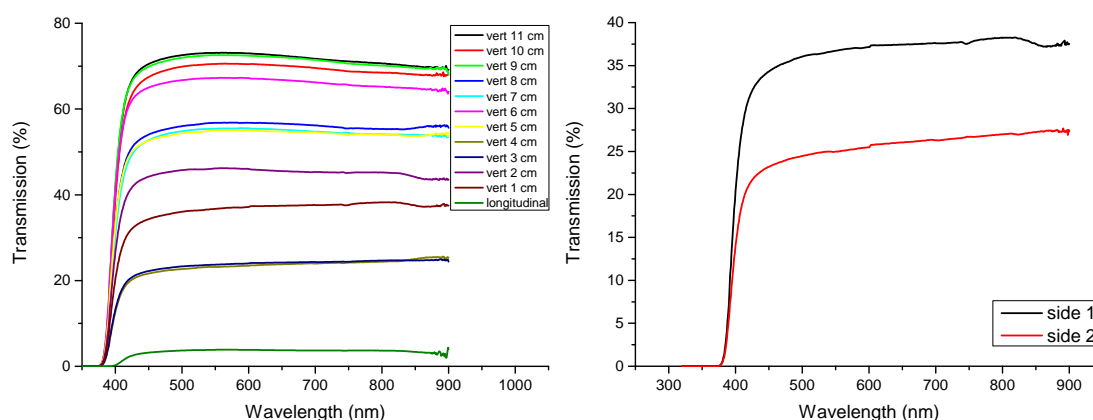


Figure 3.20: Transmission of the the Gd enriched DSB sample, **left:** measured horizontally and vertically at different heights measured from the bottom, along the block and **right:** measurement at a height of 1 cm from two sides turned by 90° .

The variation of the imperfections and defects can be documented by the lateral transmission at 450 nm as a function of position shown in figure 3.21, the development of the transmission along the crystal.

3.4.2 Light Yield Measurements

Comparing the sources ^{60}Co , ^{137}Cs and ^{22}Na in figure 3.22, the well pronounced photopeak corresponding to 511 keV from a ^{22}Na source was used the measurements of the light yield and attenuation of the sample. Light yield measurements were done at -25°C and 18°C for several integration gates between 100 ns and 10 000 ns. The results are shown in figure 3.23. Since the sample shows such a poor transmission two measurements the source was placed 2 cm from the bottom of the block, close to the PMT. The measurement at 18°C was repeated with the source placed on top of the sample despite the limited transparency.

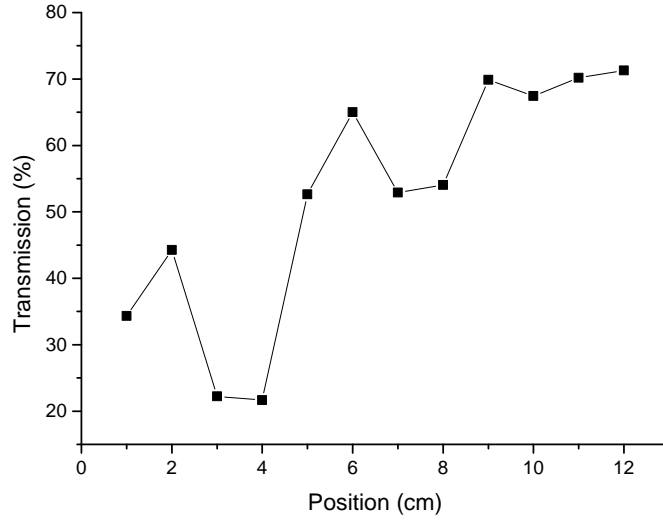


Figure 3.21: Development of the transmission along the Gd enriched DSB sample compared at 450 nm.

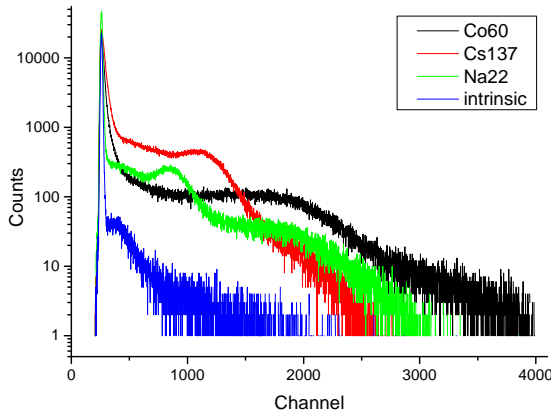


Figure 3.22: Response of the Gd enriched DSB sample for different γ sources with a integration time of 4 μ s.

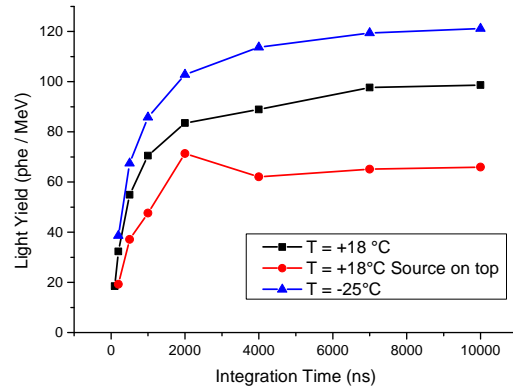


Figure 3.23: Light yield of the Gd enriched DSB sample for different integration times between 100 ns and 10 μ s.

The position dependence of the light yield on the irradiation point in the sample, was measured too and can be seen in figure 3.24. The data points were fitted by an offset exponential function as in equation (3.3.2) with the parameters $A_0 = (23.58 \pm 2.58)$ photoelectrons, $y_0 = (24.52 \pm 3.31)$ photoelectrons and $\Lambda = (10.40 \pm 2.87)$ cm which means a light loss of (9.17 ± 2.92) % per cm.

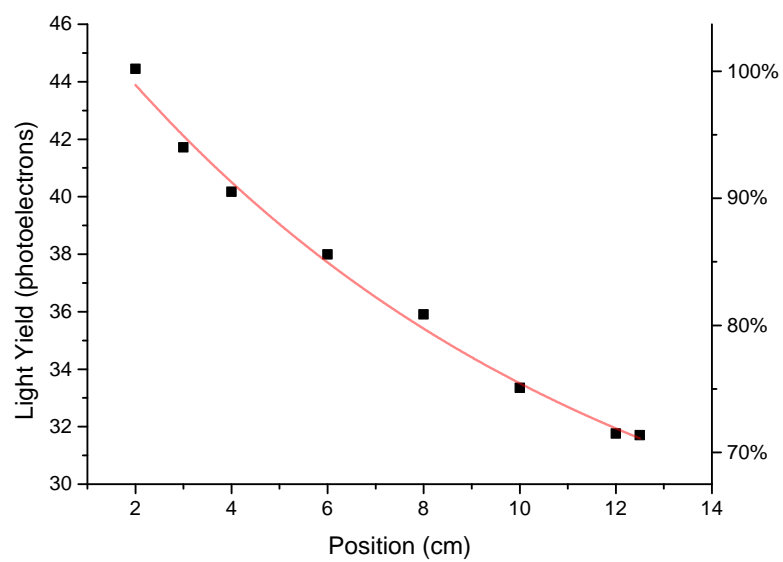


Figure 3.24: *Non-uniformity of the light yield of the Gd enriched DSB sample irradiated along its side.*

Chapter 4

Discussion

4.1 LuAG fibers

4.1.1 Attenuation of irradiated pulled LuAG fibers

Measurements of the irradiated pulled LuAG fibers show little to no damage. This could be due to two factors. First, about 15 months passed between the irradiation in Groningen and the attenuation measurement. This gave them time to recover and potentially repair the damages. This contribution however should be minimal since they were kept cold and in the dark. Secondly the fibers were exposed to a fluence of $7.5 \cdot 10^{12}$ protons/cm². Fibers irradiated with higher fluences, comparable to the expected dose of the detectors at the LHC after the upgrade, of around $6 \cdot 10^{13}$ protons/cm² show more damage as seen in [30]. Nonetheless the LuAG fibers have shown a good radiation hardness for this limited dose.

4.1.2 Attenuation of cut LuAG and YAG fibers

The high light yield measured for the YAG fibers is surprising. A light yield of 35 000 Ph/MeV for YAG and of 25 000 Ph/MeV for LuAG are reported [31]. This means a light yield 1.4 times higher for YAG than for LuAG. The light yield for the fibers however, taking the different quantum efficiency of the MPPCs into account, show a light yield for the YAG fibers 3.5 times higher than for the LuAG fibers.

The cause of this discrepancy could be production irregularities. Furthermore no further information is given, detailing the light yield measurements or their accuracy.

The irregular attenuation behavior of the fibers is most likely due to inhomogeneities of the cerium concentration inside the crystal creating position dependent absorption. Cerium inhomogeneities also lead to inhomogeneous light yields. This effect can easily be seen by looking at observed light yield close to the SiPM where attenuation effects hardly play a role. At this point the light yield of LuAG fiber 2 show a large discrepancy for each side.

The attenuation measurements done for the YAG fibers also suggest that the fiber performance depends on the initial crystal or position in the bulk material from where the fiber is cut. Fiber 38 and 39 show very similar performance whereas fiber number 6 shows a steady exponential attenuation with an attenuation coefficient of $\mu_6 = 0.052 \text{ cm}^{-1}$ much lower than for fiber 38 and 39, $\mu_{38} = 7.3 \cdot 10^{-3} \text{ cm}^{-1}$ and $\mu_{39} = 8.6 \cdot 10^{-3} \text{ cm}^{-1}$.

4.1.3 LuAG fiber calorimeter

The results of the first beam time show a poor performance, both in terms of linearity and resolution. A fitted function with the constant factor $c_1 = 0$, described purely by the statistical term $c_0/\sqrt{E[\text{GeV}]}$ can not be physically accurate but the fit will only assume the factor to be the lowest set bound which makes all parameters unreliable. The linearity issues could be explained by the fact that the employed module has suffered from a large amount of leakage although it was about $28.8 X_0$ long for tungsten but only $7.1 X_0$ of LuAG respectively. The short radiation length of LuAG is significant since a positioning of the module with fibers parallel to the photon beam allows a shower development along these fibers with reduced interaction in the absorber. In addition to the longitudinal loss significant transversal losses can be expected since the beam spot of about 1 cm nearly covers the whole module. This means it is possible for a shower that develops close to the edge to be partially lost since the module has a Molière radius of 1.09 cm, almost as big as the sensitive core of the module itself. These losses increase as the shower grows in size for higher energies causing a relative signal reduction seen in figure 2.16.

At low energies the relevant detector signal overlaps with the background of random signals. This distorts the line shapes leading to a reduced peak position. A parametrization of this background would improve the fit and result in a more accurate resolution determination.

This behavior however is not observed for the calibration measurements of the second beam time which shows a better linearity and considerably better resolution for what in principle should effectively be the same setup.

The shape of the measured energy distribution for the LuAG fiber calorimeter contradicts expectations from homogeneous calorimeters in which a Gauss-like peak with a tail to lower energies is seen. The measured distributions however show a wide peak with a significant tail to higher energies. This tail is most likely caused by the inhomogeneity of the module resulting in events where an incident photon hits a fiber and deposits more energy in the active material.

This is confirmed by simulations for such a fiber calorimeter with the same dimensions done by P. Orsich. Photons hitting the dead material produce a smaller signal than photons that first interact in a fiber directly. Figure 4.1 shows the effect of a widening beam spot on the line shape. At 1 mm radius the beam only hits dead material directly producing a nice and symmetric distribution. With a growing beam spot more photons start hitting fibers directly and the high energy tail grows. This effect is enhanced by the fact that the module has a low sampling fraction of about 8%.

Tilting the module around two axes should reduce the asymmetry of the distribution of the measured energy. This prevents showers from mainly developing along either fibers or absorber material. It increases the effective sampling frequency and decreases the influence of the point of primary interaction. This is also supported by the simulations as seen in the right figure of 4.1 a tilt of 6° is sufficient to receive a more symmetrical response. Tilting the module further to 10° shows no improvement.

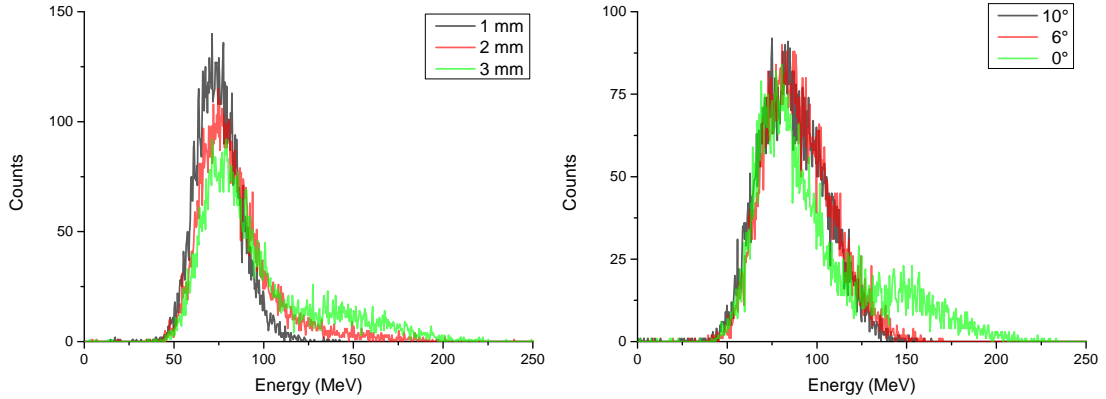


Figure 4.1: Simulations done with a 1 GeV photon beam for a module with 12×12 20 cm long fibers in the same arrangement as the LuAG fiber matrix used at the second beam time. **On the left:** Simulations done for different beam sizes of 1 mm to 3 mm. **On the right:** Simulations for tilting of the fiber module towards the beam of 0° , 6° and 10° [32].

The addition of further modules, all readout simultaneously should reduce the transversal losses due to the increase in size and hence increase the detector response. The measured data however shows 22 % smaller amplitude signals compared to the calibration measurement of module 1, averaged over all tagger energies and an energy dependent reduction for the integral. This effect was most likely due to the thick absorber layers at the boundary between modules. Since four single modules were just bound together the outer absorber layers formed a cross of 2 mm thickness in the center, decreasing the sampled energy.

This effect not only produces a decreased signal but the inhomogeneity causes position-dependent fluctuations of the energy deposition in the active material, the fibers. For these reasons larger modules are required with a reduced thickness of the outer wall to achieve homogeneity.

The lower signal strength directly translates into the resolution, showing a worse resolution for the sum of the signals both for the amplitude and integral methods compared to signals produced in single modules.

The worse resolution observed for feature extraction via integral compared to the feature extraction via amplitude most likely stems from the higher sensitivity of the integral on the pulse shape of the event. Slight variations in the pulse decay or pileup of multiple pulses do not influence the amplitude as much if at all whereas the integral can increase significantly. Especially at low energies where the pulse amplitude is small a lot of noise can be picked up since the ADC base value, the pedestal, is slightly unstable. The impact of an imprecise measured pedestal also has a larger impact on the integral than on the amplitude. When adding multiple modules this noise from non-involved modules can not be cut completely without cutting the actual signal worsening the resolution of the sum even further. In addition to that the energy may spread onto multiple modules lowering the individual responses, amplifying the relative noise contribution since multiple readout channels are added. This effect loses its significance for higher

energies as the pulse amplitude and integral increase, explaining why the amplitude and integral resolution become similar for higher energies.

When rejecting pulse shapes with an integral to amplitude ratio above the cutoff value the drawbacks need to be considered too. Although the energy resolution for the feature extraction for the integral method shows improvements at low energies no significant improvement of the resolution can be seen for feature extraction for the amplitude method. The discarded events only cause a loss of statistics.

The increase of rejected events for low energy channels can be caused by the higher relative contribution of the noise of the electronics deforming the pulses and causing the integral amplitude ratio to exceed the cutoff value.

The resolution the LuAG module shows for photons between roughly 50 MeV to 800 MeV with the given shape of the distribution, poses great difficulties for its application. The histograms for all tagger energies up to the 800 MeV are not only very broad with a relative resolution of more than 30% but all show a spread of events from no measured energy deposition to the double of the peak position. This wide range of measured energies for a single photon energy allows the association of single events with arbitrary high energies.

4.2 DSB

4.2.1 Emission

Two broad emission lines of the scintillation light could be distinguished at around 425 nm and 470 nm. Since they are so close to the absorption edge the transmission differs for the two emission wavelengths. The transmission of the 425 nm component is lower leading to a stronger attenuation along the material and resulting in the observed relative decrease in intensity compared to the 470 nm component seen in figure 3.4.

The different emission spectra of the blue and yellow colored fibers and their color itself can most likely be explained by different transmittance namely a lower transmission for blue light in the yellow fibers. A reduction of blue light which has a wavelength of about 400 to 475 nm makes an object appear yellow. As the emission spectrum also lies in this wavelength region it is also affected by the higher absorption the shorter wavelength component leading to the relative decrease in intensity. If blue light is missing objects appear yellow just as the fibers do.

4.2.2 Fiber Measurements

The low light yield of the first fiber measurements examined in section 3.2.2 is somewhat reasonable. At a light yield of only a few photons it is not possible to measure the attenuation appropriately. The stopping power for the electrons emitted by the strontium source is about $1.47 \text{ MeVcm}^2 / \text{g}$ for a 50/50 compound of BaO_2 and SiO_2 [33], leading to an average energy deposition of about 0.59 MeV mm^{-1} when multiplied by the density of DSB. Considering that an electron would on average traverse 0.785 mm for a 1 mm fiber, about 0.43 MeV would be deposited.

Taking the light yield measurement of the big block of DSB of up to 50 photoelectrons per MeV for a crude estimation, a signal of around 22 photoelectrons should have been seen. This however does not take the different data acquisition methods and geometry into account.

The light yield of the DSB block was measured for a large piece of DSB wrapped in multiple layers of Teflon, reflecting photons back into the sample. Measuring the fibers without any wrapping leads to a large loss of electrons since photons of an angle smaller than the critical angle do not undergo total reflection and are lost in large part. Approximating the refractive index of DSB with $n_{\text{DSB}} \approx 1.55$ the refractive index of quartz leads to a critical angle of about 40° . This leads to a loss of about 72% of photons for an isotropic emission of photons as backwards emitted light is lost too, leaving 6.16 photons that reach the readout. This effects is enhanced by the thin diameter of the fibers forcing scintillation photons to reflect multiple times before reaching the readout at one end. This significant loss of photons for thin fibers with the relatively low light yield and the cracks and macro defects inside the fibers then produce such a small signal.

4.2.3 DSB Matrix

This measurement recorded 11890 events in 1 031 000 s which corresponds to 0.692 events per minute. A flux of one muon per cm^2 and second can be expected for horizontal detectors [2]. This means 5 muons should have hit the 5 cm^2 module every minute which is significantly smaller but about the same order of magnitude of the expected value.

The much larger light yield of the DSB fiber matrix compared to single fibers was to be expected for multiple reasons. To estimate the stopping power of a muon in DSB the stopping power in the chemically similar BaSO_4 with a comparable density of 4.5 g/cm^3 is used. A 4 GeV muon in BaSO_4 has a stopping power of $1.77 \text{ MeVcm}^2 / \text{g}$ [24]. Muons in this energy region are slightly above minimum ionizing which means they show only very little energy dependence. Such a stopping power would deposit 0.53 MeV in 0.79 mm of DSB. This is only about 1.2 times more energy than for the strontium electrons.

The setup used however does not only read out one fiber but 20 at the same time of which multiple can be struck by a single muon. In addition to that the high energies of the cosmic muons do not quite lead to a shower production but to the emission of secondary particles inside the absorber material surrounding the fibers. These particles, mostly electrons, deposit energy inside the fibers. In addition the fibers were wrapped reducing the photon loss drastically, creating this larger signal.

Since the exact energy of each incident muon is unknown the energy response could not be studied. This measurement however shows that, for fibers of better quality, a proper study of the calorimeter capability is feasible.

4.2.4 DSB Block Transmission Measurement

The measured transmission along the sample of only up to 25 % are not sufficient for a proper application of DSB in calorimeters and has to be improved. The measurements also showed a slight position dependence of the transmission, calling for an improvement of the material homogeneity. The imperfections in the sample loaded with gadolinium prevent an adequate transmission measurement for the whole crystal. The high position dependence of these measurements, caused by the opaque spots, also makes future studies e.g. of the radiation hardness difficult.

4.2.5 Light Yield Measurements

The decay times of (25 ± 38) and (178 ± 99) produced by the light yield fit at 18 °C match nicely to the values measured by [28] although no shorter decay time was approximated. All fitted parameters show very large errors. This is most likely due to attempting to fit nine parameters with 15 data points. The fit of the -25 °C data shows a decay time in the order of 18 μ s and the offset had to be given an upper bound. As this fit does not converge at reasonable values more data points are necessary to approximate the decay times.

These different decay times produce the integration time dependent temperature dependency. Slower components of the decay seem to show a higher temperature dependency. If the integration time is too short this light does not contribute to the signal in a significant way. The longer the integration time the larger the contribution of the dependent decay times. Since the temperature dependence is so small it can not be distinguished between a linear and exponential dependence, as an exponential function can be approximated by a linear function in the first order Taylor expansion. For this reason the measured temperature dependence is given in photoelectrons per °C and percent per °C.

The position dependent light yield in the DSB block is rather high, with a loss of 25.1 % over the length of the sample of the sample or (13.9 ± 2.2) % per cm. This is due to reflections on structural macro defects that increase the path the light has to travel to reach the PMT. The choice of a fit with an offset was made since focusing effects respectively geometry dependent internal reflections influence the light yield as light emitted away from the PMT can be scattered back to the front of the crystal due to the the wrapping and its rough surface. This causes a behavior that can not be described by a simple exponential decay.

The light loss of the sample loaded with gadolinium of (9.17 ± 2.92) % per cm appears lower than for the first DSB sample although the transmission is worse. But if the lower offset is taken into account a greater absolute loss of 28.7 % is observed. This light loss however is not as high as one might expect from the longitudinal transmission measurements where the first DSB block showed a transmission of up to 25 % the Gd loaded sample however only about 4 % which in comparison is only 16 % of the first sample. This stems from the distribution of the blemishes inside the second DSB block. A linear measurement from front to back of the sample is interrupted by the opaque spots. Scintillation light however is reflected multiple times and travels all throughout the block passing the spots more often than being

absorbed.

When irradiated from the same position the two DSB samples show about the same light yield. A difference of the temperature dependence can however be observed. While the first DSB sample only doped with cerium shows a decrease of light for falling temperatures the opposite is observed for the Gd loaded sample with a mean increase of $(22.9 \pm 2.5) \%$.

Compared to other inorganic scintillators the DSB samples show a very low light yield similar to PbWO_4 . This low light yield combined with the unrefined production of the material makes the use as fibers not feasible in this state and needs further development to be of interest for scintillation applications.

4.2.6 Radiation Damage

The radiation damage induced by 100 Gy of ^{60}Co radiation is up to three times higher than for PbWO_4 crystals developed for the $\bar{\text{P}}\text{ANDA}$ experiment as seen in figure 4.2, a comparison of the measured damage to the DSB sample and a PbWO_4 crystal exposed to 90 Gy [34]. Especially high transmission losses can be seen for the region of the emission wavelengths from about 400 nm to 500 nm.

Although DSB was developed in hopes of producing an especially radiation hard scintillator material, such a relatively high induced absorption coefficient is no surprise. Glasses tend to be very susceptible to color center formation, as, due to their amorphous structure, they are prone to defects that can be populated by electrons or holes. Seeing as DSB is still in development with visible macro defects in the samples, a more homogeneous crystalline structure should be achievable and improvements in the production should lead to a better radiation hardness.

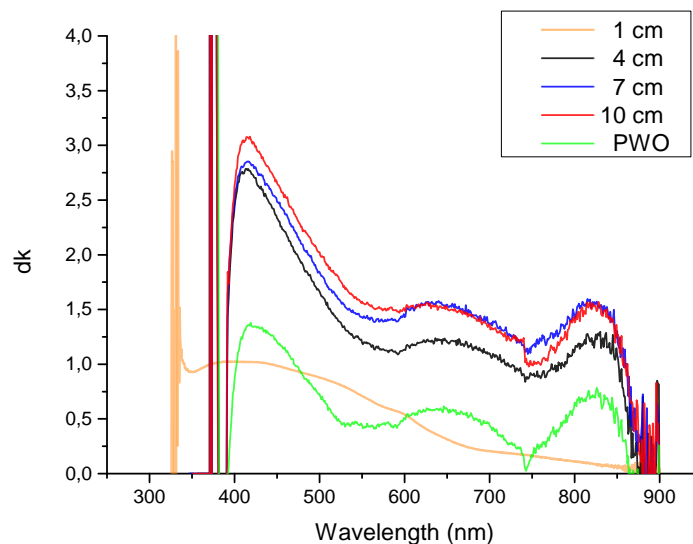


Figure 4.2: Comparison of radiation damage to a $\bar{\text{P}}\text{ANDA}$ PbWO_4 crystal exposed to 90 Gy of ^{60}Co radiation [34] and the DSB sample exposed to 100 Gy.

List of Figures

1.1	Stopping power ($-\frac{dE}{dx}$) of positive muons in copper.	7
1.2	Energy loss per radiation length X_0 for electrons or positrons in lead vs energy.	8
1.3	The mass attenuation of photons in lead.	12
1.4	A comprehensive visualization of which effects dominate at a certain energy and atomic number.	12
1.5	A nuclear reaction between an atomic nucleus and a proton of 30 GeV/c.	13
1.6	Shower development of an incoming photon.	14
1.7	Monte Carlo simulation of the longitudinal shower development of a cascade induced by a 30 GeV electron.	16
1.8	Monte Carlo simulation for the development of the energy loss of electromagnetic showers in different absorber materials.	16
1.9	Simulation of energy deposition by particles of different energies.	17
1.10	Different longitudinal shower developments for 4 different events of incident 270 GeV pions in a lead-iron-plastic sampling calorimeter.	19
1.11	Sampling calorimeter designs.	21
1.12	Schematic setup of a photo-multiplier tube coupled to a scintillator.	27
1.13	Schematic of an avalanche photodiode.	28
1.14	Exemplary radiation induced transmission losses due to γ and proton (150 MeV) irradiation of PbWO_4	30
1.15	Double logarithmic relation between exposed proton fluence and the induced absorption coefficient.	31
1.16	Isotopes and their activity inside the irradiated crystal measured 4 months after exposure to 24 GeV protons.	32
2.1	Sampling calorimeter module with CeF_3 as active material and tungsten as absorber.	34
2.2	Transmission spectra for LuAG with different dopants.	35
2.3	The micro pulling down method to grow thin crystal fibers.	36
2.4	A set of $1 \times 1 \times 10 \text{ mm}^3$ LuAG fibers produced by Crytur.	36
2.5	Measurement setup for LuAG and YAG fibers read out by an SiPM.	37
2.6	Schematic of the readout electronics for the attenuation measurements of single fibers.	38
2.7	Attenuation measurements of the LuAG fibers described in table 2.1 before and after irradiation at KVI with 180 MeV protons. The light yield is given in arbitrary units normalized to the first measurement.	39
2.8	Attenuation measurements of LuAG and YAG fibers.	40

2.9	A single fiber module with LuAG fibers in a tungsten matrix with a wall thickness of 1 mm	40
2.10	The floor plan of the MAMI facility.	41
2.11	Schematic of the Glasgow Tagged Photon Spectrometer.	42
2.12	A spectrum of the recorded tagger times for all events of tagger channel 0 during the calibration run for module 4.	43
2.13	Visualization of the feature extraction through amplitude and integral calculation for a single pulse shape.	44
2.14	Exemplary Novosibirsk fit of a histogram for 377 MeV photons.	45
2.15	Response of the detector for the LuAG and YAG fiber module for amplitude feature extraction.	45
2.16	Linearity of the module for feature extraction via the amplitude and the integral.	46
2.17	Resolution of the LuAG module for amplitude and integral feature extraction.	47
2.18	Four 6×6 LuAG fiber modules combined. Data was taken with the beam aimed at the five marked positions.	47
2.19	Comparison of the resolution for a longer and shorter window of integration (200-1200, 450-900 time bins) in module 3.	48
2.20	Calibrated responses of single modules for the calibration measurements 1 to 4.	48
2.21	Detector responses of each module normalized to module 1.	49
2.22	Noise distributions for a tagger time window outside of the signal window for the feature extraction via the amplitude and via integral.	49
2.23	Multiplicity of modules with a signal above the amplitude threshold for three selected energies (56 MeV, 377 MeV, 767 MeV).	49
2.24	Pulse shapes of two irregular events with a tagger multiplicity of 1.	50
2.25	The relation of pulse integral to amplitude vs the amplitude for all recorded events.	50
2.26	Amplitude distributions of single modules for irradiation at position 5.	51
2.27	Signal distribution after summation of the amplitudes of all four calibrated modules for three selected energies.	51
2.28	Peak position of the sum relative to the calibration measurement of module 1.	52
2.29	Comparison of the resolution for all four calibration measurements and the sum of the four modules at beam position 5 for feature extraction via the amplitude, and the linearity of the sum.	52
2.30	Comparison of the resolution for all four calibration measurements and the sum of the four modules at beam position 5 for feature extraction via the integral, and the linearity of the sum.	53
2.31	A comparison of the obtained resolution for feature extraction via amplitude and integral for a single module and the sum of four modules.	53
2.32	Comparison of the pileup corrected and uncorrected relative resolutions for feature extraction via the amplitude.	54

2.33	Comparison of the pileup corrected and uncorrected relative resolutions for feature extraction via the integral.	54
3.1	A bundle of DSB:Ce fibers from the INP in Belarus.	56
3.2	Transmission of a $13 \times 15 \times 5 \text{ mm}^3$ piece of DSB, with the wavelengths of the emission peaks marked at 425 nm and 470 nm.	57
3.3	Schematic setup of the spectrum measurements of the DSB fibers.	57
3.4	A set of different luminescence spectra, irradiated at different position along a fiber, the irradiation of differently colored fibers as well as a small sample.	57
3.5	Schematic view of the coincidence measurement setup.	58
3.6	Measured photons emitted by a DSB fiber, read out as seen in the schematic 3.5.	58
3.7	An array of 4×5 5 mm long DSB fibers, placed in a molybdenum matrix.	59
3.8	Schematic setup of the electronics for a double readout of the DSB fiber matrix.	59
3.9	Signal distributions of the two PMTs in 3.8 read out in coincidence shown separately and the distribution of the signals measured in one PMTs versus the other.	60
3.10	$23 \times 23 \times 120 \text{ mm}^3$ block of DSB illuminated to make the defects inside the material visible.	61
3.11	Transmission of the DSB block measured longitudinally as well as laterally.	61
3.12	Wiring of the readout electronics for the light yield measurements.	62
3.13	Histogram of a 300 second long light yield measurement with different integration times at a temperature of -45°C	63
3.14	Measurements of the integration time dependent light yield at different temperatures for gates between 100 ns and 10 μs	63
3.15	Light yield measurements for different integration times with a fit according to (3.3.1).	64
3.16	Temperature dependence of the light yield for different integration times.	65
3.17	Nonuniformity measurement of the DSB block. An exponential decay was fitted to the data points showing a light loss of $(13.90 \pm 2.18)\%$ per cm.	66
3.18	Radiation damage as transmission losses.	66
3.19	The block of DSB enriched with gadolinium with opaque, white spots inside.	67
3.20	Transmission of the the Gd enriched DSB sample.	67
3.21	Development of the transmission along the Gd enriched DSB sample compared at 450 nm.	68
3.22	Response of the Gd enriched DSB sample for different γ sources with a integration time of 4 μs	68
3.23	Light yield of the Gd enriched DSB sample for different integration times between 100 ns and 10 μs	68

3.24	Non-uniformity of the light yield of the Gd enriched DSB sample irradiated along its side.	69
4.1	Simulations for a module with 12×12 20 cm long LuAG fibers for different beam widths and angles.	73
4.2	Comparison of radiation damage to a PANDA PbWO ₄ crystal exposed to 90 Gy of ⁶⁰ Co radiation [34] and the DSB sample exposed to 100 Gy.	77

List of Tables

1.1	Short list of radiation lengths and critical energies of some absorber materials.	14
1.2	List of inorganic scintillating material interesting for high energy physics applications.	27
2.1	Irradiated LuAG fibers and their dopant concentration, length and diameter.	38
2.2	Energies corresponding to the active tagger channels given in MeV.	42
3.1	Temperature dependence of light yield in photoelectrons per 100 °C and %per °C.	65

Bibliography

- [1] C. Grupen and B. Shwartz, “Interactions of particles and radiation with matter,” in *Particle Detectors*, pp. 1–55, Cambridge University Press, second ed., 2008. Cambridge Books Online.
- [2] J. Beringer, J. Arguin, R. Barnett, K. Copic, O. Dahl, D. Groom, C. Lin, J. Lys, H. Murayama, C. Wohl, *et al.*, “Review of particle physics,” *Physical Review D*, vol. 86, no. 1, 2012.
- [3] W. Leo, *Techniques for Nuclear and Particle Physics Experiments: A How-To Approach*. Springer, 1994.
- [4] R. Wigmans, *Calorimetry: Energy measurement in particle physics*, vol. 107. Oxford University Press, 2000.
- [5] C. Grupen and B. Shwartz, “Calorimetry,” in *Particle Detectors*, pp. 230–272, Cambridge University Press, second ed., 2008. Cambridge Books Online.
- [6] C. Grupen and I. Buvat, *Handbook of particle detection and imaging*. Springer Science & Business Media, 2011.
- [7] C. Fabjan, W. Struczinski, W. Willis, C. Kourkoumelis, A. Lankford, and P. Rehak, “Iron liquid-argon and uranium liquid-argon calorimeters for hadron energy measurement,” *Nuclear Instruments and Methods*, vol. 141, no. 1, pp. 61 – 80, 1977.
- [8] Crystal Clear Collaboration, “Scintillators for high-energy physics.” <http://crystalclear.web.cern.ch/crystalclear/scintforhep.html>, 2016.
- [9] Wikipedia, “Photomultiplier — Wikipedia, The Free Encyclopedia,” 2016. [Online; accessed 12-April-2016].
- [10] Wikipedia, “Avalanche-photodiode — Wikipedia, Die freie Enzyklopädie,” 2015. [Online; Stand 12. April 2016].
- [11] R.-y. Zhu, “Radiation damage in scintillating crystals,” *Nuclear Instruments and Methods in Physics Research Section A: Accelerators, Spectrometers, Detectors and Associated Equipment*, vol. 413, no. 2, pp. 297–311, 1998.
- [12] G. Dissertori, D. Luckey, F. Nessi-Tedaldi, F. Pauss, M. Quittnat, R. Wallny, and M. Glaser, “Results on damage induced by high-energy protons in LYSO calorimeter crystals,” *Nuclear Instruments and Methods in Physics Research Section A: Accelerators, Spectrometers, Detectors and Associated Equipment*, vol. 745, pp. 1–6, 2014.

- [13] A. E. Borisevitch, V. I. Dormenev, A. A. Fedorov, M. V. Korjik, T. Kuske, V. Mechinsky, O. V. Missevitch, R. W. Novotny, R. Rusack, and A. V. Singovski, "Stimulation of radiation damage recovery of lead tungstate scintillation crystals operating in a high dose-rate radiation environment," *Nuclear Science, IEEE Transactions on*, vol. 60, no. 2, pp. 1368–1372, 2013.
- [14] V. Dormenev, M. Korjik, T. Kuske, V. Mechinski, and R. W. Novotny, "Comparison of radiation damage effects in PWO crystals under 150 MeV and 24 GeV high fluence proton irradiation," *Nuclear Science, IEEE Transactions on*, vol. 61, no. 1, pp. 501–506, 2014.
- [15] V. Dormenev, T. Kuske, R. Novotny, A. Borisevich, A. Fedorov, M. Korjik, V. Mechinski, O. Missevitch, and S. Lugert, "Stimulated recovery of the optical transmission of PbWO_4 scintillation crystals for electromagnetic calorimeters after radiation damage," *Nuclear Instruments and Methods in Physics Research Section A: Accelerators, Spectrometers, Detectors and Associated Equipment*, vol. 623, no. 3, pp. 1082–1085, 2010.
- [16] F. Nessi-Tedaldi, G. Dissertori, Q. Huang, W. Lusterhmann, D. Luckey, S. Luterer, F. Pandolfi, F. Pauss, M. Peruzzi, M. Quittnat, and R. Wallny, "Proof-of-principle of a new geometry for sampling calorimetry using inorganic scintillator plates," *IEEE NSS*, 2014. paper N24-32.
- [17] R.-Y. Zhu, "The next generation of crystal detectors," *Journal of Physics: Conference Series*, vol. 587, no. 1, p. 012055, 2015.
- [18] H. Ogino, A. Yoshikawa, M. Nikl, J. A. Mares, J. ichi Shimoyama, and K. Kishio, "Growth and optical properties of $\text{Lu}_3(\text{Ga,Al})_5\text{O}_{12}$ single crystals for scintillator application," *Journal of Crystal Growth*, vol. 311, no. 3, pp. 908 – 911, 2009. The Proceedings of the 4th International Asian Conference on Crystal Growth and Crystal Technology.
- [19] E. Auffray, D. Ablter, S. Brunner, B. Frisch, A. Knapitsch, P. Lecoq, G. Mavromanolakis, O. Poppe, and A. Petrosyan, "LuAG material for dual readout calorimetry at future high energy physics accelerators," in *Nuclear Science Symposium Conference Record (NSS/MIC), 2009 IEEE*, pp. 2245–2249, Oct 2009.
- [20] P. Lecoq, "New crystal technologies for novel calorimeter concepts," *Journal of Physics: Conference Series*, vol. 160, no. 1, p. 012016, 2009.
- [21] C. Dujardin, C. Mancini, D. Amans, G. Ledoux, D. Ablter, E. Auffray, P. Lecoq, D. Perrodin, A. Petrosyan, and K. Ovanesyan, "LuAG: Ce fibers for high energy calorimetry," *Journal of Applied Physics*, vol. 108, no. 1, p. 013510, 2010.
- [22] S. Diehl, R. W. Novotny, N. Aubry, S. Faraj, and G. Ferro, "Development and characterization of inorganic scintillating fibers made of LuAG:Ce and

- LYSO:Ce,” *Nuclear Science, IEEE Transactions on*, vol. 61, no. 1, pp. 353–361, 2014.
- [23] H. P. K.K., “Physics and operation of an MPPC.” http://www.hamamatsu.com/us/en/community/optical_sensors/tutorials/physics_of_mppc/index.html, 2016.
- [24] Particle Data Group, “Atomic and nuclear properties of materials,” 2016. [Online; Stand 14. April 2016].
- [25] I. für Kernphysik Johannes Gutenberg Universität Mainz. <http://www.kph.uni-mainz.de/mami.php>, 2016.
- [26] S. Diehl, *Optimization of the influence of longitudinal and lateral non-uniformity on the performance of an electromagnetic calorimeter*. PhD thesis, Justus-Liebig-Universität, Otto-Behaghel-Str. 8, 35394 Gießen, 2015.
- [27] G. J. Tambave, *Electromagnetic calorimeter studies for charmonium physics*. PhD thesis, University of Groningen, 2013.
- [28] E. Auffray, N. Akchurin, A. Benaglia, A. Borisevich, C. Cowden, J. Damgov, V. Dormenev, C. Dragoiu, P. Duerdo, M. Korjik, D. Kozlov, S. Kunori, P. Lecoq, S. W. Lee, M. Lucchini, V. Mechinsky, and K. Pauwels, “DSB:Ce³⁺ scintillation glass for future,” *Journal of Physics: Conference Series*, vol. 587, no. 1, p. 012062, 2015.
- [29] R. B. Firestone, L. Ekström, and S. Y. F. Chu, “Table of radioactive isotopes,” 2016. [Online; Stand 14. April 2016].
- [30] S. Diehl, R. W. Novotny, N. Aubry, S. Faraj, G. Ferro, and M. Kavatsyuk, “Characterization and optimization of new high-quality inorganic fibers made of luag:ce and lyso:ce,” in *2014 IEEE Nuclear Science Symposium and Medical Imaging Conference (NSS/MIC)*, pp. 1–6, Nov 2014.
- [31] Crytur, “Scintillation materials data,” 2016. [Online; Stand 14. April 2016].
- [32] P. Orsich. personal communication.
- [33] N. I. for Standards and Technology. <http://www.nist.gov/pml/data/star/index.cfm>, 2016.
- [34] V. Dormenev. personal communication.

Acknowledgments

I am grateful that this thesis has come to a conclusion. I want to thank Dr. Rainer Novotny for his patience and feedback, pushing my work to a higher standard, as well as my professor Dr. Kai Brinkmann for his support. I also want to express my gratitude towards Stefan Diehl who I have interrupted multiple times a day to ask questions and who always has taken his time to explain the issue thoroughly to me. I want to thank Stefan Friedrich and Valera Dormenev who have given me valuable feedback along the way. A big thank you also belongs to my family who have been very patient with my absence for most of my days for the last four months, especially my little sister Amy. Last of all I would like to thank my girl friend Ida for being so patient about when I would finally be able to move to Vienna and supporting me every step of the way as well as keeping me company during late hour working sessions at the university. Without the contribution of all of you and my other colleagues that I have not mentioned, this work and the time in the group would not have been the same.